Planar Shockwave Collisions in AdS/CFT and Rényi Entanglement Entropy in Yang-Mills Theories

Dissertation

zur Erlangung des Doktorgrades
der Naturwissenschaften (Dr. rer. nat.)
der Fakultät für Physik
der Universität Regensburg

vorgelegt von

Andreas Rabenstein

aus Bad Windsheim

im Jahr 2019

Promotionsgesuch eingereicht am: 9. Juli 2019
Die Arbeit wurde angeleitet von: Dr. Andreas Schäfer

Planar Shockwave Collisions in AdS/CFT and Rényi Entanglement Entropy in Yang-Mills Theories

Abstract

In this thesis, we first give an introduction to the holographic principle by reviewing the basics of bosonic and supersymmetric string theory. Afterwards, we will motivate the holographic principle and give more details about its specific realization in the context of AdS_5/CFT_4. The discussion of the physical relevance of this thesis is then divided into two parts.

In the first part which is based on [1], we will make use of the holographic principle to model Heavy Ion Collisions (HICs) by two colliding lumps of energy in a Conformal Field Theory (CFT). Through the holographic principle, this is mapped to the collision of gravitational shockwaves in an asymptotically Anti-de-Sitter (AdS) spacetime. To reduce complexity we will consider shocks which are infinitely extended in the transverse direction. We will motivate that this can be seen as the first order in a gradient expansion of an off-center collision with finite transverse extent. We find that the post-collision hydrodynamic flow is very well described by appropriate averages of the symmetric collision. Chesler, Kilbertus and van der Schee give an analytic expression for the proper energy density in [2]. In a similar manner, we found an approximation which models initial data for hydrodynamic simulations without the need for cumbersome holographic calculations.

In the second part which is based on [3], we study entanglement entropy in $SU(N_c)$ Yang-Mills (YM) theory. One of the motivations for this was to test how fast the $N_c \to \infty$ limit is reached. Entanglement entropy, or to be more precise the entropic C-function, can be calculated both in holography (for $N_c \to \infty$) and in lattice gauge theory (for finite N_c) which then allows a comparison for these theories. Holography predicts a sharp jump for the entropic C-function in a slap shaped geometry at some finite slap length l_c. In lattice simulations we find a

smooth transition from $\mathcal{O}(N_c^2 - 1)$ down to a value compatible with zero for this observable. Within the statistics achieved in this work, the slope for $SU(4)$ is larger than for $SU(3)$ supporting the holographic scenario.

Planar Shockwave Collisions in AdS/CFT and Rényi Entanglement Entropy in Yang-Mills Theories

Zusammenfassung

In dieser Dissertation geben wir zunächst eine Einführung in die bosonische und supersymmetrische String Theorie mit Hinblick auf die Erklärung des holographischen Prinzipes. Anschließend werden wir uns genauer mit der Realisierung der AdS_5/CFT_4 Dualität beschäftigen. Die physikalische Bedeutung der Arbeit ist dann auf zwei Gebiete aufgeteilt.

Im ersten Teil, der auf [1] basiert, werden wir das holographische Prinzip auf die Modellierung von Schwerionenstößen durch die Kollision von zwei Energieverteilungen in einer konformen Feldtheorie anwenden. Mithilfe des holographischen Prinzipes kann diese Problemstellung in die Kollision von Schockwellen in einer asymptotischen Anti-de-Sitter (AdS) Raumzeit umgewandelt werden. Um die Komplexität des Problems zu reduzieren, verwenden wir asymmetrische Schockwellen mit verschiedenen longitudinalen Dicken, die eine unendliche transversale Ausdehnung besitzen. Wir werden zeigen, dass dies als erster Term einer Näherung in Gradienten von dezentralen Stößen mit endlicher transversaler Ausdehnung gesehen werden kann. Durch numerische Simulationen erkennen wir, dass der hydrodynamische Fluss nach der Kollision sehr gut durch entsprechende Mittelwerte von symmetrischen Shockwellen approximiert werden kann. Somit verallgemeinern wir das Ergebnis von Chesler, Kilbertus und van der Schee in [2], die eine analytische Form für die Eigenenergie angeben. Folglich können Anfangswerte für hydrodynamische Simulationen gefunden werden, ohne aufwendige numerische Simulationen im Rahmen des holographischen Prinzipzs durchführen zu müssen.

Im zweiten Teil, der auf [3] basiert, beschäftigen wir uns mit Verschränkungsentropie (Entanglement entropy) in $SU(N_c)$ Yang-Mills (YM) Theorien. Verschränkungsentropie kann sowohl im Rahmen des holographischen Prinzipes (für $N_c \to \infty$) als auch mithilfe der Gittereichtheorie (für endliche N_c) berechnet werden.

Die interessante Observable ist die entropische C-Funktion. Das holographische Prinzip sagt hierfür einen Sprung bei einem endlichen Wert der Länge l_c voraus. Wir berechnen diese Observable mithilfe von Gittersimulationen. Wir finden, dass diese anfangs von der Ordnung $\mathcal{O}(N_c^2 - 1)$ ist und dann in einer stetigen Kurve gegen einen Wert, der innerhalb der Fehlergrenzen mit 0 kompatibel ist, abfällt. Dies geschieht für $N_c = 4$ schneller als für $N_c = 3$, was das Szenario eines Sprunges für $N_c \to \infty$ unterstützt.

Contents

This is dedicated to my friends and family. Especially to my grandmother who hoped to see me finish my PhD but sadly passed away a couple of months too early.

Publications

This thesis is based on the following publications:

1. S. Waeber, A. Rabenstein, A. Schäfer, and L. G. Yaffe, "Asymmetric shock-wave collisions in AdS_5", [1906.05086]

2. A. Rabenstein, N. Bodendorfer, P. Buividovich, and A. Schäfer, "Lattice study of Rényi entanglement entropy in $SU(N_c)$ lattice Yang-Mills theory with $N_c = 2, 3, 4$", [1812.04279]

1 Motivation

The aim of (theoretical) physics is to describe nature in the language of mathematics, thereby reproducing existing observations and predicting new ones. Modern physics states that there exist four different types of fundamental interactions, namely gravity, electromagnetism, the weak and the strong force plus possibly still unknown ones. An ultimate goal is to combine these different forces, but there are several reasons why General Relativity (GR) and the Standard Model (SM) cannot be combined straightforwardly. Current experiments of interest for particle physics, which is subject of this thesis, are well below Planck energy and thus gravity is suppressed such that we are left with the SM. Using the language of group theory the SM can be written as the direct product of the gauge groups $SU(3) \times SU(2) \times U(1)$. In this motivation, we will further restrict ourselves to the strong sector, i.e. Quantum Chromo Dynamics (QCD), whose Lagrangian is given by

$$\mathcal{L}_{QCD} = \sum_{\psi} \overline{\psi}_i \left(i\gamma^\mu \left(\partial_\mu \delta_{ij} - igA^a_\mu T^a_{ij} \right) - m_\psi \delta_{ij} \right) \psi_j - \frac{1}{4} F^a_{\mu\nu} F^{\mu\nu}_a. \tag{1.1}$$

One important feature of gauge theories is the running coupling g which means that the coupling itself is not constant due to quantum corrections and thus is dependent on the considered energy scale Q. Usually one defines the β function

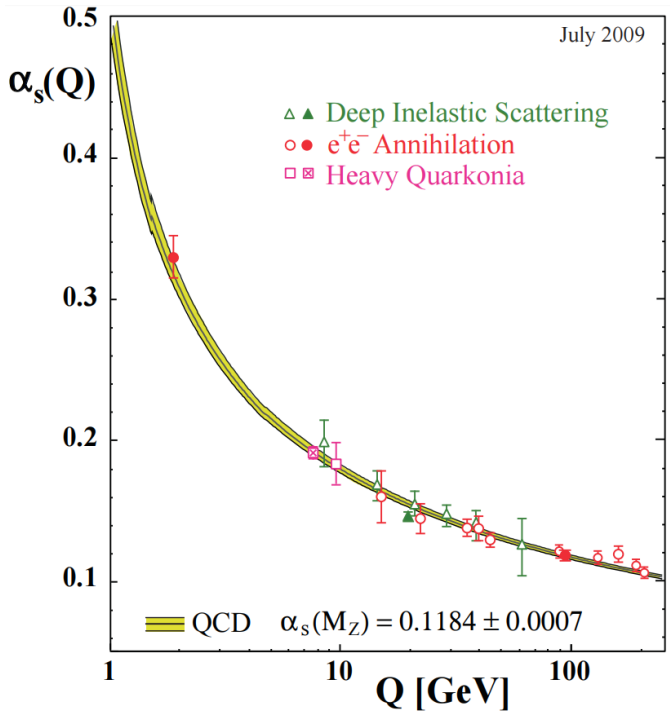

FIGURE 1.1: Running of the coupling for QCD [4]. We see that for small energies the coupling becomes strong and thus PT will fail while for large Q it will converge (asymptotic freedom).

for a coupling g as

$$\beta(g) = \frac{\partial g}{\partial \log Q}. \tag{1.2}$$

For QCD first order Perturbation Theory (PT), i.e. the one-loop calculation, gives

$$\beta(g) = -\left(11 - \frac{n_s}{3} - \frac{2n_f}{3}\right)\frac{g^3}{16\pi^2} \tag{1.3}$$

where n_s is the number of scalar bosons and n_f is the number of flavors. For QCD this behavior is shown in figure 1.1. Since for PT a small coupling is assumed, we can deduce that it will only give reliable results for large Q. If we are interested in smaller Q ($Q \lesssim 1-2\,\mathrm{GeV}$) we have to use non-perturbative techniques. A common approach is Lattice QCD (LQCD) [5]. In this technique, one uses the path integral formalism to calculate expectation values. This leads to an infinite dimensional integral which is then discretized on a finite hypercube and is finally approximated using Monte Carlo techniques. To be able to do so one has to perform a Wick rotation, i.e. to go from real to imaginary time $t \to i\tau$. The Minkowski metric then picks up a minus sign in the time direction such that we end up in flat Euclidean spacetime. This has the disadvantage that we are no more able to calculate dynamical processes. If one is interested in dynamical, non-perturbative quantities,

one has to think about different approaches. One very popular approach is to use the holographic principle which we will explain in greater detail in chapter 2. In 1997 Juan Maldacena made the probably most famous conjecture within the last 30 years [6]. He conjectured that type IIB superstring theory is dynamically equivalent to $\mathcal{N} = 4$ Super Yang-Mills (SYM) theory. As we will see later-on this statement is quite general. For now we will consider the weak form, i.e. the limit of large gauge group $N_c \to \infty$ and large 't Hooft coupling $\lambda \equiv g_{YM}^2 N_c \to \infty$ in SYM which results in Supergravity (SUGRA) on the Anti-de-Sitter (AdS) side of the duality. It can be shown that the resulting Equations of Motion (EoM) are Einstein's equations in five dimensional AdS spacetime.

In chapter 3 we will use this approach to get insight into dynamics in Heavy Ion Collisions (HICs) by solving Einstein's equations numerically. We will use the characteristic formulation to transform the system of coupled non-linear Einstein's equations in a set of nested Ordinary Differential Equations (ODEs). For the very first time, we consider asymmetric shockwave collisions which can be seen as a first approximation for off-center collisions. We analyze the results with respect to hydrodynamization time since this is important for the starting time of hydrodynamic simulations and the formation of the Quark Gluon Plasma (QGP).[1] In [2] Chesler, Kilbertus and van der Schee found an analytic expression for the proper energy density which is needed as initial data for hydrodynamic simulations. We generalize these results to asymmetric shocks by using appropriate averages of symmetric shockwaves. Hence, it is possible to bypass the numerically cumbersome calculation in holography and start with a hydrodynamic time evolution straight away.

Obviously, we made the real world, or – in this case – QCD, more symmetric than it actually is. The holographic principle in its weak form, as we applied it, assumes that the field theory is supersymmetric ($\mathcal{N} = 4$), has infinitely many colors ($N_c \to \infty$), has conformal symmetry, and an infinite 't Hooft coupling ($\lambda \to \infty$). But QCD is different and therefore it is also interesting to see how reliable these results are. Calculating corrections to the holographic principle is feasible but tedious [7–16]. Another possibility to test this conjecture is to consider observables which can be calculated on both sides of the duality. In chapter 4 we will consider entanglement entropy which can be calculated both in holography, via minimal surfaces, and in the boundary Conformal Field Theory (CFT). We will apply the lattice approach to get results for $SU(N_c)$, $N_c \in \{2, 3, 4\}$.

[1] Note that the definition of the QGP is not unique. In LQCD it is defined as the state after thermalization. But here we refer to it as a perfect fluid and hence it is the state after hydrodynamization. It is also shown that the hydrodynamization and the thermalization times are not equal. One is not even sure if the QGP produced in realistic HICs thermalizes at all.

2

Holographic Principle

In this chapter, we will review some basics about the holographic principle which we will use in this thesis. We will start by giving an introduction into string theory, especially starting with the purely bosonic one to get familiar with the concepts in section 2.1. We will then extend these ideas to superstring theory which includes fermionic degrees of freedom and also has a non-tachyonic and stable vacuum in section 2.2 (in contrast to the bosonic case). Afterwards, we will discuss D-branes which are the important objects to motivate the gauge/gravity duality since they deform spacetime to have an AdS geometry and also a $SU(N_c)$ gauge field lives on them (cf. section 2.3). Combining these two facts will give rise to the holographic principle which we introduce in section 2.4.
In section 2.5 we will introduce a topic which is not directly related to string theory and the gauge/gravity duality, but which we will also consider in the analysis of the colliding shockwaves, i.e. hydrodynamics.
This chapter is mainly based on the textbook by Ammon and Erdmenger [17] which we recommend for further study. The introduction to string theory is partially also based on the lecture notes [18]. The section about the holographic principle also uses the introduction of [19] as reference.

2.1 Bosonic String Theory

We will start this chapter by considering bosonic string theory. The main idea of string theory is to extend the concept of point particles to one dimensional objects which are then called strings. As an immediate consequence, the trajectory of the point particle which is one dimensional, is called worldline and can be parametrized by proper time τ, becomes a two dimensional object which is called worldsheet. Obviously, we need two parameters to describe this. We use the proper time τ and a spatial parameter σ. For brevity, we use several notations throughout this chapter and it will be obvious from the context which one we mean, i.e. we write $\sigma = (\sigma^0, \sigma^1) = (\tau, \sigma)$.

2.1.1 Nambu-Goto and Polyakov Action

To start with, we have to embed the two dimensional worldsheet Σ in a D dimensional flat target space, we do this by introducing embedding functions $X^\mu(\tau, \sigma)$. The simplest parameterization invariant form is the Nambu-Goto (NG) action given by

$$S_{NG} = -\frac{1}{2\pi\alpha'} \int_\Sigma d^2\sigma \, \sqrt{-\det \gamma}. \tag{2.1}$$

In this formula $\gamma_{ab} = \partial_a X^\mu \partial_b X_\mu$ is the induced metric which is the pull-back of the spacetime metric on the worldsheet.[1] The prefactor can be written as the tension T of the string, i.e. $T = \frac{1}{2\pi\alpha'}$. The parameter α' is related to the string length l_s as $\alpha' = l_s^2$.
Due to the square root in this action, it is hard to perform computations. But it is possible to circumvent this problem by introducing an auxiliary field, namely the worldsheet metric h_{ab}. With this field, we arrive at the Polyakov action

$$S_P = -\frac{1}{4\pi\alpha'} \int_\Sigma d^2\sigma \, \sqrt{-h} h^{ab} \gamma_{ab}. \tag{2.2}$$

First of all, we want to show that these two equations are indeed the same and thus look at the variation of the action with respect to the auxiliary worldsheet metric h_{ab}, i.e.

$$\frac{\delta S}{\delta h^{ab}} = -\frac{1}{4\pi\alpha'} \int_\Sigma d^2\sigma \, \sqrt{-h} \left(\gamma_{ab} - \frac{1}{2} h_{ab} h^{cd} \gamma_{cd} \right) \stackrel{!}{=} 0. \tag{2.3}$$

[1] In this introduction to string theory we will label the worldsheet coordinates by Roman letters a, b, ... while we denote the spacetime coordinates by Greek letters μ, ν, ... Later in this chapter we will also use Roman letters i, j, ... for labeling spatial directions in spacetime.

For further discussion, it is convenient to rewrite this in the following form

$$h_{ab} = 2f(\sigma)\gamma_{ab} \tag{2.4}$$

with the conformal factor $f(\sigma)$ being defined by $f(\sigma)^{-1} = h^{cd}\gamma_{cd}$. Inserting this in the Polyakov action (2.2) we recover the NG action (2.1) by noting that we get a factor of $f(\sigma)$ from the determinant and a factor of $f(\sigma)^{-1}$ from the inverse metric which then cancels exactly. Thus these two actions (2.1) and (2.2) are the same at classical level.

Since we introduced the worldsheet metric as an auxiliary field we have additional constraints on the EoM which are the so-called Virasoro constraints and come from the requirement that the worldsheet energy-momentum tensor vanishes, i.e.

$$T_{ab} = \frac{4\pi\alpha'}{\sqrt{-h}}\frac{\delta S}{\delta h^{ab}} = \gamma_{ab} - \frac{1}{2}h_{ab}h^{cd}\gamma_{cd} = 0. \tag{2.5}$$

Let us next have a look at the symmetries of the Polyakov action.

D-dimensional Poincaré invariance Since we started in D dimensional Minkowski space and we did not change anything there, the embedding functions $X^\mu(\sigma)$ are still invariant under Lorentz transformations $\Lambda^\mu{}_\nu$ and translations e^μ while the worldsheet metric is kept fixed, i.e.

$$X^\mu \to \Lambda^\mu{}_\nu X^\nu + e^\mu, \quad h^{ab} \to h^{ab}. \tag{2.6}$$

Reparametrization invariance/diffeomorphisms The action is also invariant under reparametrizations of the worldsheet coordinates σ. If we consider a coordinate change in the worldsheet $\sigma^a \to \tilde{\sigma}^a = f^a(\sigma)$, the embedding functions transform as scalars while the worldsheet metric transform as a rank 2 tensor, i.e.

$$X^\mu(\sigma) \to \tilde{X}^\mu(\tilde{\sigma}) = X^\mu(\sigma), \quad h_{ab}(\sigma) \to \tilde{h}_{ab}(\tilde{\sigma}) = \frac{\partial f^c}{\partial\sigma^a}\frac{\partial f^d}{\partial\sigma^b}h_{cd}(\sigma). \tag{2.7}$$

Weyl invariance The worldsheet metric is also invariant under multiplication by conformal factors, as we have already seen above when showing that the Polyakov action coincides with the NG one, i.e. the factor $f(\sigma)$ canceled. We can write this as

$$X^\mu(\sigma) \to X^\mu(\sigma), \quad h_{ab}(\sigma) \to \Omega^2(\sigma)h_{ab}(\sigma) = e^{2\omega(\sigma)}h_{ab}(\sigma). \tag{2.8}$$

Due to these local symmetries we can choose a gauge. We will use the conformal gauge from now on, i.e. we choose

$$h_{ab} = e^{2\omega(\sigma)}\eta_{ab}, \quad \eta_{ab} = \mathrm{diag}(-1, 1). \tag{2.9}$$

Remarkably we could further use the Weyl invariance to set $\omega \equiv 0$ and hence end up with a flat worldsheet metric with Minkowski signature. Using this gauge the Polyakov action (2.2) simplifies to

$$S_P = -\frac{1}{4\pi\alpha'}\int d^2\sigma \, \left(-\left(\partial_\tau X^\mu\right)\left(\partial_\tau X_\mu\right) + \left(\partial_\sigma X^\mu\right)\left(\partial_\sigma X_\mu\right)\right). \tag{2.10}$$

We can apply the variational principle to arrive at the EoM

$$\left(\partial_\tau^2 + \partial_\sigma^2\right) X^\mu(\sigma) = \partial_+\partial_- X^\mu = 0 \tag{2.11}$$

where we introduced lightcone coordinates $\sigma_\pm = \tau \pm \sigma$ and corresponding derivative $\partial_\pm = \frac{\partial}{\partial\sigma_\pm}$.
As usual for the application of the variational principle we pick up a boundary term which vanishes for point particles, but for strings there are boundary terms in the spatial dimension which do not vanish automatically, i.e. we have to demand that a string spanning from 0 to σ_0 satisfies

$$\partial_\sigma X^\mu \delta X_\mu\Big|_0^{\sigma_0} = 0. \tag{2.12}$$

Equation (2.11) is a simple wave equation but we must not forget that we have to satisfy the Virasoro constraint (2.5), too. In the conformal gauge, this constraint reads

$$T_{01} = \dot{X}^\mu \cdot X'_\mu = 0, \quad T_{00} = T_{11} = \frac{1}{2}\left(\dot{X}^2 + X'^2\right) = 0 \tag{2.13}$$

or, in lightcone coordinates

$$T_{++} = \partial_+ X^\mu \partial_+ X_\mu = 0, \quad T_{--} = \partial_- X^\mu \partial_- X_\mu = 0, \quad T_{+-} = T_{-+} = 0. \tag{2.14}$$

2.1.2 Solving the Wave Equation

To solve the wave equation in lightcone gauge we see that we can split the solution in a left- and right-moving part, i.e.

$$X^\mu(\sigma) = X_L^\mu(\sigma_+) + X_R^\mu(\sigma_-). \tag{2.15}$$

We can write a general ansatz as a Fourier expansion, i.e.

$$X_L^\mu(\sigma_+) = \frac{\tilde{x}_0^\mu}{2} + \frac{\alpha'}{2}\tilde{p}^\mu\sigma_+ + i\sqrt{\frac{\alpha'}{2}}\sum_{n\neq 0}\frac{1}{n}\tilde{\alpha}_n^\mu e^{-in\sigma_+}, \tag{2.16a}$$

$$X_R^\mu(\sigma_-) = \frac{x_0^\mu}{2} + \frac{\alpha'}{2}p^\mu\sigma_- + i\sqrt{\frac{\alpha'}{2}}\sum_{n\neq 0}\frac{1}{n}\alpha_n^\mu e^{-in\sigma_-}. \tag{2.16b}$$

For later convenience we further define $\alpha_0^\mu = \sqrt{\frac{\alpha'}{2}}p^\mu$ and $\tilde{\alpha}_0^\mu = \sqrt{\frac{\alpha'}{2}}\tilde{p}^\mu$. Since the embedding functions $X^\mu(\sigma)$ have to be real, we can deduce that $\alpha_{-n}^\mu = (\alpha_n^\mu)^*$ and $\tilde{\alpha}_{-n}^\mu = (\tilde{\alpha}_n^\mu)^*$.

With this ansatz for the solution of the wave equation (2.11), we can now continue with the implementation of the boundary term (2.12). Obviously, there exist several possibilities to satisfy this equation. First of all, we distinguish between closed and open strings.

Closed strings For closed strings, we choose the endpoint of the string $\sigma_0 = 2\pi$ for convenience. As the name suggests we identify the string start and end point with each other, i.e.

$$X^\mu(\tau,0) = X^\mu(\tau,2\pi), \quad \partial_\sigma X^\mu(\tau,0) = \partial_\sigma X^\mu(\tau,2\pi), \tag{2.17a}$$

$$\gamma_{ab}(\tau,0) = \gamma_{ab}(\tau,2\pi). \tag{2.17b}$$

In the ansatz (2.16) for the solution of the wave equation, this results in the requirement that $\tilde{p}^\mu = p^\mu$. Furthermore, it is convenient to also identify $\tilde{x}_0^\mu$ with x_0^μ. The constraint (2.12) is then automatically satisfied.

Open strings The other possibility is that the endpoints of the string do not coincide. To get simpler results, we choose $\sigma_0 = \pi$ in this case. In the case of open strings, it is obvious that there are two possibilities to satisfy (2.12) on each endpoint of the string independently. Let us further denote the endpoint by $\overline{\sigma}$, i.e. $\overline{\sigma} \in \{0, \pi\}$.

Neumann boundary conditions

$$\partial_\sigma X^\mu(\tau,\overline{\sigma}) = 0. \tag{2.18}$$

Dirichlet boundary conditions

$$\delta X^\mu(\tau,\overline{\sigma}) = 0. \tag{2.19}$$

We are free to choose any of these boundary conditions in each dimension, except for the time direction where we have to implement Neumann bound-

ary conditions, since otherwise the string would not evolve in time. Again the choice of boundary conditions gives constraints for the ansatz (2.16).

Let us, for example, have a look at open strings which satisfy Dirichlet boundary conditions at both ends. This means that the endpoints of the string are fixed for all τ, i.e. $X^\mu(\tau,0) = x_i^\mu$ and $X^\mu(\tau,\pi) = x_f^\mu$. With this choice, the ansatz (2.16) reads

$$X^\mu(\tau,\sigma) = x_i^\mu + \frac{1}{\pi}\left(x_f^\mu - x_i^\mu\right) + \sqrt{2\alpha'}\sum_{n\neq 0}\frac{\alpha_n^\mu}{n}e^{-in\tau}\sin(n\sigma). \tag{2.20}$$

Defining the momentum as the integral over the canonical momentum, i.e.

$$p^\mu = \int_0^\pi d\sigma\,\Pi^\mu(\tau,\sigma) = \int_0^\pi d\sigma\,\frac{\partial_\tau X^\mu(\tau,\sigma)}{2\pi\alpha'}, \tag{2.21}$$

we see that this is not conserved. This can also already be seen by the fact that by the choice of Dirichlet boundary conditions we explicitly broke the translation invariance. This invariance is always related to momentum conservation through the Noether theorem. Hence, it is reasonable to ask where the momentum goes. As shown in figure 2.1 the string is attached to a hypersurface which is called Dirichlet or short D-brane. Since the momentum of the string is not conserved these hypersurfaces have to be dynamical and also contribute to the total momentum. We will come back to these D-branes in section 2.3.
To continue we write down the Virasoro constraint (2.5) which has to be satisfied

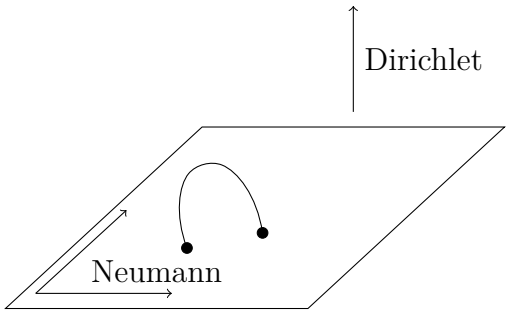

FIGURE 2.1: String with different boundary conditions in different directions. The directions orthogonal to directions with Dirichlet boundary conditions span a hyperplane (D-brane). Along the directions of this D-brane Neumann boundary conditions are implemented. In this setup Dirichlet boundary conditions where applied such that $x_i^\mu = x_f^\mu$.

for open strings

$$T_{--} = T_{++} = (\partial_+ X^\mu)(\partial_+ X_\mu) = \frac{\alpha'}{2}\sum_m \sum_n \alpha_n^\mu \alpha_{m,\mu} e^{-i(m+n)\sigma_+}$$
$$= \alpha' \sum_m L_m e^{-in\sigma_+} \tag{2.22}$$

where we introduced the Virasoro numbers

$$L_m = \frac{1}{2}\sum_n \alpha_n^\mu \alpha_{m-n,\mu} \quad \forall m. \tag{2.23}$$

For closed strings both oscillation modes α_n^μ and $\tilde{\alpha}_n^\mu$ survive and hence we have two types of Virasoro numbers given by L_n and $\tilde{L}_n$ which have to vanish. Hence, it follows that we have to implement $L_m = 0$ in the open string sector, while for closed strings we have to require that $\tilde{L}_m = L_m = 0$ for all m.

2.1.3 Quantizing Bosonic Strings

A theory can be quantized by promoting fields to operators and then requiring that they satisfy certain commutation relations. For bosonic string theory, we require that the standard canonical equal time commutation relations are satisfied, i.e.

$$\left[\hat{X}^\mu(\tau,\sigma), \hat{\Pi}^\nu(\tau,\sigma')\right] = i\eta^{\mu\nu}\delta(\sigma - \sigma') \tag{2.24}$$

where the conjugate momentum is given by $\Pi^\nu(\tau,\sigma) = \frac{\partial_\tau X^\mu(\tau,\sigma)}{2\pi\alpha'}$.
Let us quantize open strings as an example since we just have one Virasoro constraint to satisfy and hence the notation is shorter. We start by introducing creation and annihilation operators like for the harmonic oscillator. We define

$$\hat{a}_m^\mu = \frac{1}{\sqrt{m}}\hat{\alpha}_m^\mu, \quad \hat{a}_m^{\mu\dagger} = \frac{1}{\sqrt{m}}\hat{\alpha}_{-m}^\mu \quad \forall\ m > 0. \tag{2.25}$$

From expansion (2.16) and the canonical commutation relation, we straightforwardly see that

$$\left[\hat{a}_m^\mu, \hat{a}_n^{\nu\dagger}\right] = \eta^{\mu\nu}\delta_{mn}, \quad [\hat{a}_m^\mu, \hat{a}_n^\nu] = \left[\hat{a}_m^{\mu\dagger}, \hat{a}_n^{\nu\dagger}\right] = 0. \tag{2.26}$$

Note that due to the Minkowski signature of the metric $\left[\hat{a}_m^0, \hat{a}_m^{0\dagger}\right] = -1$ and hence we have negative norm states in the Hilbertspace. This results in the failure of the probability interpretation of the norm. Such states also occur in other gauge theories and one solves this by fixing the gauge symmetries. In this case, the relevant symmetries are the reparametrization and Weyl invariance which we

fixed by choosing the conformal gauge and finally, we ended up with the Virasoro constraint (2.14). This constraint can be solved easily in lightcone coordinates $X^{\pm} = X^0 \pm X^{D-1}$ and by setting

$$\hat{X}^+ = \hat{x}_0^+ + 2\alpha' \hat{p}^+ \tau. \tag{2.27}$$

With this, we can solve the Virasoro constraint (2.5) for X^- as a function of X^i $(i = 1, \ldots, D-2)$, X^+ and a constant x_0^-. Hence the dynamical degrees of freedom are given by $\hat{p}^+$, $\hat{x}_0^-$, $\hat{p}^i$, $\hat{a}_m^i$ and $\hat{a}_m^{i\dagger}$ which satisfy the above commutation relations. Next, we can label states by the eigenvalue of the number operator $\hat{N} = \sum_{i=1}^{D-2} \sum_{n=1}^{\infty} n \hat{a}_n^{\mu} \hat{a}_{n,\mu}^{\dagger}$ and the momentum operator $\hat{p}^{\mu}$, i.e. $|N, k\rangle$. The vacuum $|0, k\rangle$ is then defined as

$$\hat{p}^{\mu} |0, k\rangle = k^{\mu} |0, k\rangle , \quad \hat{a}_m^i |0, k\rangle = 0. \tag{2.28}$$

As usual for creation and annihilation operators, all excited states can then be constructed by multiplying them with the appropriate number of creation operators

$$|N, k\rangle = \left(\prod_{i=1}^{D-2} \prod_{n=1}^{\infty} \frac{\left(\hat{a}_n^{i\dagger}\right)^{N_{in}}}{\sqrt{N_{in}!}} \right) |0, k\rangle . \tag{2.29}$$

Here we introduce the occupation number for each mode N_{in} given by

$$\hat{a}_n^i \hat{a}_n^{i\dagger} |N, k\rangle = N_{in} |N, k\rangle \quad \text{(no summation over } i\text{)}. \tag{2.30}$$

Next we have to quantize the Virasoro constraint which is equivalent to construct consistent operators for $\hat{L}_m$ (cf. equation (2.23)). If $m \neq 0$ we can simply replace α_m^i by the operators $\hat{a}_m^i$, but for $\hat{L}_0$ ordering ambiguities arise. To take care of this we start with the naive ordering, i.e.

$$\begin{aligned} \hat{L}_0 &= \alpha' \hat{p}^{\mu} \hat{p}_{\mu} + \frac{1}{2} \sum_{i=1}^{D-2} \sum_{n \neq 0}^{\infty} \hat{\alpha}_n^{\mu} \hat{\alpha}_{-n,\mu} \\ &= \alpha' \hat{p}^{\mu} \hat{p}_{\mu} + \frac{1}{2} \sum_{i=1}^{D-2} \left(\sum_{n>0} n \hat{a}_n^{\mu} \hat{a}_{n,\mu}^{\dagger} + \sum_{n<0} n \hat{a}_n^{\mu\dagger} \hat{a}_{n,\mu} \right). \end{aligned} \tag{2.31}$$

In the end, we want to have normal-ordering of the creation and annihilation operator such that the action on the vacuum does not vanish, i.e. we have to commute the operators in the last term

$$\hat{a}_n^{\mu\dagger} \hat{a}_{n,\mu} = \hat{a}_{n,\mu} \hat{a}_n^{\mu\dagger} - \delta_{nn}. \tag{2.32}$$

Hence we can write L_0 as

$$\hat{L}_0 = \alpha' \hat{p}^\mu \hat{p}_\mu + \sum_{i=1}^{D-2} \sum_{n=1}^{\infty} n \hat{a}_n^\mu \hat{a}_{n,\mu}^\dagger + \underbrace{\frac{D-2}{2} \sum_{n=1}^{\infty} n}_{a}. \tag{2.33}$$

The term a seems to diverge in first place, but this can be regularized by removing the leading divergence such that[2]

$$a = -\frac{D-2}{24}. \tag{2.34}$$

By using the number operator $\hat{N}$ introduced above we can finally write $\hat{L}_0$ as

$$\hat{L}_0 = \alpha' \hat{p}^\mu \hat{p}_\mu + \hat{N} + \frac{2-D}{24}. \tag{2.35}$$

Since for any physical state $|\psi\rangle$ the Virasoro constraint has to be satisfied, i.e. $\hat{L}_0 |\psi\rangle = 0$, we can calculate the mass squared eigenvalues via $M^2 = -k^\mu k_\mu$ from this requirement and eventually arrive at

$$M^2 = \frac{1}{\alpha'} \left(N + \frac{2-D}{24} \right). \tag{2.36}$$

Let us briefly discuss the vacuum state for bosonic string theory, i.e. $N = 0$. We see that for $D > 2$, M^2 is negative and hence the vacuum is tachyonic. It is not known up to now if a stable vacuum exists in bosonic string theory. In contrast, one knows that for superstring theory using the GSO projection (cf. section 2.2) a stable vacuum exists.

Let us continue by looking at the first excited states, i.e. $N = 1$. We see that $M^2 = \frac{26-D}{\alpha'}$ and the corresponding states are obtained by applying one creation operator on the vacuum state, i.e. $a_1^{i\dagger} |0, k\rangle$. Since the index $i = 1, \ldots, D-2$ this transforms under $SO(D-2)$ and not under the full group $SO(D-1)$ as it should for a massive particle. The same phenomenon occurs in other gauge theories like Quantum Electro Dynamics (QED) where the massless photon has only two polarizations instead of three for a massive particle. This is because the photon does not have a rest frame. Reverting this argument we can conclude that the first excited state in bosonic string theory has to be massless and hence the

[2]This can be shown e.g. by considering $\sum_{n=1}^{\infty} n = \lim_{\epsilon \to 0} \left(-\frac{\partial}{\partial \epsilon} \sum_{n=1}^{\infty} e^{-\epsilon n} \right)$. We can then use the geometric series and Taylor the expression to obtain

$$\sum_{n=1}^{\infty} n = \lim_{\epsilon \to 0} \left(\frac{1}{\epsilon^2} - \frac{1}{12} + \mathcal{O}\left(\epsilon^2\right) \right).$$

dimension is fixed to be

$$D = 26. \tag{2.37}$$

This argument is a bit hand-waving but one can show that the requirement of Poincaré invariance at quantum level leads to the same dimensionality.
Analogous considerations are possible for closed strings where we have two Virasoro constraints to be satisfied ($\hat{L}_m$ and $\hat{\tilde{L}}_m$). We find that the vacuum is again tachyonic and unstable. The first excited state and its mass squared are given by

$$M^2 = \frac{26 - D}{6\alpha'}, \quad \hat{a}_1^i \hat{\tilde{a}}_1^j \left|0, 0, k\right\rangle . \tag{2.38}$$

In $D = 26$ this gives rise to a massless rank 2 tensor since we have two indices i, j. This tensor can be decomposed in a traceless symmetric tensor which we can identify with the graviton, an antisymmetric tensor identified with a Kalb-Ramond field and a scalar to be identified with the dilaton. From this, we can conclude that gravity emerges if we couple these excitations to fundamental strings.
We will show this by first identify the symmetric traceless part with the metric $g_{\mu\nu}(X)$ which now can differ from the flat Minkowski metric, i.e. the Polyakov action now reads

$$S_P = -\frac{1}{4\pi\alpha'} \int_\Sigma d^2\sigma \sqrt{-h} h^{ab} \left(\partial_a X^\mu\right) \left(\partial_b X^\nu\right) g_{\mu\nu}(X). \tag{2.39}$$

Additionally, we have the Kalb-Ramond field and the dilaton whose action is given by

$$S_{B,\Phi} = -\frac{1}{4\pi\alpha'} \int d^2\sigma \sqrt{-h} \left(\epsilon^{ab} \left(\partial_a X^\mu\right) \left(\partial_b X^\nu\right) B_{\mu\nu}(X) + \alpha' R_{(h)} \Phi(X)\right) \tag{2.40}$$

where $R_{(h)}$ is the Ricci scalar of the worldsheet. Of course, this action has to be still Weyl invariant and hence we have to require that the worldsheet energy-momentum tensor is traceless, i.e. $T^a_{\ a} = 0$. Calculating this tensor from the action by variation with respect to the metric we arrive at the following equation

$$T^a_{\ a} = -\frac{1}{2\alpha'} \beta^g_{\mu\nu} h^{ab} \left(\partial_a X^\mu\right) \left(\partial_b X^\nu\right) - \frac{1}{2\alpha'} \beta^B_{\mu\nu} \epsilon^{ab} \left(\partial_a X^\mu\right) \left(\partial_b X^\nu\right) - \frac{1}{2} \beta^\Phi R_{(h)}. \tag{2.41}$$

The β functions in order α' are given by

$$\beta^g_{\mu\nu} = -\alpha' \left(R_{\mu\nu} - 2\nabla_\mu \nabla_\nu - \frac{1}{4} H_{\mu\rho\lambda} H_\nu{}^{\rho\lambda} \right), \tag{2.42a}$$

$$\beta^B_{\mu\nu} = \alpha' \left(-\frac{1}{2} \nabla^\lambda H_{\lambda\mu\nu} + \left(\nabla^\lambda \Phi \right) H_{\lambda\mu\nu} \right), \tag{2.42b}$$

$$\beta^\Phi = \alpha' \left(\frac{D-26}{6\alpha'} - \frac{1}{2} \nabla^2 \Phi + \left(\nabla_\mu \Phi \right) \left(\nabla^\mu \Phi \right) - \frac{1}{24} H_{\mu\nu\lambda} H^{\mu\nu\lambda} \right) \tag{2.42c}$$

where we introduced the field strength $H = \mathrm{d}B$ for the Kalb-Ramond field given by

$$H_{\mu\nu\lambda} = \partial_\mu B_{\nu\lambda} + \partial_\nu B_{\lambda\mu} + \partial_\lambda B_{\mu\nu}. \tag{2.43}$$

Since all the terms in (2.41) are linearly independent each of the β functions has to vanish independently.
The interesting point here is that this all can be written down as an effective action in the D dimensional target space. For bosonic string theory, this effective action reads

$$S = \frac{1}{2\tilde{\kappa}^2} \int d^D x \, \sqrt{-g} e^{-2\Phi} \Bigg(R + 4 \left(\nabla_\mu \Phi \right) \left(\nabla^\mu \Phi \right) - \frac{1}{12} H_{\mu\nu\lambda} H^{\mu\nu\lambda} - \frac{2(D-26)}{3\alpha'} + \mathcal{O}\left(\alpha'\right) \Bigg). \tag{2.44}$$

This is an action only in target space for which we can derive EoM for all the fields involved. This is valid if only massless closed strings contribute, i.e. for small α'.
This closes our review of bosonic string theory. In the next section, we will extend this discussion to fermionic degrees of freedom and hence additionally require Supersymmetry (SUSY).

2.2 Superstring Theory

In this section, we want to extend bosonic string theory as it has two disadvantages. First of all, it has an unstable, tachyonic vacuum and there exist no fermions in the spectrum. Hence, we additionally require SUSY in the string theory. In principle, we will perform the same steps as before and therefore we will be quite brief in this section.
SUSY is the extension of the Poincaré group and it equals the number of bosonic and fermionic degrees of freedom. Hence, we start by introducing anti-commuting fermionic fields ψ^μ on top of the bosonic ones. Therefore the generalization of the

Polyakov action (2.2) in conformal gauge reads

$$S = -\frac{1}{4\pi a'} \int d^2\sigma \, \eta^{ab} \left((\partial_a X^\mu) (\partial_b X^\nu) + i \bar{\psi}^\mu \gamma_a \partial_b \psi^\nu \right) \eta_{\mu\nu}(X) \tag{2.45}$$

where $\bar{\psi}^\mu = (\psi^\mu)^T \gamma^0$ and γ^1 denote the worldsheet Dirac matrices

$$\gamma^0 = \begin{pmatrix} 0 & -i \\ i & 0 \end{pmatrix}, \quad \gamma^1 = \begin{pmatrix} 0 & i \\ i & 0 \end{pmatrix}. \tag{2.46}$$

Choosing the fermionic fields to be Majorana spinors, i.e. $\psi^\mu = (\psi^\mu_-, \psi^\mu_+)$ with real components $\psi^\mu_\pm$ the fermionic part of the action can be written as

$$S_f = \frac{i}{4\pi\alpha'} \int d^2\sigma \ (\psi^\mu_- \partial_+ \psi_{-\mu} + \psi^\mu_+ \partial_- \psi_{+\mu}) \tag{2.47}$$

with $\partial_\pm = \partial_\tau \pm \partial_\sigma$. For the bosonic part of the action, the same procedure as described above in section 2.1 applies and thus we will focus on the fermionic part from now on. As usual, we apply the variational principle to arrive at the EoM for the fermionic fields given by

$$\partial_+ \psi^\mu_- = \partial_- \psi^\mu_+ = 0. \tag{2.48}$$

Again we obtain a simple wave equation for the fermionic coordinate functions. As in the bosonic case, we pick up a boundary term which we have to require that it vanishes. It can be written as

$$\delta S_f = \frac{i}{4\pi\alpha'} \int d\tau \ (\psi^\mu_- \delta\psi_{-\mu} - \psi^\mu_+ \delta\psi_{+\mu}) \Big|_{\sigma=0}^{\sigma=\pi}. \tag{2.49}$$

Once more there exist two kinds of strings, namely open and closed ones. We will start to derive the spectrum for the open strings. In this case, the boundary term (2.49) has to vanish for both ends independently. Setting again $\overline{\sigma} \in \{0, \pi\}$, it follows

$$\psi^\mu_- \delta\psi_{-\mu} - \psi^\mu_+ \delta\psi_{+\mu} \Big|_{\sigma=\overline{\sigma}} = 0 \Leftrightarrow \delta \left(\psi^\mu_-\right)^2 \Big|_{\sigma=\overline{\sigma}} = \delta \left(\psi^\mu_+\right)^2 \Big|_{\sigma=\overline{\sigma}}. \tag{2.50}$$

The overall sign of the fields does not matter and thus we are able to freely choose $\psi^\mu_-(\tau, 0) = \psi^\mu_+(\tau, 0)$. For the other end of the string ($\sigma = \pi$), we then have two different possibilities leading to the Ramond (R) and the Neveu-Schwarz (NS)

sector of superstring theory, i.e.

$$\text{R} \quad : \quad \psi_+^\mu(\tau,\pi) = +\,\psi_-^\mu(\tau,\pi), \tag{2.51a}$$

$$\text{NS} \quad : \quad \psi_+^\mu(\tau,\pi) = -\,\psi_-^\mu(\tau,\pi). \tag{2.51b}$$

As in the last section, the wave equation (2.48) can be solved by expanding the fields in Fourier modes

$$\text{R} \quad : \quad \psi_\pm^\mu(\tau,\sigma) = \frac{1}{\sqrt{2}} \sum_{n\in\mathbb{Z}} d_n^\mu e^{-in\sigma_+}, \tag{2.52a}$$

$$\text{NS} \quad : \quad \psi_\pm^\mu(\tau,\sigma) = \frac{1}{\sqrt{2}} \sum_{r\in\mathbb{Z}-\frac{1}{2}} b_r^\mu e^{-ir\sigma_+}. \tag{2.52b}$$

The nature of fermionic degrees of freedom is preserved by using Grassmanian Fourier coefficients d_n^μ and b_r^μ. Hence, they satisfy the anti-commutation relations

$$\{d_m^\mu, d_n^\nu\} = \eta^{\mu\nu}\delta_{m,-n} \quad , \quad \{b_r^\mu, b_s^\nu\} = \eta^{\mu\nu}\delta_{r,-s}. \tag{2.53}$$

As in the last section the next step is to quantize the theory. To do so, we promote d_n^μ and b_r^μ to operators and require the canonical commutation relations as in the bosonic case.
Afterwards, we can calculate the first excited state for example in the NS sector $b^i_{-\frac{1}{2}}\left|0\right\rangle_{NS}$ to obtain the mass squared operator

$$M^2 = \frac{1}{\alpha'}\left(\frac{1}{2} - \frac{D-2}{16}\right). \tag{2.54}$$

With the same reasoning as in the bosonic case, we can conclude that the first excited state has to be massless and hence we fixed the dimension to be

$$D = 10 \tag{2.55}$$

for superstring theory.
The vacuum in the NS sector is still tachyonic since $M^2 = -\frac{1}{2\alpha'}$ and in the R sector both chiralities are present. To circumvent these issues we use the GSO (Gliozzi, Scherk and Olive) projection which projects out all tachyonic states and equals the number of fermions and bosons in each state. This is done by introducing the fermion number $\exp(i\pi F) = \pm 1$. The lowest lying states are displayed in table 2.1. We have representations of the group $SO(D-2) = SO(8)$ since we have one open index $i = 1, \ldots, D-2$ for the states $b^i_{-\frac{1}{2}}\left|0\right\rangle_{NS}$ and $d_1^i\left|0\right\rangle_R$.
For closed strings, we can use right- and left-moving solutions both from the Ramond and the Neveu-Schwarz sector independently. We have the following

Sector	$\exp(i\pi F)$	$SO(8)$ repr.	M^2
NS	$+$	$\mathbf{8_v}$	0
NS	$-$	$\mathbf{1}$	$-\frac{1}{2\alpha'}$
R	$+$	$\mathbf{8}$	0
R	$-$	$\mathbf{8'}$	0

TABLE 2.1: Lowest lying string states in superstring theory.

statistics for the spacetime coordinates: NS-NS/R-R are spacetime bosons and NS-R/R-NS are spacetime fermions. From this, we can construct several string theories. For the gauge/gravity duality two of them are important. They are denoted by type IIA and type IIB and contain the following sectors

$$\text{Type IIA} \quad : \quad (\text{NS}+,\text{NS}+)\ ,\ (\text{R}+,\text{NS}+)\ ,\ (\text{NS}+,\text{R}-)\ ,\ (\text{R}+,\text{R}-) \tag{2.56a}$$

$$\text{Type IIB} \quad : \quad (\text{NS}+,\text{NS}+)\ ,\ (\text{R}+,\text{NS}+)\ ,\ (\text{NS}+,\text{R}+)\ ,\ (\text{R}+,\text{R}+) \tag{2.56b}$$

where $\pm$ denotes the fermion number $e^{i\pi F}$. Coupling the lowest lying states for each of the combinations can be written as a direct product of groups, which we can then transform to direct sums. For example, the (NS+,NS+) term is given by

$$\mathbf{8}_\text{v} \otimes \mathbf{8}_\text{v} = \mathbf{1} \oplus \mathbf{28} \oplus \mathbf{35}. \tag{2.57}$$

Doing this for all possibilities for the different types of string theories, we arrive at

$$\text{Type IIA} \quad : \quad \mathbf{1} \oplus \mathbf{8_v} \oplus \mathbf{28} \oplus \mathbf{56_t} \oplus \mathbf{35} \oplus \mathbf{8} \oplus \mathbf{8'} \oplus \mathbf{56} \oplus \mathbf{56'}, \tag{2.58a}$$

$$\text{Type IIB} \quad : \quad \mathbf{1}^2 \oplus \mathbf{28}^2 \oplus \mathbf{35} \oplus \mathbf{35}_+ \oplus \mathbf{8'}^2 \oplus \mathbf{56}^2. \tag{2.58b}$$

As we did for bosonic string theory, we can write down an action which we require to satisfy local SUSY. From this, we can read off that the worldsheet energy-momentum tensor has to vanish, i.e. $T_{ab} = 0$. Analogously we obtain β functions which have to vanish. From this, we can then write down an effective low energy action which is the SUGRA action. For type IIA one obtains in the string frame

$$S_{IIA} = \frac{1}{2\kappa_{10}^2}\Bigg[\int d^{10}x\,\sqrt{-g}\Big(e^{-2\phi}\left(R + 4\left(\partial_\mu\phi\right)\left(\partial^\mu\phi\right) - \frac{1}{2}\left|H_{(3)}\right|^2\right) - \frac{1}{2}\left|F_{(2)}\right|^2 - \frac{1}{2}\left|\tilde{F}_{(4)}\right|^2\Big) - \frac{1}{2}\int B \wedge F_{(4)} \wedge F_{(4)}\Bigg] \tag{2.59}$$

with

$$\tilde{F}_{(4)} = dA_{(3)} - A_{(1)} \wedge F_{(3)}. \tag{2.60}$$

With the notation $\left|F_{(p)}\right|^2$ we mean

$$\int d^{10}x\,\sqrt{-g}\left|F_{(p)}\right|^2 = \frac{1}{p!}\int d^{10}x\,\sqrt{-g}F_{(p)\,\mu_1\ldots\mu_p}F_{(p)}^{\mu_1\ldots\mu_p}. \tag{2.61}$$

For type IIB the action reads

$$S_{IIB} = \frac{1}{2\kappa_{10}^2}\Bigg[\int d^{10}x\,\sqrt{-g}\Bigg(e^{-2\phi}\left(R + 4\left(\partial_\mu\phi\right)\left(\partial^\mu\phi\right) - \frac{1}{2}\left|H_{(3)}\right|^2\right) \tag{2.62}$$

$$- \frac{1}{2}\left|F_{(1)}\right|^2 - \frac{1}{2}\left|\tilde{F}_{(3)}\right|^2 - \frac{1}{4}\left|\tilde{F}_{(5)}\right|^2\Bigg)\Bigg] \tag{2.63}$$

$$- \frac{1}{2}\int C_{(4)}\wedge H_{(3)}\wedge F_{(3)} \tag{2.64}$$

with

$$F_{(p)} = dC_{(p-1)}, \quad H_{(3)} = dB_{(2)}, \quad \tilde{F}_{(3)} = F_{(3)} - C_{(0)}H_{(3)}, \tag{2.65}$$

$$\tilde{F}_{(5)} = F_{(5)} - \frac{1}{2}C_{(2)}\wedge H_{(3)} + \frac{1}{2}B_{(2)}\wedge F_{(3)}. \tag{2.66}$$

Additionally the 5-form has to be self-dual, i.e.

$$*\tilde{F}_{(5)} = \tilde{F}_{(5)} \tag{2.67}$$

where $*$ is the Hodge star operator.
So we finally arrived at the low energy effective action for superstring theory. This is an action which only has fields living in the target spacetime. In the next section, we will consider D-branes which we already shortly touched in the context of hypersurfaces where open strings end (cf. section 2.1.2).

2.3 D-branes

As we have already seen in bosonic string theory there exist dynamical objects such as D-branes. These D-branes are $p+1$ dimensional objects. To have a precise notation which represents the dimensionality, we will call them Dp-branes in this section.
As we will elaborate on what follows, these objects have two faces. First of all, open strings end on these branes and hence the strings deform them. On the other hand, they are also massive and thus they will curve spacetime itself. They can be considered to be soliton-like solutions to SUGRA.

2.3.1 Low Energy effective Action

We introduced the low energy effective action both for bosonic and superstring theory above. The same can be done for the Dp-branes and again we have to demand that the worldvolume energy-momentum tensor T^{ab} vanishes. We parametrize the Dp worldvolume by coordinates ξ^a $(a = 1, \ldots, p+1)$. Finally, we can write an action for a Dp-brane as

$$S_{DBI} = -(2\pi)^{-p}\,\alpha'^{-\frac{p+1}{2}} \int d^{p+1}\xi\, e^{-\phi}\sqrt{-\det\left(\mathcal{P}[g]_{ab} + \mathcal{P}[B]_{ab} + 2\pi\alpha' F_{ab}F^{ab}\right)} \tag{2.68}$$

where $\mathcal{P}[g]$ and $\mathcal{P}[B]$ are the pull-back of the target spacetime metric and the Kalb-Ramond field to the worldvolume. The field F_{ab} is the field strength tensor of the gauge field A_a which is sourced by the string endpoint attached to the Dp-brane. Due to the form of this action, it is also called Dirac-Born-Infeld (DBI) action.

Let us consider this setup in flat spacetime, with vanishing Kalb-Ramond field $(B = 0)$ and constant dilaton $(e^{\phi} = g_s)$. In the last expression, we used the fact that the string coupling g_s is given by the expectation value of the dilaton field. We can use that $\det(1 + M) = 1 - \frac{1}{2}\mathrm{tr}M^2 + \ldots$ and expand the DBI action as

$$S_{DBI} = -(2\pi)^{2-p}\,\alpha'^{\frac{3-p}{2}}\,\frac{1}{4g_s}\int d^{p+1}\xi\, F_{ab}F^{ab}. \tag{2.69}$$

This matches exactly the term in $U(1)$ Yang-Mills (YM) theory, $-\frac{1}{4}\frac{1}{g_{YM}^2}F_{ab}F^{ab}$ and therefore we deduce that a $U(1)$ gauge field lives on the Dp-brane. The relation between the YM coupling g_{YM}^2 and the string coupling g_s can easily be read off,

$$g_{YM}^2 = g_s\,(2\pi)^{p-2}\,\alpha'^{\frac{p-3}{2}}. \tag{2.70}$$

For N coincident Dp-branes we get an additional index which labels the different branes. This is the so-called Chan-Paton factor. Due to this additional index, the gauge field living on these branes satisfies a $U(N)$ gauge symmetry.

2.3.2 Dp-branes in SUGRA

Besides considering the open string sector, we can also consider the closed sector. In this sector, we already showed that we can rewrite this sector as an effective SUGRA action in 10 dimensional target spacetime (cf. equations (2.59) and (2.62)). For Dp-branes, we can make the following ansatz for the solution of

the EoM derived from this action

$$ds^2 = H_p(r)^{-\frac{1}{2}}\eta_{\alpha\beta}dx^\alpha dx^\beta + H_p(r)^{\frac{1}{2}}\delta_{ij}dy^i dy^j, \tag{2.71a}$$

$$e^\phi = g_s H_p(r)^{\frac{3-p}{4}}, \tag{2.71b}$$

$$C_{(p+1)} = \left(H_p(r)^{-1} - 1\right) \mathrm{d}x^0 \wedge \mathrm{d}x^1 \wedge \cdots \wedge \mathrm{d}x^p, \tag{2.71c}$$

$$B_{\mu\nu} = 0 \tag{2.71d}$$

where x^α ($\alpha = 0, \ldots, p$) are coordinates on the worldvolume of the Dp-brane, and x^i ($i = p+1, \ldots, 9$) are transverse coordinates. Furthermore, we defined the distance from the brane as $r^2 = \sum_{i=p+1}^{9} y_i^2$. Plugging this ansatz in the EoM derived from the SUGRA action we obtain

$$\Box H_p(r) = 0. \tag{2.72}$$

Thus, $H_p(r)$ has to be a harmonic function which can be written as

$$H_p(r) = 1 + \left(\frac{L_p}{r}\right)^{7-p} \tag{2.73}$$

where we chose the constant to be 1 such that we obtain flat Minkowski spacetime far away from the Dp-branes ($r \to \infty$).
It can be shown that for N coincident Dp-branes the constant L_p is given by

$$L_p^{7-p} = (4\pi)^{\frac{5-p}{2}}\,\Gamma\left(\frac{7-p}{2}\right) g_s N \alpha'^{\frac{7-p}{2}}. \tag{2.74}$$

Type IIA (IIB) string theory contains only odd (even) R-R gauge potentials $C_{(p+1)}$. Since a Dp-brane couples to $C_{(p+1)}$ potential,s only even (odd) Dp-branes are stable. Therefore, the following possibilities exist

$$\text{IIA} \quad : \quad \text{D0, D2, D4, D6, D8 branes,} \tag{2.75a}$$

$$\text{IIB} \quad : \quad \text{D}-1\text{, D1, D3, D5, D7 branes.} \tag{2.75b}$$

Note that for D3-branes which we will consider in the context of $\mathrm{AdS}_5/\mathrm{CFT}_4$, the dilaton ϕ decouples and is constant, $e^\phi = g_s$. The constant $L_3^{7-3} \equiv L^4$ is then given by

$$L^4 = 4\pi g_s N \alpha'^2. \tag{2.76}$$

Let us next have a glimpse towards the holographic principle by considering the limit of $r \to 0$, i.e. we go very close to the D3-branes. With this assumption, the

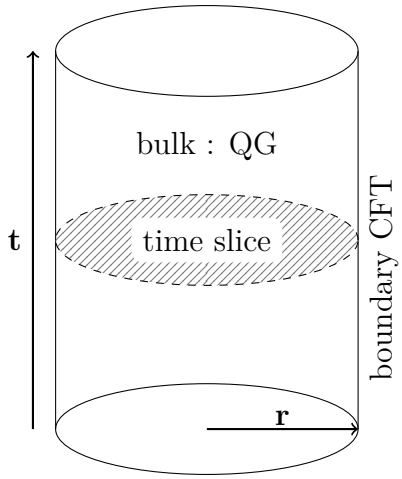

FIGURE 2.2: Visualization of the holographic principle. Within the cylinder, there lives a quantum gravity which is dual to a CFT living on the boundary.

constant term in $H_p(r)$ can be neglected and we can write down the metric as

$$\begin{aligned} ds^2 &= \frac{r^2}{L^2}\eta_{\alpha\beta}dx^\alpha dx^\beta + \frac{L^2}{r^2}dy^i dy^i \\ &= \frac{L^2}{z^2}\left(\eta_{\alpha\beta}dx^\alpha dx^\beta + dz^2\right) + L^2 d\Omega_5^2 \end{aligned} \tag{2.77}$$

where we introduced spherical coordinates instead of y^i, i.e. $ds_5^2 = dr^2 + r^2 d\Omega_5^2$, and $z = \frac{L^2}{r}$ in the last line. This is exactly the metric of $AdS_5 \times S_5$.
Hence, we have seen the two faces of D3-branes. On the one hand, there lives a $U(N)$ gauge field on them. On the other hand, the near brane geometry is $AdS_5 \times S_5$.
As we will elaborate in more detail in the next section AdS/CFT can be motivated in this manner.

2.4 Holographic Principle and AdS/CFT

Most generally speaking the holographic principle is a duality between a quantum gravity on some $AdS_{d+1} \times \mathcal{M}$ spacetime and a CFT living on its boundary. As shown in figure 2.2 this can be visualized on a cylinder. In its volume lives the quantum gravity and sources fields in the boundary CFT. From a mathematical point of view, a duality means that two theories are dynamically equivalent but can have different Lagrangians. AdS/CFT conjectured by Juan Maldacena in 1997 [6] is a specific example. AdS/CFT is also a strong-weak coupling duality which makes it interesting, because we can map problems with strong coupling to a dual problem which is weakly coupled and hence, we are able to apply PT.
In this section, we will focus on the AdS_5/CFT_4 duality which was the original

conjecture by Maldacena [6]. From these considerations, it can be generalized to other $\mathrm{AdS}_{d+1}/\mathrm{CFT}_d$ dualities.
The so-called strongest form of the duality reads [17]:

$\mathcal{N} = 4$ $SU(N)$ SYM with coupling constant g_{YM}
is dynamically equivalent to
type IIB superstring theory with string length $l_s = \sqrt{\alpha'}$ and
coupling g_s on $AdS_5 \times S_5$ with radius of curvature L and N units
of $F_{(5)}$ flux on S_5.

The parameters are related as
$g_{YM}^2 = 2\pi g_s, \quad 2g_{YM}^2 N = \frac{L^4}{\alpha'^2}.$

(2.78)

From now on we will call the first part of the duality, i.e. the SYM theory, the "CFT side" and the type IIB superstring theory side the "AdS side" for clear terminology.
The strongest form is very interesting especially conceptually, but it is very hard to compute anything due to the lack of mathematical tools. Therefore, we will consider certain limits which will make it possible to perform computations.
String theory is best understood in the PT regime where the string coupling g_s is assumed to be small, $g_s \ll 1$ while keeping $\frac{L}{\sqrt{\alpha'}}$ constant. The AdS side of the duality then reduces to classical string theory where only tree-level diagrams are considered. On the CFT side, this limit implies that $g_{YM} \ll 1$ while $g_{YM}^2 N = \lambda$ is kept finite. This means that we take the 't Hooft limit $N \to \infty$ with λ kept finite [20]. This limit is called the strong form of AdS/CFT.
Finally, we are left with only one free parameter on each side of the duality. This parameter is related as $2\lambda = \frac{L^4}{\alpha'^2}$ in the two dual theories. As already mentioned above, we want to use the strong-weak coupling property of the duality to be able to calculate strongly coupled processes in the CFT, i.e. we want to send the 't Hooft coupling to infinity, $\lambda \to \infty$. This implies that $\frac{\sqrt{\alpha'}}{L} = \frac{l_s}{L} \to 0$, and hence we arrive at the point particle approximation of string theory. The EoM are then determined by the type IIB SUGRA action (2.62) on $AdS_5 \times S_5$ spacetime.[3] This

[3]For even Dp-branes we have to use type IIA superstring theory since only there these branes are stable solutions. This is used e.g. in the Witten model where confinement can be implemented [21].

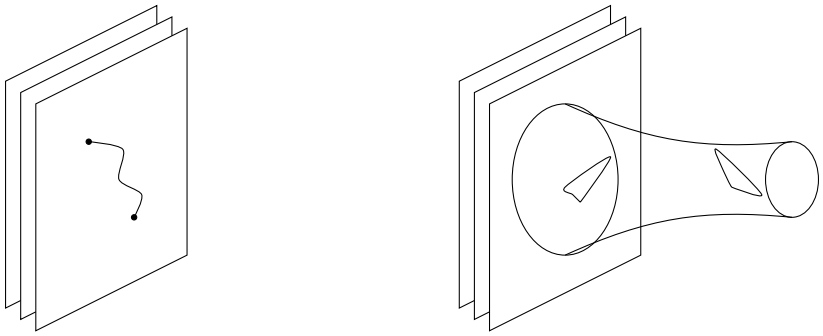

FIGURE 2.3: The two different perspectives for D-branes. The left panel shows the open string perspective where the open strings end on the brane and source a gauge field. While for the closed strings the near brane geometry is $AdS_5 \times S_5$ as indicated in the right picture.

is the weak form of the AdS/CFT duality which we will apply in chapter 3.
Let us now dig a bit deeper in the derivation and motivation for statement (2.78). As already pointed out the D-branes from the last section are the important objects. We have seen in the last sections that these D-branes are soliton-like solutions of superstring theory. As already elaborated, these D-branes have two different faces, i.e. we can have a look at the open strings and closed strings perspective. The two ideas are displayed in figure 2.3.

Open strings We have seen in section 2.3 that D-branes are hyperplanes where open strings end. The strings source a $U(1)$ gauge field A_μ transverse to the plane. This description is only valid in the regime of decoupled closed strings, i.e. $g_s \ll 1$. Furthermore, we want to ignore massive excitations and thus we consider the low energy limit $E \ll \alpha'^{-\frac{1}{2}}$.
In the case of N coincident D-branes, the gauge group becomes $U(N)$ and the effective coupling becomes $g_s N$. Therefore, this perspective is applicable if $g_s N \ll 1$. In this limit, the closed strings fully decouple due to the small string coupling and they are described by type IIB SUGRA in flat Minkowski space $\mathbb{R}^{9,1}$.

Closed strings We already know from section 2.3 that D-branes are also soliton-like solutions to SUGRA in the low energy limit $E \ll \alpha'^{-\frac{1}{2}}$. For this approximation to be valid the string length $l_s = \sqrt{\alpha'}$ has to be much smaller than the radius of curvature, i.e. $\frac{L^4}{\alpha'^2} \sim g_s N \gg 1$.
In section 2.3.2 we showed that close to the branes we have type IIB SUGRA in an $AdS_5 \times S_5$ background, while far away from the branes the action is governed again by type IIB SUGRA but this time in flat Minkowski spacetime $\mathbb{R}^{9,1}$. So once more, we have two decoupled theories.

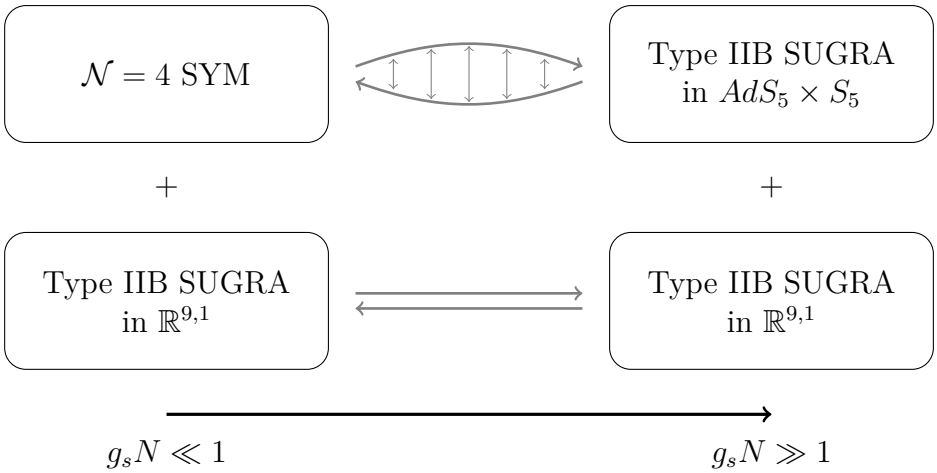

FIGURE 2.4: Summary of the closed and open string perspective for D3-branes. The type IIB SUGRA in flat Minkowski spacetime $\mathbb{R}^{9,1}$ always decouples in the low energy limit $E \ll \alpha'^{-\frac{1}{2}}$. Thus, Juan Maldacena conjectured that $\mathcal{N} = 4$ SUSY is equivalent to type IIB SUGRA in $AdS_5 \times S_5$ [6].

To summarize we have seen that in both perspectives the type IIB SUGRA in flat Minkowski spacetime $\mathbb{R}^{9,1}$ decouples from the rest of the theory which is either $\mathcal{N} = 4$ SYM or SUGRA in $AdS_5 \times S_5$, depending on the value of $g_s N$. This is also depicted in figure 2.4.
The question which is left unanswered up to now is how to map observables in the two theories. In principle, a bulk field ϕ is dual to a gauge invariant operator $\mathcal{O}$ in the boundary CFT. Here we suppress any index such that ϕ can be a scalar, vector, tensor,. etc. . The corresponding field operator maps can be derived by symmetry considerations. The statement of the strongest form of AdS/CFT (2.78) now is [22, 23]

$$\left\langle e^{i \int d^4x \, \mathcal{O}\phi_0} \right\rangle_{SYM} = Z_{\text{IIB,String}} \left(\phi \to \phi_0\right) \tag{2.79}$$

where ϕ_0 is the value of the bulk field ϕ at the conformal boundary. This means that we can obtain any expectation value for an operator by varying the type IIB string partition function $Z_{\text{IIB,String}}$ with respect to the dual field ϕ and evaluate it at the boundary. The problem here is that up to now there is no way to calculate the (quantum) string partition function since we would have to perform a path integral over all kinds of fields and also the metric which has poles at the boundary. Nevertheless, going to the weakest form resolves this problem because the path integral can be approximated by using the saddle point approximation and hence we are left with the exponential of the classical string action, i.e.

$$\left\langle e^{i \int d^4x \, \mathcal{O}\phi_0} \right\rangle_{SYM} = e^{iS_{\text{IIB,SUGRA}}\left(\overline{\phi} \to \phi_0\right)} \tag{2.80}$$

where $\overline{\phi}$ is a solution of the SUGRA EoM. With this technique, we can then calculate all required expectation values of fields, correlators, and so on. For example, the boundary energy-momentum tensor is dual to the SUGRA metric. We will use this in chapter 3 to extract physical quantities in shockwave collisions. This ends the introduction of string theory and the holographic principle. In the next section, we will introduce hydrodynamics which we will also use to analyze the results of shockwave collisions in the following chapter.

2.5 Hydrodynamics

In this section, we will review some details of relativistic hydrodynamics which describes many aspects of high-energy HICs very well. We use the first order gradient expansion in chapter 3 to judge from what time on the evolution of shockwaves is well described by hydrodynamics. We will call this time hydrodynamization time. This section is based on [17, 24].
Hydrodynamics is based on conservation laws which are related to continuous symmetries of the fundamental microscopic system as stated in the Noether Theorem. In relativistic systems, the spacetime itself exhibits translation, rotation and boost invariance. The corresponding conserved current is the energy-momentum tensor $T^{\mu\nu}$ and thus the conservation law reads

$$\partial_\mu T^{\mu\nu} = 0. \tag{2.81}$$

In this section, we further assume an additional conserved $U(1)$ current, e.g. the baryon number current, i.e.

$$\partial_\mu J^\mu = 0. \tag{2.82}$$

In a general setup with d spatial dimensions, the symmetric energy-momentum tensor has $\frac{(d+1)(d+2)}{2}$ independent components, while the current J^μ has $d+1$ independent entries. But the conservation laws only provide $d+1+1$ equations and hence there exist more unknowns than equations. In hydrodynamics one assumes that $T^{\mu\nu}$ and J^μ can be parametrized by the local temperature $T(x)$, the local fluid velocity $\vec{v}(x)$ and the local chemical potential $\mu(x)$. With this assumption, the number of unknowns equals the number of equations.
Taking any timelike vector u^μ with $u^\mu u_\mu = -1$ we can decompose $T^{\mu\nu}$ and J^μ in transverse and longitudinal components with respect to u^μ by first defining the

projection operator

$$\Delta_{\mu\nu} = g_{\mu\nu} + u_\mu u_\nu, \tag{2.83}$$

and then writing the decomposition as [25]

$$T^{\mu\nu} = \mathcal{E} u^\mu u^\nu + \mathcal{P}\Delta^{\mu\nu} + (q^\mu u^\nu + q^\nu u^\mu) + t^{\mu\nu}, \tag{2.84a}$$

$$J^\mu = \mathcal{N} u^\mu + j^\mu \tag{2.84b}$$

where $\mathcal{E}$, $\mathcal{P}$ and $\mathcal{N}$ are scalars, q^μ and j^μ are transverse vectors, i.e. $u_\mu q^\mu = u_\mu j^\mu = 0$ and $t^{\mu\nu}$ is symmetric, traceless and transverse, i.e. $u_\mu t^{\mu\nu} = 0$. Counting the degrees of freedom on both sides shows that we cover all these degrees.
The coefficients can be extracted from $T^{\mu\nu}$ and J^μ by using that $\Delta_{\mu\nu}u^\mu = 0$ and $\Delta_{\mu\nu}\Delta^{\mu\nu} = d$. We finally obtain

$$\mathcal{E} = u_\mu u_\nu T^{\mu\nu}, \quad \mathcal{P} = \frac{1}{d}\Delta_{\mu\nu}T^{\mu\nu}, \quad \mathcal{N} = -u_\mu J^\mu, \tag{2.85a}$$

$$q_\mu = -\Delta_{\mu\alpha}u_\beta T^{\alpha\beta}, \quad j_\mu = \Delta_{\mu\nu}J^\mu, \tag{2.85b}$$

$$t_{\mu\nu} = \frac{1}{2}\left(\Delta_{\mu\alpha}\Delta_{\nu\beta} + \Delta_{\nu\alpha}\Delta_{\mu\beta} - \frac{2}{d}\Delta_{\mu\nu}\Delta_{\alpha\beta}\right)T^{\alpha\beta}. \tag{2.85c}$$

The hydrodynamic approximation is that the scalars $\mathcal{E}$, $\mathcal{P}$ and $\mathcal{N}$ are functions of the scalars T, μ, $\partial_\mu u^\mu$, $u^\mu\partial_\mu T$, $\partial^2\mu$, etc.. q^μ and j^μ are functions of transverse vectors, e.g. $\Delta^{\mu\nu}\partial_\nu T$, $\Delta^{\mu\nu}\partial_\nu\mu$, etc.. The equations (2.84) in terms of the hydrodynamic variables T, μ and u_μ are called constitutive relations.
Hydrodynamics uses an expansion in derivatives, even though recent results show that it also converges to attractor solutions for large gradients [26].

2.5.1 Zeroth-order Hydrodynamics

As we have already mentioned in the last section, q^μ, j^μ and $t^{\mu\nu}$ contain derivatives and hence we immediately know that in lowest order they are zero, i.e.

$$q^\mu = j^\mu = t^{\mu\nu} = 0. \tag{2.86}$$

But $\mathcal{E}$, $\mathcal{P}$ and $\mathcal{N}$ are functions of T and μ. Going to the local rest frame of the fluid (labeled by tilde), we know the form of the energy-momentum tensor and the current, i.e.

$$\widetilde{T}^{\mu\nu} = \text{diag}\,(\epsilon, p, \ldots, p), \quad \tilde{J}^\mu = \left(n, \vec{0}\right) \tag{2.87}$$

where $\epsilon(T,\mu)$ is the equilibrium energy density, $p(T,\mu)$ the equilibrium pressure and $n(T,\mu)$ the equilibrium charge density. We can boost this to a frame moving with velocity $\vec{v}$ by applying a Lorentz boost $\Lambda(\vec{v})$. The boosted energy-momentum tensor and the boosted current then read

$$T^{\mu\nu} = \begin{pmatrix} -p+\gamma^2(\epsilon+p) & -\gamma^2(\epsilon+p)v_i \\ -\gamma^2(\epsilon+p)v_i & p\delta_{ij}+\gamma^2(\epsilon+p)v_iv_j \end{pmatrix}, \quad J^\mu = \begin{pmatrix} n \\ \gamma\vec{v} \end{pmatrix}. \tag{2.88}$$

Using the 4-velocity $u^\mu = \gamma\,(1,\vec{v})$ with $u^2=-1$ we can rewrite this as

$$T^{\mu\nu} = \epsilon u^\mu u^\nu + p\Delta^{\mu\nu}, \quad J^\mu = nu^\mu. \tag{2.89}$$

The zeroth-order hydrodynamic equations can be written down in a nice form by using the longitudinal component of the conservation equation (2.81) to give

$$\begin{aligned} u_\nu\partial_\mu T^{\mu\nu} = u_\nu\partial_\mu\left[(\epsilon+p)u^\mu u^\nu + pg^{\mu\nu}\right] = -\partial_\mu\left[(\epsilon+p)u^\mu\right] + u^\nu\partial_\nu p = 0, \\ \partial_\mu\left[(\epsilon+p)u^\mu\right] = u^\nu\partial_\nu p \end{aligned} \tag{2.90}$$

where we used that

$$u_\nu\partial_\mu u^\nu = \partial_\mu(\underbrace{u^\nu u_\nu}_{-1}) - u^\nu\partial_\mu u_\nu = -u_\nu\partial_\mu u^\nu = 0. \tag{2.91}$$

From current conservation we obtain

$$\partial_\mu(nu^\mu) = 0. \tag{2.92}$$

These are the zeroth-order hydrodynamic equations.

2.5.2 First-order Hydrodynamics

For zeroth-order hydrodynamics the expansion coefficients in (2.84) were unique since the local temperature $T(x)$, the local fluid velocity $\vec{v}(x)$ and the local chemical potential $\mu(x)$ are only well defined in equilibrium. In the first-order approximation, these quantities can't be defined uniquely any more, i.e. they are only defined up to gradients which vanish in the equilibrium. Thus we can write them as

$$\mathcal{E} = \epsilon(T,\mu) + f_{\mathcal{E}}\left(\partial T, \partial\mu, \partial u\right), \tag{2.93a}$$

$$\mathcal{P} = p(T,\mu) + f_{\mathcal{P}}\left(\partial T, \partial\mu, \partial u\right), \tag{2.93b}$$

$$\mathcal{N} = n(T,\mu) + f_{\mathcal{N}}\left(\partial T, \partial\mu, \partial u\right). \tag{2.93c}$$

The coefficients $\epsilon(T,\mu)$, $p(T,\mu)$ and $n(T,\mu)$ are determined by the equation of state in thermal equilibrium, while the form of the out-of-equilibrium functions $f_{\mathcal{E}/\mathcal{P}/\mathcal{N}}$ depends on the choice of the hydrodynamic variables. This choice is often referred to as the choice of a frame, hence, we will adopt this nomenclature in what follows. It is important to stress here that the hydrodynamic parameters do not have a first-principle microscopic meaning. One has to understand them as auxiliary parameters which are used to parameterize the microscopically well-defined energy-momentum tensor and current. Therefore, we can change these parameters at will as long as $T^{\mu\nu}(x)$ and $J^{\mu}(x)$ remain unchanged. We can write an arbitrary frame transformation as

$$T(x) \rightarrow T'(x) = T(x) + \delta T(x), \tag{2.94a}$$
$$\mu(x) \rightarrow \mu'(x) = \mu(x) + \delta\mu(x), \tag{2.94b}$$
$$u^{\mu}(x) \rightarrow u'^{\mu}(x) = u^{\mu}(x) + \delta u^{\mu}(x) \tag{2.94c}$$

with δT, $\delta\mu$ and δu^{μ} being first-order in derivatives. From the normalization condition $u^2 = -1$ we can conclude that $u_{\mu}\delta u^{\mu} = 0$, i.e. δu^{μ} is transverse. Using (2.85), the fact that $T^{\mu\nu}$ and J^{μ} remain constant and that q^{μ}, j^{μ} and $t^{\mu\nu}$ are transverse, we can calculate the effect on the parameters of (2.84) of such a transformation to first order. They are given by

$$\delta\mathcal{E} = 0, \quad \delta\mathcal{P} = 0, \quad \delta\mathcal{N} = 0, \tag{2.95a}$$
$$\delta q_{\mu} = -\left(\mathcal{E} + \mathcal{P}\right)\delta u_{\mu}, \quad \delta j_{\mu} = -\mathcal{N}\delta u_{\mu}, \tag{2.95b}$$
$$\delta t_{\mu\nu} = 0. \tag{2.95c}$$

As already mentioned above we can fix $d+3$ components freely, since T, μ and $u^{\mu}(x)$ are not uniquely defined out-of-equilibrium.

One of the most common choices for δu_{μ} is such that $\delta j^{\mu} = 0$ which is called the Eckart frame [25]. This choice implies that there is no charge flow in the local rest frame of the fluid.

Another possible choice is the so-called Landau frame [27] where δu_{μ} is chosen such that $q_{\mu} = 0$, i.e. there is no energy flow in the fluid rest frame. This is also the frame which we will use from now on.

Since $\mathcal{E}$, $\mathcal{P}$ and $\mathcal{N}$ are invariant under the transformations (2.94) it follows that, e.g., $\epsilon(T,\mu) + f_{\mathcal{E}}(\partial T, \partial\mu, \partial u) = \epsilon(T',\mu') + f'_{\mathcal{E}}(\partial T', \partial\mu', \partial u')$. Hence the functions

$f_{\mathcal{E}/\mathcal{P}/\mathcal{N}}$ have to satisfy

$$f'_{\mathcal{E}} = f_{\mathcal{E}} - \left(\frac{\partial \epsilon}{\partial T}\right)_{\mu} \delta T - \left(\frac{\partial \epsilon}{\partial \mu}\right)_{T} \delta\mu, \tag{2.96a}$$

$$f'_{\mathcal{P}} = f_{\mathcal{P}} - \left(\frac{\partial p}{\partial T}\right)_{\mu} \delta T - \left(\frac{\partial p}{\partial \mu}\right)_{T} \delta\mu, \tag{2.96b}$$

$$f'_{\mathcal{N}} = f_{\mathcal{N}} - \left(\frac{\partial n}{\partial T}\right)_{\mu} \delta T - \left(\frac{\partial n}{\partial \mu}\right)_{T} \delta\mu. \tag{2.96c}$$

Additionally to the already chosen δu_μ, we can freely choose δT and $\delta\mu$ and hence we can set two of the three primed functions to zero. Usually one sets $f'_{\mathcal{E}}$ and $f'_{\mathcal{N}}$ to zero, which means that the out-of-equilibrium temperature and chemical potential are chosen such that $\mathcal{E} = \epsilon$ and $\mathcal{N} = n$.
After this choice we have fixed all freedoms, i.e. in the Landau frame we chose $\mathcal{E} = \epsilon$, $\mathcal{N} = n$ and $q^\mu = 0$. Thus, we have to express $\mathcal{P}$, j^μ and $t^{\mu\nu}$ in hydrodynamical variables. In first-order in a gradient expansion, there exist three scalars

$$u^\lambda \partial_\lambda T, \quad u^\lambda \partial_\lambda \mu, \quad \partial_\lambda u^\lambda, \tag{2.97}$$

three transverse vectors

$$\Delta^{\mu\nu}\partial_\nu T, \quad \Delta^{\mu\nu}\partial_\nu \mu, \quad \Delta^{\mu\nu} u^\lambda \partial_\lambda u_\nu T, \tag{2.98}$$

and one transverse, symmetric, and traceless tensor

$$\sigma^{\mu\nu} = \Delta^{\mu\alpha}\Delta^{\nu\beta}\left(\partial_\alpha u_\beta + \partial_\beta u_\alpha - \frac{2}{d} g_{\alpha\beta}\partial_\lambda u^\lambda\right). \tag{2.99}$$

Having a look at the scalar $\mathcal{P}$ first we make the ansatz

$$\mathcal{P} = p + c_1 u^\lambda \partial_\lambda T + c_2 u^\lambda \partial_\lambda \mu + c_3 \partial_\lambda u^\lambda + \mathcal{O}\left(\partial^2\right) \tag{2.100}$$

with coefficients c_i, $i \in \{1, 2, 3\}$. We can use the zeroth-order hydrodynamic equations $u_\mu \partial_\nu T^{\mu\nu} = 0$ and $\partial_\mu J^\mu = 0$ (2.90) to eliminate two of the three coefficients. Hence, we choose $c_1 = c_2 = 0$ to obtain

$$\mathcal{P} = p - \zeta \partial_\lambda u^\lambda + \mathcal{O}\left(\partial^2\right) \tag{2.101}$$

with ζ being the bulk viscosity which has to be determined from the microscopic theory.
Continuing with j^μ we can write it with three constants and again make use of

the zeroth-order hydrodynamic equation $\Delta_{\lambda\nu}\partial_\mu T^{\mu\nu} = 0$ to arrive at

$$j^\mu = -\sigma T \Delta^{\mu\nu}\partial_\nu\left(\frac{\mu}{T}\right) + \chi_T \Delta^{\mu\nu}\partial_\nu T + \mathcal{O}\left(\partial^2\right) \tag{2.102}$$

where σ is the charge conductivity and χ_T has to be zero by requiring that entropy production is positive [24].
For the tensor part there exist no zeroth-order hydrodynamic equations and, thus, this part is written as

$$t^{\mu\nu} = -\frac{\eta}{2}\sigma^{\mu\nu} + \mathcal{O}\left(\partial^2\right). \tag{2.103}$$

In this equation η is the shear viscosity. Note that we have an additional factor of $\frac{1}{2}$ here to be consistent with work in numerical AdS/CFT [1, 28–30].
With this parametrization, we can write down the energy-momentum tensor and the current as

$$\begin{aligned} T^{\mu\nu} &= \epsilon u^\mu u^\nu + p\Delta^{\mu\nu} - \frac{\eta}{2}\Delta^{\mu\alpha}\Delta^{\nu\beta}\left(\partial_\alpha u_\beta + \partial_\beta u_\alpha - \frac{2}{d}g_{\alpha\beta}\partial_\lambda u^\lambda\right) \\ &\quad - \zeta\Delta^{\mu\nu}\partial_\lambda u^\lambda + \mathcal{O}\left(\partial^2\right), \end{aligned} \tag{2.104a}$$

$$J^\mu = nu^\mu - \sigma T\Delta^{\mu\nu}\partial_\nu\left(\frac{\mu}{T}\right) + \chi_T\Delta^{\mu\nu}\partial_\nu T + \mathcal{O}\left(\partial^2\right). \tag{2.104b}$$

These are the first-order hydrodynamic equations for an arbitrary fluid.
Since we will deal with a CFT in chapter 3, the considered fluid will also be conformal. One property of a conformal theory is the tracelessness of the energy-momentum tensor, i.e. $T^\mu{}_\mu = 0$. Since $u^2 = -1$, $\Delta^\mu{}_\mu = d$ and $\epsilon = \frac{p}{d}$, we can see that $\zeta \overset{!}{=} 0$. It is straightforward to show that one can write the energy-momentum tensor also in the notation of [1, 28–30]

$$\begin{aligned} T^{\mu\nu} =& pg^{\mu\nu} + (\epsilon{+}p)u^\mu u^\nu - \eta\left[\partial^{(\mu}u^{\nu)} + u^{(\mu}u^\rho\partial_\rho u^{\nu)} - \frac{1}{3}\partial_\lambda u^\lambda(g^{\mu\nu} + u^\mu u^\nu)\right] \\ &+ \mathcal{O}(\partial^2). \end{aligned} \tag{2.105}$$

Furthermore, in a thermal CFT, there is only one scale. Thus, we can express all of the coefficients in terms of the proper energy ϵ, i.e. [31, 32]

$$T = \left(\frac{8\epsilon}{3\pi^2 N_c^2}\right)^{\frac{1}{4}}, \quad \eta = \frac{1}{3\pi T}\epsilon = \frac{\epsilon^{3/4}}{3^{3/4}\sqrt[4]{8}}\sqrt{\frac{N_c}{\pi}}, \quad p = \frac{\epsilon}{3}. \tag{2.106}$$

Hence, the first-order hydrodynamics in a conformal theory is determined by the proper energy and the fluid 4-velocity which can be written as the normalized ($u_\mu u^\mu = -1$), future directed ($u^0 > 0$) eigenvector and the eigenvalues of the full

energy-momentum tensor

$$T^{\mu}_{\ \nu} u^{\nu} = -\epsilon u^{\mu}. \tag{2.107}$$

This closes the discussion of hydrodynamics and also this introductory section. We will continue by applying the gauge/gravity duality to the collision of lumps of energies in a strongly coupled CFT in the next chapter.

3

Shockwave Collisions in AdS/CFT

In this chapter, we will use the holographic principle to get insight into HICs mainly concerning the formation of the QGP. In HICs nuclei are accelerated and collide with very high energies as it is done, e.g., at LHC (Large Hadron Collider) or RHIC (Relativistic Heavy Ion Collider). This process can be thought of as consisting of several stages indicated in figure 3.1. The whole process is described by QCD but we cannot access solutions for all of these stages because of the lack of mathematical techniques. In particular, non-perturbative, highly dynamical processes far from thermal equilibrium cannot be treated reliably with present-day QCD techniques.

Hence, we will use the holographic principle to model such situations. To do this we follow the ideas of [28, 29, 33, 34] and collide two gravitational shockwaves in 5-dimensional AdS space which is related via the holographic dictionary to two lumps of energy moving towards each other with the speed of light in the dual field theory. Hence, we have to solve Einstein's equations in AdS space numerically. We will do this by using the characteristic, also called Bondi-Sachs formulation [35, 36] pioneered for asymptotically AdS spaces by Chesler and Yaffe in [28, 33, 37]. In these publications, the coupled non-linear Einstein's equations are converted into a set of nested ODEs by applying a null-slicing of the geometry. This will be reviewed in section 3.2.

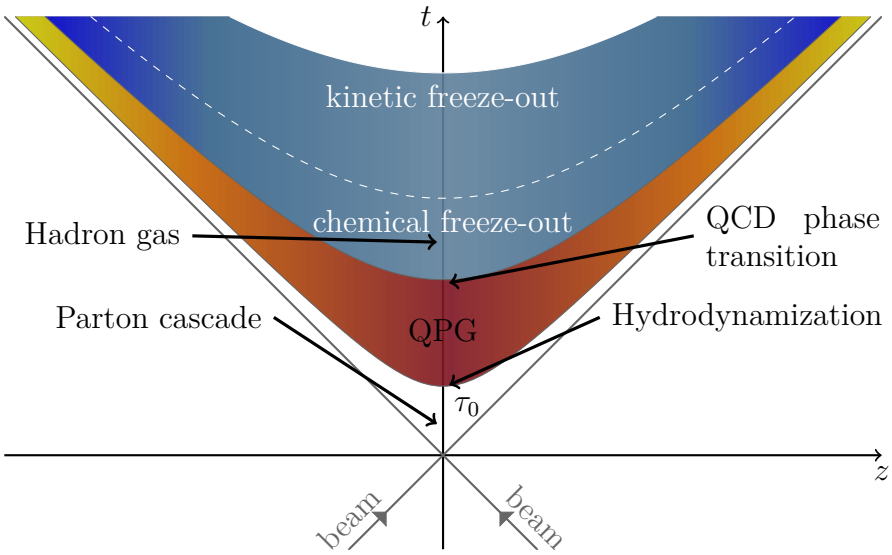

FIGURE 3.1: This picture visualizes the different stages of HICs. The two beams (or nuclei) meet each other at $t = 0$. After hydrodynamization τ_0 a deconfined QGP is formed. This plasma expands and cools down until it undergoes the QCD phase transition to the confined phase at temperature $T = T_c$ and a hadron gas forms. After the freeze-out hadrons form and they reach the detectors. This figure is adapted from [38].

Before describing this we will give a quite extensive introduction to numerical methods to solve differential equations, focusing on pseudo-spectral methods which we will use to solve the set of nested differential equations.[1]
Afterwards, we will move on to solve the differential equations for the collision of shockwaves. To reduce the dimensionality of the (5 dimensional) problem, which was already solved in [29] where they also included the transverse directions, we will use planar shocks as an approximation instead of keeping the transverse dependence. But in contrast to [29] we can go to thinner (and thus more realistic) shock widths in the longitudinal directions. This approximation was also used in [28, 34] for the planar case.
In [1] we considered asymmetric planar shocks as an approximation for off-center collisions (cf. figure 3.8). This argument will be motivated in section 3.3. In section 3.5 we will then show results of the simulations and analyze some aspects which are of interest for particle physics and hydrodynamization of the QGP.

[1]This section is accompanied by a MATHEMATICA notebook which you can request from the author via mail `andreas.rabenstein@ur.de`.

3.1 Numerical Methods

We start this section by giving a brief overview of numerical methods for linear differential equations and the corresponding main ideas. Afterwards, we will discuss interpolation and Gaussian quadrature as an approximation for needed integrals. In section 3.1.4 spectral methods will be introduced. Finally, we will solve several types of differential equations. We apply various techniques including domain decomposition and the Newton-Raphson method for non-linear differential equations.

3.1.1 Weighted Residual Methods

For a lot of problems we are interested in, the aim is to solve a linear differential equation of the type

$$Lu = f \tag{3.1}$$

where L is a linear differential operator. Most numerical methods used nowadays are weighted residual methods where one approximates the solution u within a vectorspace with some basis ϕ_i

$$u \approx u_N = \sum_{i=0}^{N} u_i \phi_i \tag{3.2}$$

and then defines the residual to be

$$R = Lu_N - f. \tag{3.3}$$

Obviously, this residual has to be minimized. To do so one requires that the (weighted) scalar product with a test function ξ_i vanishes, i.e.

$$(R, \xi_i)_\omega = 0. \tag{3.4}$$

The different methods are then characterized by the choice of the test function and we list the most common examples in what follows:

Subdomain method

$$\xi_i = \begin{cases} 1 & x \in D_i \\ 0 & \text{else} \end{cases} \tag{3.5}$$

where D_i is a subdomain.

Collocation method

$$\xi_i = \delta(x - x_i). \tag{3.6}$$

Least Squares method

$$\xi_i = \frac{\partial R}{\partial \alpha_i}. \tag{3.7}$$

Galerkin method

$$\xi_i = \phi_i. \tag{3.8}$$

The pseudospectral method is a Galerkin method as we will see later on. In the next section, we will discuss interpolation which is essential for numerical methods in more detail.

3.1.2 Interpolation

As we have seen in the last section we have to interpolate the (unknown) exact solution (c.f., equation (3.2)). For the interpolating polynomial

$$p_N(x) = a_N x^N + a_{N-1} x^{N-1} + \cdots + a_1 x^1 + a_0 \tag{3.9}$$

we require that it coincides with the function $u(x)$ at the grid-points which we have to specify. The error for such a polynomial interpolation is given by [39]

$$\max_{x_0 \le x \le x_1} |f(x) - p_N(x)| \le \frac{1}{(N+1)!} \max_{x_0 \le x \le x_1} \left| \prod_{k=0}^{N} (x - x_k) \right| \max_{x_0 \le x \le x_1} \left| f^{(N+1)} \right|. \tag{3.10}$$

A theorem by Weierstrass states that there is always a polynomial arbitrarily close to any continuous function [40]. Of course for an arbitrarily "good fit" N has to be sufficiently large. But for computational reasons, we want to keep N rather small. Thus there are two possibilities to reduce the error on the interpolation:

1. Pick the grid-points such that they minimize the term $\prod (x - x_k)$. It can be shown that this is fulfilled by the zeros of the Chebyshev polynomials [39].

2. Use a local and piecewise fit. This is the case for the domain decomposition we introduce later-on and also, e.g., for the widely used Finite Element Methods (FEMs).

Note that due to practical reasons we will not use the zeros of the Chebyshev polynomials as grid, but we will use the "extrema- and endpoints" or Gauss-Lobatto-

grid as it is then easier to implement boundary (and matching) conditions.
If we now consider an arbitrary basis of orthogonal polynomials ϕ we can write the polynomial interpolation $P_N u$ as a projection of u on the orthogonal polynomials ϕ [41]

$$P_N u = \sum_{n=0}^{N} \hat{u}_n \phi_n \quad \text{with} \quad \hat{u}_n = \frac{(u, \phi_n)_\omega}{(\phi_n, \phi_n)_\omega}. \tag{3.11}$$

Note that due to the fact that we mentioned orthogonality a scalar product with weight function ω has to exist. To obtain the coefficients of the functions, integrals of the form

$$(u, \phi_n)_\omega = \int_{-1}^{1} dx u(x) \phi_n(x) \omega(x) \tag{3.12}$$

have to be performed. As their calculation is very expensive in general, we need to approximate these integrals. We do this by using Gaussian quadrature and generalizations thereof, which we will introduce in the next section.

3.1.3 Gauss Quadrature

Due to finite computational resources, we approximate the needed integrals for interpolation. The Gaussian quadrature theorem basically states that, given a weight $\omega(x)$, there exist $N+1$ positive real numbers ω_i and $N+1$ real numbers $x_i \in [-1, 1]$ such that [41]

$$\forall u \in \mathbb{P}_{2N+\delta} \; : \quad \int_{-1}^{1} u(x) \omega(x) dx = \sum_{n=0}^{N} u(x_n) \omega_n \tag{3.13}$$

where $\mathbb{P}_{2N+\delta}$ are polynomials of order $2N + \delta$ and different δ refer to different quadratures:

- Gauss quadrature: $\delta = 1$
- Gauss-Radau quadrature: $\delta = 0$ and $x_0 = -1$
- Gauss-Lobatto quadrature: $\delta = -1$ and $x_0 = -1$, $x_n = 1$

Obviously, one loses accuracy if one specifies some of the grid-points. We will use Gauss-Lobatto quadrature to be able to implement boundary (and matching) conditions in a straight-forward manner. The weights and the grid-points are calculated by requiring that the integrals of the basis functions are exact (one

could also use any other orthogonal basis to do so), i.e.

$$\forall n \in \{0, 1, \ldots, 2N + \delta\} \ : \qquad \int_{-1}^{1} \phi_n(x)\omega(x)dx \stackrel{!}{=} \sum_{i=0}^{N} \phi_i(x)\omega_i(x). \tag{3.14}$$

To be precise with nomenclature we have to specify the polynomials we use as well as the grid-points. For the spectral methods we introduce later we will use the Chebyshev-Gauss-Lobatto quadrature where the points of the grid are given by

$$x_i = \cos\left(\frac{i\pi}{N}\right) \quad i = 0, \ldots, N \quad \text{and} \quad \omega_i = \frac{\pi}{c_i N} \tag{3.15}$$

where $c_i = 2$ for $i = 0, N$ and $c_i = 1$ elsewhere.
How to interpolate the solution was discussed in the last two sections.

3.1.4 Spectral Methods

As mentioned in the previous section the spectral method is a Galerkin method, i.e. the test functions ξ are equal to the basis functions ϕ. Depending on the symmetries of the problem these functions have to be chosen suitably. Boyd states in [42] that one should mostly use Chebyshev polynomials unless the solution is periodic where one should use Fourier series. Furthermore, it is advantageous to modify the basis functions such that they satisfy

$$\phi_i(x_j) = \delta_{ij}. \tag{3.16}$$

These functions are referred to as Cardinal functions. As mentioned in the last section we will use Gauss-Lobatto grid-points (3.15). Because the Cardinal functions satisfy (3.16) they are also often called Lagrange polynomials as they are of the form $\prod {}^{(x-x_i)}/_{(x_j-x_i)}$. For the Chebyshev polynomials

$$T_k(x) = \cos(k \arccos(x)) \tag{3.17}$$

and Gauss-Lobatto grid-points (3.15) the Cardinal functions $C_j(x)$ are given by [43]

$$C_j(x) = (-1)^{j+1} \frac{(1 - x^2)}{c_j N^2 (x - x_j)} \frac{dT_N(x)}{dx}. \tag{3.18}$$

The limit $x \to x_j$ can be taken easily by using L'Hôspital's theorem. Let us now consider the example of a (linear) M-th order differential equation with different coefficient functions $p_p(x)$, i.e. the differential operator is given by $L = \sum_{p=0}^{M} p_p(x) \frac{d^p}{dx^p}$. Then equation (3.4) with the approximated solution can be

written as

$$\sum_{p=0}^{M}\sum_{n=0}^{N}\int_{-1}^{1}dx\underbrace{\left(p_p(x)\frac{d^p}{dx^p}u_nC_n(x)-f(x)\right)}_{R=Lu_N-f}\underbrace{C_m(x)}_{\xi_m}\omega(x)=0 \tag{3.19}$$

where we used $C_m(x)$ as a test function. This integral can be approximated by using Chebyshev-Gauss-Lobatto quadrature to yield

$$\sum_{p=0}^{M}\sum_{n=0}^{N}\sum_{l=0}^{N}u_np_p(x_l)\frac{d^pC_n}{dx^p}\Big|_{x=x_l}\delta_{ml}=\sum_{l=0}^{N}f(x_l)\delta_{ml}. \tag{3.20}$$

The Kronecker-δ's occur due to (3.16). Evaluating them gives

$$\sum_{p=0}^{M}\sum_{n=0}^{N}u_np_p(x_m)\frac{d^pC_n}{dx^p}\Big|_{x=x_m}=f(x_m). \tag{3.21}$$

The Cardinal functions can be written down in analytical form and thus the derivatives occurring in the above formula can be calculated straightforwardly and then be evaluated at the grid-points with arbitrary precision. Expressions can be found, e.g. in appendix F of [42].
Thus, we have transformed the differential equation to the matrix equation (3.21) which we can solve using standard routines.
Hence, we have presented the basic principle of the spectral method. In what follows we will explain some technical details.

3.1.5 Applications

In this section, we will apply the spectral methods to several model differential equations. We will furthermore explain the different techniques which are applied.

3.1.5.1 Ordinary Differential Equation

To begin with, we consider an ODE

$$u''(x)-x^6u(x)=x \tag{3.22}$$

with boundary conditions $u(0)=a$, $u(1)=b$. In the provided Mathematica notebook we use $a=b=1$, but this can be changed arbitrarily. To compare the result we use the inbuilt DSolve or NDSolve functions to solve the equation. In this and the following subsections, we will first solve the equation without and then with domain decomposition.

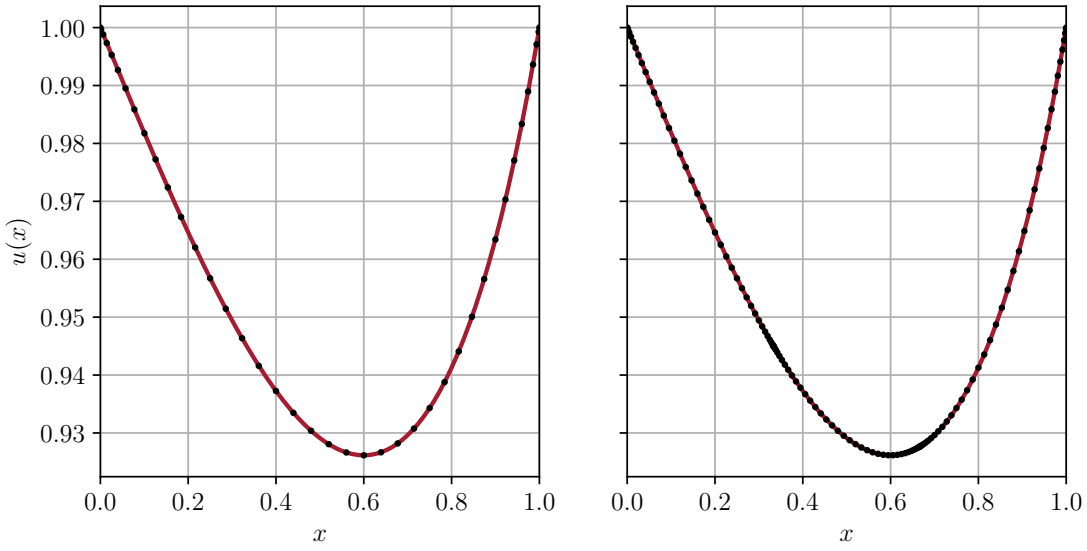

FIGURE 3.2: Comparison between the MATHEMATICA solution (red) and the solution obtained by application of spectral methods (black). The left plot shows the results for (3.22) without domain decomposition while the right graph shows the one with domain decomposition.

SINGLE DOMAIN

For the single domain example, the implementation is straightforward. We write equation (3.21) as a matrix equation, implement the boundary conditions by replacing the first and the last row by the corresponding requirements and then solve the resulting system of equations. The comparison between the obtained solution and the MATHEMATICA solution is shown in the left panel of figure 3.2.

DOMAIN DECOMPOSITION

For more sophisticated problems where the solution varies very rapidly, we need to put more effort into solving the differential equation. As can be found in literature the error decreases exponentially with the number of grid-points N for spectral methods [42]. One important fact for this proof is the global definition of the basis functions. Higher accuracy can be obtained by increasing the number of basis functions N. With finite computational resources only finite computational accuracy is reached. Let us consider the differentiation matrix from appendix F of [42]. For larger N the elements of the matrix, we want to invert, span a larger range of numbers. There is an element on the diagonal of the differentiation matrix $-\frac{x_i}{2(1-x_i)^2}$ which is very small for $x_i \approx 0$ (this is always the case as the grid-points are chosen in $[-1, 1]$). On the other hand, the first entry of the matrix is $(1+2N^2)/6$ and thus increases quadratically with N. Computational errors from the matrix inversion become more and more significant with increasing N. Thus we need to think about other methods to improve the accuracy without increasing N. This

is why we apply domain decomposition where we split the computational domain into M subdomains. In principle, it is possible to have subdomains of different size which is, e.g., used in adaptive FEM, but we only consider equal subdomains in this work.

In the case of an ODE we can apply the method of homogeneous solutions (nomenclature from [41], see also chapter 22 of [42]). In this method, one uses the fact that we can add arbitrary solutions of the homogeneous problem to the solution of the inhomogeneous one and it still solves the ODE. If we consider the equation $Lu = f$ again we solve the following three problems in each subdomain

$$Lu_l = 0 \quad u_l(x_l) = 1 \;\&\; u_l(x_r) = 0, \tag{3.23a}$$

$$Lu_r = 0 \quad u_r(x_l) = 0 \;\&\; u_r(x_r) = 1, \tag{3.23b}$$

$$Lu_p = f \quad u_p(x_l) = 0 \;\&\; u_p(x_r) = 0 \tag{3.23c}$$

where x_l and x_r denote the left and the right edge respectively. Then

$$u(x) = u_p(x) + A_l u_l(x) + A_r u_r(x) \tag{3.24}$$

also solves the ODE. Thus it is left over to determine the coefficients A_l and A_r such that the solution is C^1 ($2\,M - 2$ conditions) and satisfies the boundary conditions (2 conditions). This argumentation only holds for a second order differential equation as we have $2M$ degrees of freedom representing the boundary conditions in each subdomain. For an arbitrary order differential equation the number of equations we solve in the subdomains varies (c.f., section 3.1.5.5). Hence all coefficients are set by these requirements. To satisfy Dirichlet boundary conditions it is obvious that

$$A_l^{(0)} = a \quad \text{and} \quad A_r^{(M-1)} = b. \tag{3.25}$$

while continuity requires that

$$A_r^{(j)} = A_l^{(j+1)} \quad j = 0, \ldots, M-2. \tag{3.26}$$

For a continuous derivative we have to require that

$$\begin{aligned} A_l^{(j)} u_l^{(j)\,\prime}(x) + A_l^{(j+1)} \left[u_r^{(j)\,\prime}(x) - u_l^{(j+1)\,\prime}(x) \right] - A_l^{(j+2)} u_r^{(j+1)\,\prime}(x) \\ = u_p^{(j+1)\,\prime}(x) - u_p^{(j)\,\prime}(x) \end{aligned} \tag{3.27}$$

for $j = 0, \ldots, M-2$. From these constraints, we can derive a system of linear equations which is represented by a band diagonal matrix. Solving this yields the

coefficients for the wanted solution.
This method is implemented in the MATHEMATICA notebook. The obtained solution is shown in the right panel of figure 3.2.

3.1.5.2 Coupled linear Differential Equations

Let us now turn to coupled linear equations. In this section, we consider the following system of coupled equations

$$\begin{aligned} y_1' - 4y_1 - 7y_2 &= 0, \\ y_2' + 2y_1 + 5y_2 &= 0 \end{aligned} \tag{3.28}$$

with boundary conditions

$$y_1(0) = 1 \quad \text{and} \quad y_1(1) = 2. \tag{3.29}$$

For coupled linear differential equations we write the two equations in the form

$$L \begin{pmatrix} y_1 \\ y_2 \end{pmatrix} = \begin{pmatrix} L_{11} & L_{12} \\ L_{21} & L_{22} \end{pmatrix} \begin{pmatrix} y_1 \\ y_2 \end{pmatrix} = \begin{pmatrix} f_1 \\ f_2 \end{pmatrix} \tag{3.30}$$

and both solutions (y_1, y_2) are expanded in basis functions to obtain a larger $[2(N+1)] \times [2(N+1)]$ matrix system which we can solve. In the example above the differential operators are given by

$$L_{11} = \frac{d}{dx} - 4, \qquad L_{12} = -7, \tag{3.31}$$

$$L_{21} = 2, \qquad L_{22} = \frac{d}{dx} + 5. \tag{3.32}$$

Each submatrix L_{ij} is calculated as in the last section and afterwards the matrix L is formed. This procedure is also implemented in the MATHEMATICA notebook and the results are visualized in the left plot of figure 3.3.

Domain Decomposition

For the domain decomposition, we construct the matrix from the corresponding submatrices and then determine the coefficients as in the last section, i.e. we use the method of homogeneous solutions again. Note that for this specific example we only had to implement two boundary conditions as we have two first order equations. The results are shown in the left panel of figure 3.3.

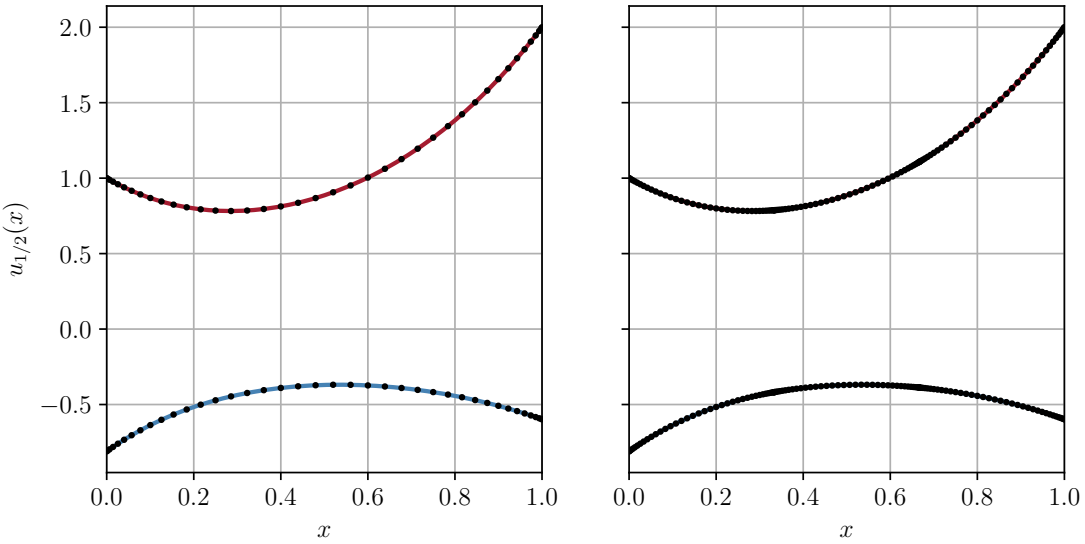

FIGURE 3.3: Comparison for the coupled linear equations (3.28). The solution y_1 is visualized in red while the solution y_2 is visualized in blue. The left plot again shows the results for a single domain while the right plot shows the outcome for domain decomposition.

3.1.5.3 NON-LINEAR EQUATION

In this section, we will deal with non-linear equations. We will present two different methods each with and without domain decomposition. Both methods are based on the Newton-Raphson method which is a well-known tool to find the roots of a function. We denote a non-linear equation by

$$\mathcal{N}(u) = f. \tag{3.33}$$

Throughout the current section, we will use the following equation as example

$$u'' - u^2 = 1 \tag{3.34}$$

with boundary conditions $u(0) = u(1) = 1$.

NEWTON-RAPHSON SINGLE DOMAIN METHOD

As mentioned before the Newton-Raphson method is a tool to find the roots of a function. Thus we rewrite the equation as $\mathcal{N}(u) - f = 0$. To find the zeros of a function $\vec{g}(x_1, \ldots, x_N)$ with the Newton-Raphson method, we start with an initial guess $\vec{x}$ which we assume to be close to a zero $\vec{x} + \vec{\delta}$, $\vec{\delta} \ll 1$. As we assume to be close to the zero we can perform a Taylor series in each component g_i to obtain

$$g_i(\vec{x} + \vec{\delta}) = g_i(\vec{x}) + \sum_j J_{ij}\delta_j + \mathcal{O}\left(|\vec{\delta}|^2\right) \tag{3.35}$$

with the Jacobian

$$J_{ij} = \frac{\partial g_i}{\partial x_j}\Big|_{\vec{x}}. \tag{3.36}$$

Neglecting $\mathcal{O}(|\vec{\delta}|^2)$ contributions we can solve for $\vec{\delta}$ to obtain

$$\vec{\delta} = -J^{-1}\vec{g}(\vec{x}). \tag{3.37}$$

Then the new guess for the zero is given by

$$\vec{x}_{new} = \vec{x}_{old} + \vec{\delta} = \vec{x}_{old} - J^{-1}\vec{g}(\vec{x}_{old}). \tag{3.38}$$

This is performed iteratively until some specified criterion is reached. One natural choice for this is to calculate $\vec{g}(\vec{x}_{new})$ (which has to be done anyway for the next step) and require that a specified norm is below a certain value. We chose the maximum norm in the accompanying MATHEMATICA notebook.
To apply the Newton-Raphson method to solve non-linear differential equations we start with choosing a trial function $\vec{t}$ which satisfies the boundary condition and is close enough to a zero for convergence. For the example considered here we chose $t(\vec{x}_i) \equiv t_i = 1\ \forall i$. Next, we define $\vec{\theta}$ as the spectral representation of the differential equation. For the example we consider here, this is given by

$$\theta_i = \sum_j D_{ij}^2 t_j - t_i^2 - 1 \tag{3.39}$$

where D_{ij} is the differentiation matrix. The Jacobian J for this reads

$$J_{ij} = D_{ij}^2 - 2\delta_{ij} t_i. \tag{3.40}$$

Afterwards, we can construct the next trial function according to equation (3.38). In doing so we use $\theta(0) = \theta(1) = 0$ as boundary conditions. Then we calculate θ for the new trial function and afterwards we check if the maximum norm

$$\theta_{\max} = \max |\theta_i| \tag{3.41}$$

is below a specified value. The results are shown in the left panel of figure 3.4.

NEWTON-RAPHSON WITH DOMAIN DECOMPOSITION

Let us now use domain decomposition again. It is obvious that we cannot apply the method of homogeneous solutions as the sum of it does not necessarily give a solution to the non-linear problem any more. We have to solve the problem in

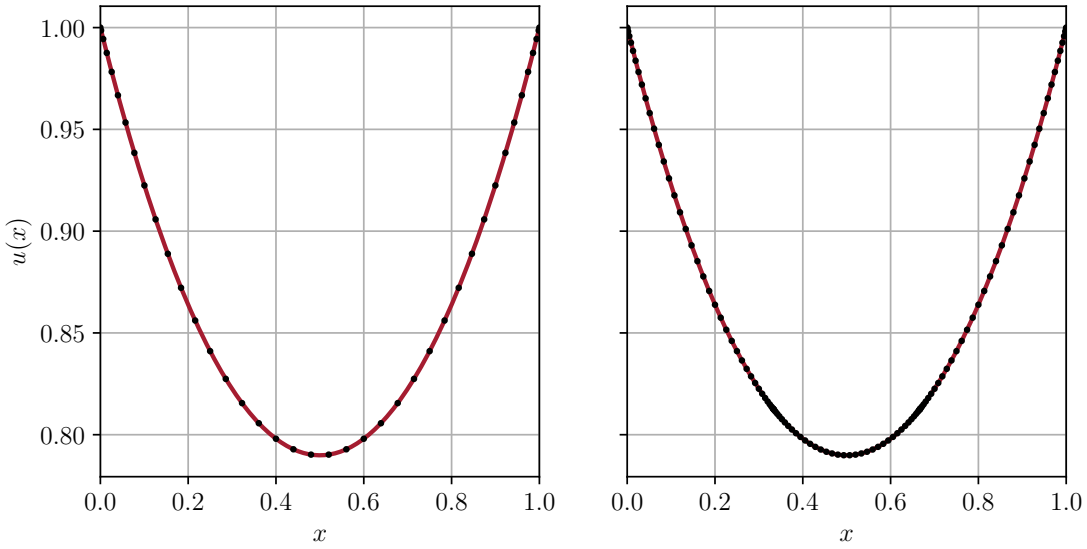

FIGURE 3.4: Comparison of the results of (3.34) with the inbuilt NDSOLVE function (red) and the solution obtained with the spectral method (black). The left plot shows the results with a single domain while the right plot depicts the outcome with multiple domains.

total and not only in each subdomain separately. Therefore we start by denoting the non-linear operator in each subdomain by $\mathcal{N}^{(i)}$ for $i = 0, \ldots, M-1$ (where M is the number of subdomains). The matrix representation of the differential equation is then block-diagonal and given by

$$\mathcal{N} = \begin{pmatrix} \mathcal{N}^{(0)} & 0 & \ldots & 0 \\ 0 & \mathcal{N}^{(1)} & \ldots & 0 \\ \vdots & \vdots & \ddots & \vdots \\ 0 & 0 & \ldots & \mathcal{N}^{(M-1)} \end{pmatrix}. \tag{3.42}$$

To ensure a certain continuity we need to add additional constraints. This is done as for the boundary conditions, i.e. we replace certain rows by conditions. The first and the last row of $\mathcal{N}$ are replaced by boundary conditions. The requirement for continuity, i.e. the requirement that the coefficients at the boundary of the domains coincide results effectively in an overlapping of the different matrices as depicted in figure 3.5. This can be seen straightforwardly by writing down the corresponding lines explicitly.
For the continuity of the derivative, a row of the matrix is replaced by the requirement that

$$\sum_j D_{Nj}^{(k)} u_j^{(k)} = \sum_j D_{0j}^{(k+1)} u_j^{(k+1)}. \tag{3.43}$$

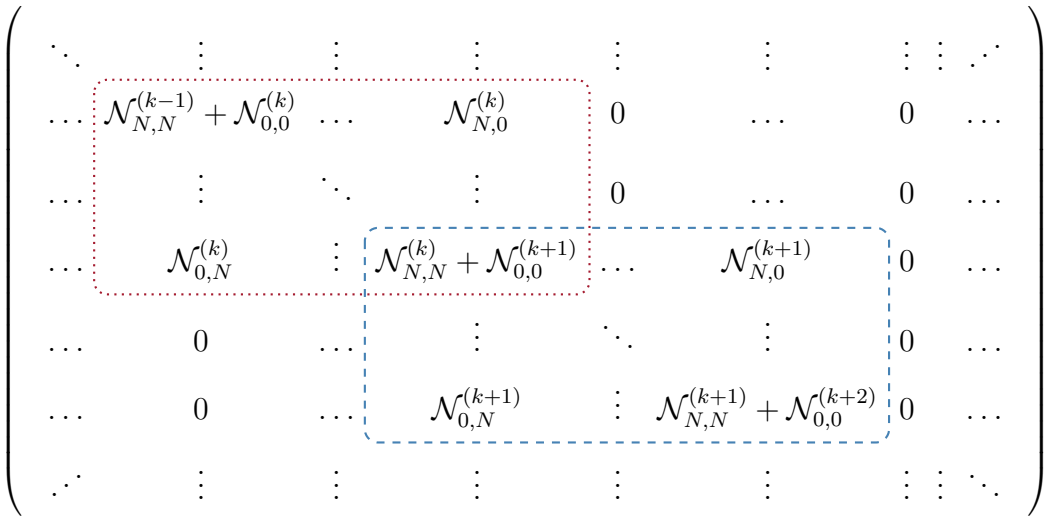

FIGURE 3.5: Sketch of effect for the requirement of continuity. The submatrices are overlapped such that the result of the matrix equation is continuous by removing coefficients of the solution which have to match.

Note that we have to take care that $u_N^{(k)} = u_0^{(k+1)}$. Once this matrix is constructed we can use the Newton-Raphson method as described in the previous subsection. The results for the example are shown in the right plot of figure 3.4.

NEWTON-KANTOROVICH

Another method which is also based on the Newton-Raphson method is the Newton-Kantorovich method (c.f., Appendix C of [42]). In this method, one linearizes the non-linear differential equation. To do so we rewrite the equation (3.33) in the form

$$u^{(p)} = F(x, \underbrace{u^{(0)}, \ldots, u^{(p-1)}}_{:=U}) \tag{3.44}$$

where the superscripts denote the corresponding derivative. Assuming we have a trial solution u_i which is close to the exact solution we can perform a Taylor expansion to obtain

$$u^{(p)} = F(x, U_i) + \sum_{k=0}^{p-1} \left.\frac{\partial F(x,U)}{\partial u^{(k)}}\right|_{U=U_i} \left[u^{(k)} - u_i^{(k)}\right] + \mathcal{O}\left(\left[u - u_i\right]^2\right). \tag{3.45}$$

For the iteration we set $u \to u_{i+1}$ and parametrize $u_{i+1} = u_i + \Delta$ to obtain

$$\Delta^{(p)} - \sum_{k=0}^{p-1} \left.\frac{\partial F(x,U)}{\partial u^{(k)}}\right|_{U=U_i} \Delta^{(k)} = F(x, U_i) - u_i^{(p)}. \tag{3.46}$$

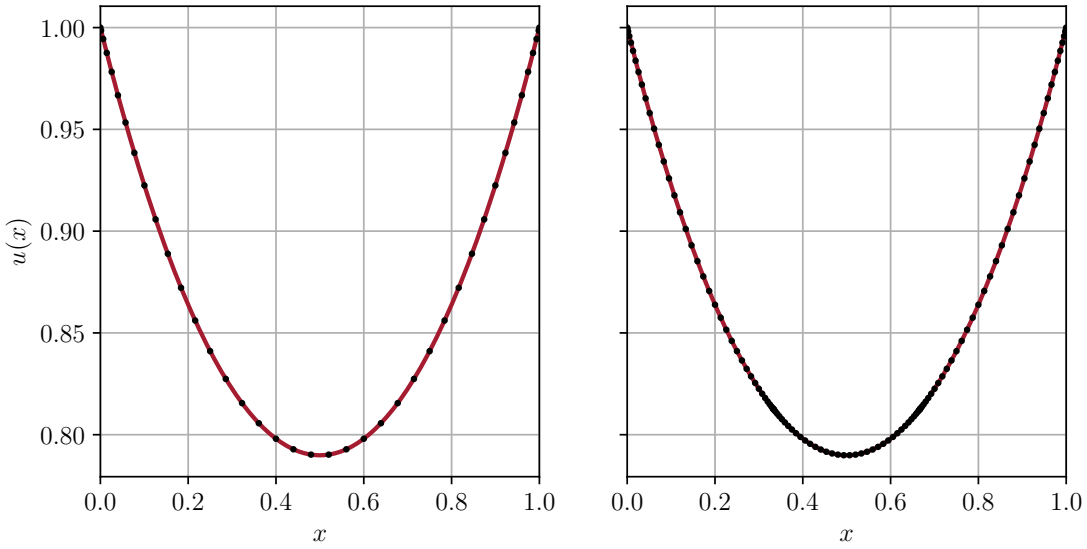

FIGURE 3.6: Comparison of the results of the inbuilt NDSOLVE function (red) and the Newton-Kantorovich method (black). The left plot is the result with a single domain while the right plot shows the results for multiple domains.

This is indeed a linear differential equation for Δ from which we can derive the next iteration

$$u_{i+1} = u_i + \Delta. \tag{3.47}$$

This linear equation can be solved with the methods described in the paragraphs above.
For the example (3.22), the linearized equation for Δ is given by

$$\Delta'' - 2u_i\Delta = 1 + u_i^2 - u_i''. \tag{3.48}$$

The results for this method are shown in figure 3.6 for single domain (left) and for multi domain (right). The clear advantage of this method is that one can apply the method of homogeneous solutions which can be easily parallelized. Additionally, we have to solve $3M$ times a system of size $(N+1)\times(N+1)$ and once a system of $(M+1)\times(M+1)$ for each iteration. Thus they are always smaller than for the Newton-Raphson method. Hence, this is computationally cheaper even though we have more equations to solve per iteration.

3.1.5.4 COUPLED NON-LINEAR EQUATIONS

In this section, we combine the methods used in the last sections to solve a set of coupled non-linear differential equations. We will use the Newton-Kantorovich

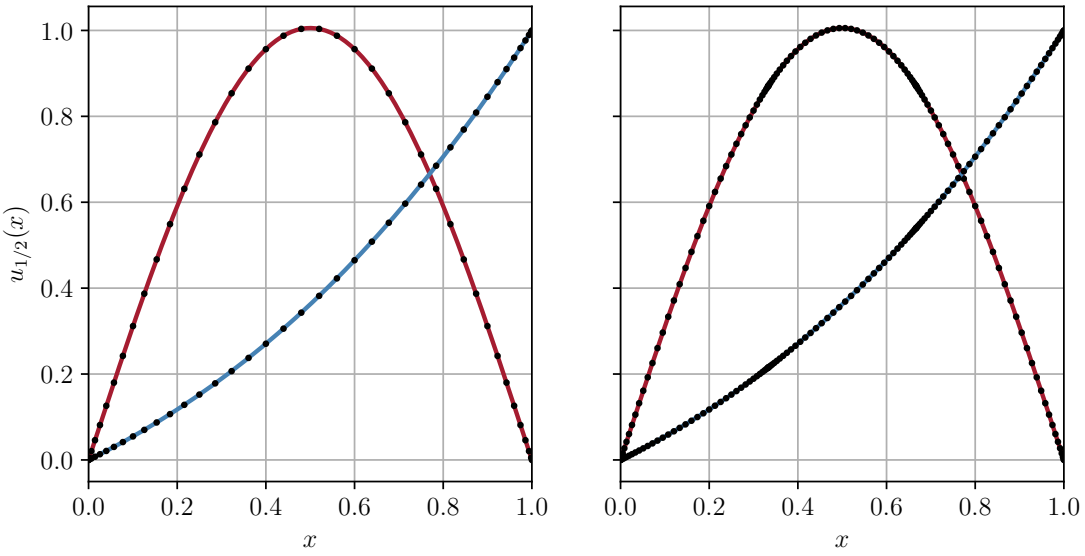

FIGURE 3.7: Comparison of the solution for the coupled non-linear differential equations with the NDSOLVE function (red,blue) and the pseudospectral method(red). The left plot shows the result with a single domain covering the whole computational domain while the right plot depicts the solution for domain decomposition.

method to linearize the problem. The example set of equations is given by

$$\begin{aligned} u_1'' - {u_2}^2 + u_1 + \frac{1}{64}(x+1)^6 + \pi^2 \sin(\pi x) - \sin(\pi x) = 0, \\ u_2'' - {u_2}^3 - x u_1 + \frac{1}{512}(x+1)^9 - \frac{3(x+1)}{4} + x \sin(\pi x) = 0 \end{aligned} \tag{3.49}$$

with boundary conditions $u_1(0) = u_1(1) = u_2(0) = 0$ and $u_2(1) = 1$.
First we derive the equations for Δ_1 and Δ_2 to obtain

$$\begin{aligned} \Delta_1'' + \Delta_1 - 2u_2\Delta_2 = u_2^2 - u_1 - \frac{1}{64}(x+1)^6 - \pi^2 \sin(\pi x) + \sin(\pi x) - u_1'', \\ \Delta_2'' - 3u_2^2\Delta_2 - x\Delta_1 = \\ u_2^3 + x u_1 - \frac{1}{512}(x+1)^9 + \frac{3(x+1)}{4} - x \sin(\pi x) - u_2''. \end{aligned} \tag{3.50}$$

Then we apply the techniques from the previous sections to solve this equation for $\Delta_{1/2}$ to obtain the next iterate. The results are shown in figure 3.7.

3.1.5.5 DIFFERENTIAL EQUATIONS OF OTHER ORDERS

For most of the problems mentioned above, to be precise for all but the one for the coupled linear equations, we considered a second order differential equation. For any other order only the method of homogeneous solutions changes by the number of the homogeneous solution in each subdomain. If we have M domains

and we have a P-th order derivative, we can specify P degrees of freedom in each subdomain, i.e. $P \cdot M$ in total. Thus we write the solution as

$$u(x) = u_p(x) + \sum_{i=1}^{P} u_i(x) A_i. \tag{3.51}$$

P of the coefficients A_i are then determined by the boundary conditions and another $P \cdot (M-1)$ for the matching conditions if we require that $u(x) \in C^{P-1}$. For example for a first order differential equation, we get

$$u(x) = u_p(x) + u_{l/r}(x) A. \tag{3.52}$$

It is arbitrary if we chose the function $u_{l/r}$ to be 1 at the left or the right side of the subdomain. But it is obvious that this decision should be made dependent on which end of the computational domain the boundary conditions are provided. If we assume that the boundary condition is given by $u(0) = a$ and the computational domain is $[0, 1]$ we would use u_l. In this case, the requirement for $u \in C^0$ would read

$$A^{(i)} u_l^{(i)} - A_{i+1} \underbrace{u_l^{(i+1)}}_{=1} = u_p^{(i+1)} - u_p^{(i)}. \tag{3.53}$$

Indeed this gives us $M-1$ constraints and together with the boundary conditions all coefficients are fixed.
This closes the discussion about the numerical solution methods for ODEs. In the next section we will apply these methods to solve Einstein's equations in asymptotically AdS spacetime.

3.2 Characteristic Formulation in Asymptotically AdS

In this section, we will show how we can write down the non-linear coupled Einstein's equations as a set of nested ODEs. This is the so-called characteristic formulation or Bondi-Sachs formulation [35, 36] which was pioneered by Chesler and Yaffe for asymptotically AdS spacetimes [28, 33, 37]. This technique is not very popular in the numerical GR community since the required null slices should not form caustics. In standard problems of GR, like black hole collisions and gravitational lensing, this happens quite generally [30]. On the other hand in problems in asymptotically AdS spacetimes, the formation of caustics is unlikely or at least hidden behind the horizon. In the numerical GR community a constant time slicing is mainly used which leads to the ADM formalism named after Richard Arnowitt, Stanley Deser and Charles W. Misner [44].

3.2.1 Characteristic Formulation

This review about the Bondi-Sachs or characteristic formalism is based on [28, 30, 45]. We start with Bondi-Sachs-coordinates[2] $(X) = (r, x) = (r, x^0 = t, x^i)$ and require that $t = const.$ defines a null-hypersufaces. That means the normal co-vector $k_A = -\nabla_A t$ satisfies $k^A k_A = 0$. Hence, we can conclude

$$g^{AB}\left(-\partial_B t\right)\left(-\partial_A t\right) = g^{AB}\delta^t_B\delta^t_A = g^{tt} = 0. \tag{3.54}$$

Additionally, the x^i are chosen such that they are constant along the null rays, i.e. they satisfy $k^A\partial_A x^i = 0$. Therefore, we get a second condition for the inverse metric, i.e.

$$g^{AB}\left(-\partial_B t\right)\partial_A x^i = -g^{AB}\delta^t_B\delta^i_A = -g^{it} = 0. \tag{3.55}$$

Since the components g^{tt} and g^{ti} of the inverse vanish, there are also constraints for the metric itself. These are given by

$$0 = \delta^t_r = g^{tA}g_{Ar} = g^{tr}g_{rr} + g^{tt}g_{tr} + g^{ti}g_{ir} = g^{tr}g_{rr}, \tag{3.56a}$$

$$0 = \delta^t_i = g^{tA}g_{Ai} = g^{tr}g_{ri} + g^{tt}g_{ti} + g^{tj}g_{ji} = g^{tr}g_{ri} \tag{3.56b}$$

and hence we conclude that $g_{rr} = g_{ri} = 0$. This choice of coordinates leads to the ansatz

$$ds^2 = 2dt\left[\beta(X)dr - A(X)dt - F_i(X)dx^i\right] + \Sigma(X)^2\hat{g}_{ij}(X)dx^i dx^j. \tag{3.57}$$

We require in the last term that the matrix $\hat{g}$ has unit determinant, $\det\left(\hat{g}_{ij}\right) = 1$. This metric is still invariant under reparametrizations in r and thus we have to fix this to obtain a well-posed initial-value problem. Bondi and Sachs did this by fixing $\Sigma(X) \equiv r$ suitable for spherical symmetry [35, 36]. We follow Chesler and Yaffe and set $\beta(X) \equiv 1$ [28, 33, 37] to arrive at the following metric ansatz

$$ds^2 = 2dt\left[dr - A(X)dt - F_i(X)dx^i\right] + \Sigma(X)^2\hat{g}_{ij}(X)dx^i dx^j. \tag{3.58}$$

[2] In this chapter, we use the following coordinate conventions. $(X) = (r, x) = (r, x^0 = t, x^i)$ is a vector in AdS spacetime, r is the radial AdS coordinate and $x^0 = t$ is the time component. We label the AdS coordinates with capital Latin letters $A, B, \ldots$, the boundary coordinates are labeled by lower case Greek letters $\alpha, \beta, \ldots$ and the spatial boundary coordinates are labeled by lower case Latin letters $a, b, \ldots$.

It is obvious that the form of this metric is still invariant under radial shifts, given by

$$r \to \overline{r} = r + \delta\lambda(x). \tag{3.59}$$

Inserting this in the metric ansatz (3.58) we can read off the transformation behaviors of the metric functions which are given by

$$\begin{aligned} A(x,r) &\to \overline{A}(x,\overline{r}) = A(x,\overline{r}-\delta\lambda) + \partial_t \delta\lambda(x), \\ F_i(x,r) &\to \overline{F}_i(x,\overline{r}) = F_i(x,\overline{r}-\delta\lambda) + \partial_i \delta\lambda(x), \\ \Sigma(x,r)^2\, \hat{g}_{ij}(x,r) &\to \overline{\Sigma}(x,\overline{r})^2\, \hat{\overline{g}}_{ij}(x,\overline{r}) = \Sigma(x,\overline{r}-\delta\lambda)^2\, \hat{g}_{ij}(x,\overline{r}-\delta\lambda). \end{aligned} \tag{3.60}$$

The transformation of A and F_i immediately reminds of gauge-invariant derivatives and thus, in analogy to gauge theories, we make this invariance manifest by defining "gauge-like" derivatives as

$$d_+ = \partial_t + A(X)\partial_r, \tag{3.61}$$

$$d_i = \partial_i + F_i(X)\partial_r. \tag{3.62}$$

The modified temporal derivative d_+ points along outgoing null geodesics, while the modified spatial derivatives d_i are orthogonal to the plane spanned by the tangents of outgoing and ingoing null geodesics.
With the ansatz (3.58) and by replacing temporal and spatial derivatives with these modified derivatives (d_+, d_i), we can write Einstein's equations

$$R^{AB} + \frac{1}{2} R\, g^{AB} - \Lambda\, g^{AB} = 0 \tag{3.63}$$

as a set of nested ODEs in radial direction. They are of the form

$$\left(\partial_r^2 + Q_\Sigma[\hat{g}]\right) \Sigma = 0, \tag{3.64a}$$

$$\left(\delta_j^i \partial_r^2 + P_F[\hat{g},\Sigma]_i^j \partial_r + Q_F[\hat{g},\Sigma]_i^j\right) F_j = S_F[\hat{g},\Sigma]_i, \tag{3.64b}$$

$$\left(\partial_r + Q_{d_+\Sigma}[\Sigma]\right) d_+\Sigma = S_{d_+\Sigma}[\hat{g},\Sigma,F], \tag{3.64c}$$

$$\left(\delta_{(i}^k \delta_{j)}^l \partial_r + Q_{d_+\hat{g}}[\hat{g},\Sigma]_{ij}^{kl}\right) d_+\hat{g}_{kl} = S_{d_+\hat{g}}[\hat{g},\Sigma,F,d_+\Sigma]_{ij}, \tag{3.64d}$$

$$\partial_r^2 A = S_A[\hat{g},\Sigma,F,d_+\Sigma,d_+\hat{g}], \tag{3.64e}$$

$$\left(\delta_i^j \partial_r + Q_{d_+F}[\hat{g},\Sigma]_i^j\right) d_+ F_j = S_{d_+F}[\hat{g},\Sigma,F,d_+\Sigma,d_+\hat{g},A]_i, \tag{3.64f}$$

$$d_+\left(d_+\Sigma\right) = S_{d_+^2\Sigma}[\hat{g},\Sigma,F,d_+\Sigma,d_+\hat{g},A]. \tag{3.64g}$$

In each of these equations, the square brackets indicate on which fields these terms depend. For planar shockwaves, the full forms of these equations can be found in appendix A.1.

With these equations in mind, we see that, once we know the initial $\hat{g}_{ij}$, we can solve (3.64a) by integrating it with respect to r. Afterwards, we can use this solution to solve (3.64b). We can continue like this until we have solved all of the equations and then perform a time step to the next time slice as we will describe below. To solve these equations we use pseudospectral methods as described in section 3.1.4.

To get unique solutions we have to specify boundary conditions encoding physics in the dual gauge theory in addition to the initial spatial metric tensor $\hat{g}_{ij}$.

To obtain the needed boundary conditions for differential equations (3.64) we analyze the near-boundary behavior of the different fields. This is obtained by solving equations (3.64) order by order in r. Doing so we obtain [28]

$$A = \frac{1}{2}(r+\lambda)^2 - \partial_t\lambda + a^{(4)}r^{-2} + \mathcal{O}\left(r^{-3}\right), \tag{3.65a}$$

$$F_i = -\partial_i\lambda + f_i^{(4)}r^{-2} + \mathcal{O}\left(r^{-3}\right), \tag{3.65b}$$

$$\Sigma = r + \lambda + \mathcal{O}\left(r^{-7}\right), \tag{3.65c}$$

$$\hat{g}_{ij} = \delta_{ij} + \hat{g}_{ij}^{(4)}r^{-4} + \mathcal{O}\left(r^{-5}\right), \tag{3.65d}$$

$$d_+\Sigma = \frac{1}{2}(r+\lambda)^2 + a^{(4)}r^{-2} + \mathcal{O}\left(r^{-3}\right), \tag{3.65e}$$

$$d_+\hat{g}_{ij} = -2\hat{g}_{ij}^{(4)}r^{-3} + \mathcal{O}\left(r^{-4}\right). \tag{3.65f}$$

Using the AdS/CFT dictionary the non-determined coefficients $a^{(4)}$, $f_i^{(4)}$ and $\hat{g}_{ij}^{(4)}$ can be mapped to the energy-momentum tensor of the dual gauge theory. For Eddington-Finkelstein (EF) coordinates this relation is given by [28, 46, 47]

$$\frac{2\pi^2}{N_c^2}\langle T_{\mu\nu}\rangle \equiv \left\langle \hat{T}_{\mu\nu}\right\rangle = g_{\mu\nu}^{(4)} + \frac{1}{4}g_{00}^{(4)}\eta_{\mu\nu} \tag{3.66}$$

where N_c is the number of colors in the dual field theory. The 4 dimensional metric $g_{\mu\nu}$ in this equation is related to parametrization (3.58) via

$$g_{00} = -\frac{2}{r^2}A, \qquad g_{0i} = -\frac{1}{r^2}F_i, \qquad g_{ij} = \frac{1}{r^2}\Sigma^2\hat{g}_{ij}. \tag{3.67}$$

Inserting the near-boundary expansion of the metric we arrive at

$$\left\langle \hat{T}_{00}\right\rangle = -\frac{3}{2}a^{(4)}, \qquad \left\langle \hat{T}_{0i}\right\rangle = -f_i^{(4)}, \qquad \left\langle \hat{T}_{ij}\right\rangle = \hat{g}_{ij}^{(4)} - \frac{1}{2}a^{(4)}. \tag{3.68}$$

The radial shift parameter $\lambda \equiv \lambda(x)$ is completely undetermined in the above near boundary expansion. We are free to set it to an arbitrary value and could, e.g. require that $\lambda(x) \equiv 0$. It turns out that there is a better choice. To cover the whole physics in the boundary theory we have to integrate from the boundary down to the horizon of the geometry. For general problems, this horizon can vary rapidly and thus we have a non-rectangular computational domain, which can cause numerical trouble. But using the freedom to arbitrarily choose $\lambda(x)$ we can require that the horizon lies at a fixed radial position

$$r_h(x) = \overline{r}_h = const. \tag{3.69}$$

Obviously, this results in a rectangular computational domain.
To see how to set the horizon at a constant radial position we follow [48]. The apparent horizon can be defined as the position where the expansion $\theta = \nabla \cdot k$ vanishes, where k is a null congruence. We start with an ansatz for the congruence

$$k_A = \mu(X)\partial_A \phi(X) \tag{3.70}$$

with arbitrary scalar functions $\mu(X)$ and $\phi(X)$. Since we are looking for a null congruence this ansatz has to satisfy

$$k^A k_A = 0 \qquad \Rightarrow \qquad \partial_t \phi = K_\phi \left(\partial_i \phi, \partial_r \phi\right) \tag{3.71}$$

where K_ϕ is a function independent of $\partial_t \phi$. In this calculation we used that $g^{tt} = g^{ti} = 0$ in EF coordinates. We also require that k is affinely parametrized, i.e.

$$k^B \nabla_B k_A = 0 \qquad \Rightarrow \qquad \partial_t \mu = K_\mu \left(\partial_i \mu, \partial_r \mu\right). \tag{3.72}$$

With these two relations and our ansatz (3.58) we can write down the expansion $\theta = \nabla \cdot k$ and demand that it vanishes on a surface $\phi(X) = const.$ This surface defines then an apparent horizon [48]. We want this surface to be at $\overline{r}_h \equiv const$ and thus set $\phi(X) \equiv r$. Finally, we obtain a condition for $d_+\Sigma$ given by

$$d_+\Sigma\Big|_{r_h} = -\frac{1}{2}\partial_r \Sigma F^2 - \frac{1}{3}\Sigma \nabla \cdot F. \tag{3.73}$$

The position of the horizon should be fixed at any time and thus this condition has to hold at all times, i.e.

$$\partial_t d_+\Sigma\Big|_{r_h} = \partial_t \left(-\frac{1}{2}\partial_r \Sigma F^2 - \frac{1}{3}\Sigma \nabla \cdot F\right). \tag{3.74}$$

field	asymptotic homogeneous solution(s)	boundary behavior
Σ	r^1 and r^0	$\Sigma \sim r + \lambda$
F_i	r^2 and r^{-2}	$F_i \sim -\partial_i \lambda + f_i^{(4)} r^{-2}$
$d_+\Sigma$	r^{-2}	$d_+\Sigma \sim \frac{1}{2}(r+\lambda)^2 + a^{(4)} r^{-2}$
$d_+\hat{g}_{ij}$	$r^{-3/2}$	$d_+\hat{g}_{ij} \sim 0$
A	r^1 and r^0	$A \sim \frac{1}{2}(r+\lambda)^2 - \partial_t \lambda$

TABLE 3.1: Homogeneous solutions and asymptotic behavior of the different fields.

The full form of equations (3.73) and (3.74) with expanded covariant derivative for planar shockwaves can be found in appendix A.1.
In this section, we outlined how we can use the characteristic formulation to rewrite the coupled non-linear Einstein's equations (3.63) in a set of nested ODEs (3.64) which we can then solve using pseudospectral methods described in section 3.1.

3.2.2 Solving Strategy

We want to solve the set of nested ODEs (3.64) using pseudospectral methods. But to get a uniquely determined solution we have to implement boundary conditions. These conditions can be obtained by matching the near boundary analysis (3.65) with the homogeneous solutions of the differential equations. This is done in table 3.1 where we can read off the boundary conditions directly. As already mentioned the radial shift parameter $\lambda(x)$ is chosen such that the horizon lies at a fixed radial position. Once we fixed the radial shift parameter, we can solve the differential equations on the first time slice and then evolve the initial and boundary conditions $\{\hat{g}_{ij}, f_i^{(4)}, a^{(4)}, \lambda\}$ to the next time slice.
For the time evolution, we use a Runge-Kutta (RK) time stepper. The time evolution equations are derived in what follows.
We can use the definition of the modified temporal derivative d_+ to get the time evolution for the spatial metric $\hat{g}_{ij}$

$$\partial_t \hat{g}_{ij} = d_+ \hat{g}_{ij} - A \partial_r \hat{g}_{ij}. \tag{3.75}$$

With a similar procedure, we can get the time evolution of the radial shift parameter λ

$$\partial_t \lambda = \lim_{r\to\infty} (d_+\Sigma - A). \tag{3.76}$$

We could go on like this for $f_i^{(4)}$ and $a^{(4)}$, but we can also use physical input, namely that the boundary energy-momentum tensor is conserved, i.e. $\nabla^\mu \left\langle \hat{T}_{\mu\nu} \right\rangle = 0$.

Using (3.66) we can express the time evolution as

$$\partial_t a^{(4)} = \frac{3}{2}\partial_i f_i^{(4)}, \qquad \partial_t f_i^{(4)} = \frac{1}{2}\partial_i a^{(4)} - \partial_i \hat{g}_{ij}. \tag{3.77}$$

This turns out to be numerically more stable [28]. With this, we know how to transform the problem of solving coupled non-linear Einstein's equations (3.63) to the problem of solving a set of nested ODEs by using EF coordinates.
The initial setup we have in mind are colliding gravitational shockwaves. Unfortunately there exist no analytic solutions to Einstein's equations in EF coordinates, which we would need as initial conditions. There is a solution in Fefferman-Graham (FG) coordinates [29, 49, 50]

$$ds^2 = \tilde{\rho}^{-2}\left(-d\tilde{t}^{\,2} + d\tilde{\mathbf{x}}_\perp^2 + d\tilde{z}^2 + d\tilde{\rho}^2 + H_\pm(\tilde{\mathbf{x}}_\perp, \tilde{x}_\mp, \tilde{\rho}) d\tilde{x}_\pm^2\right) \tag{3.78}$$

with $\tilde{x}_\pm = \tilde{t} \pm \tilde{z}$. Plugging this into Einstein's equations (3.63) we obtain a constraint for the function $H_\pm$ given by

$$\left(\partial_{\tilde{\rho}}^2 - \frac{3}{\tilde{\rho}}\partial_{\tilde{\rho}} + \nabla_\perp^2\right) H_\pm = 0. \tag{3.79}$$

For a general solution to this equation, one can use a Fourier transformation as it was done in [29]. We will later drop the transverse $\tilde{x}_\perp$ dependence and hence we will be able to analytically solve the differential equation for $H_\pm$.
Once this $H_\pm$ is fixed we have to perform a coordinate transformation to EF coordinates to be able to use the method proposed above.
To obtain the equations for the coordinate transformation we demand that the resulting metric has the required EF form (3.58). Alternatively, we can proceed as follows: A path along r in EF coordinates satisfies the geodesic equation. Since coordinate transformations are isometries, the same path in FG coordinates also satisfies the equations. The needed equation then reads

$$\frac{d^2\widetilde{Y}^A}{dr^2} + \widetilde{\Gamma}^A_{BC}\frac{d\widetilde{Y}^B}{dr}\frac{d\widetilde{Y}^C}{dr} = 0 \tag{3.80}$$

where $\widetilde{\Gamma}^A_{BC}$ are the Christoffel symbols evaluated in FG coordinates. These non-linear coupled equations can then be solved using the methods described in section 3.1. Explicit expressions for the case of planar shocks can be found in appendix A.2 and a more detailed description of the procedure is given in section 3.4. The discussion of this section is valid for 5 dimensional asymptotically AdS spacetime, but can be arbitrarily extended to any other dimension in a straightforward manner by changing just some factors [28].

After this general treatment of the characteristic formulation in asymptotically AdS space, we will restrict ourselves from now on to planar shocks and thus neglect transverse spatial dependence of the incoming shocks, i.e we assume that the shocks have an infinite extent in the transverse directions. The clear advantage is that we can reduce the dimensionality and thus reduce complexity and computational costs for numerically solving the differential equations.
We will argue in the next section why this still allows to get physical insight into off-center HICs in a leading order approximation. Afterwards, we will provide details of the performed calculation for asymmetric planar shockwaves.

3.3 Motivation for Planar Asymmetric Shocks

From now on, we will restrict ourselves to planar shocks with no transverse spatial dependence. Thus we can solve the differential equation (3.79) analytically to obtain

$$H_{\pm}(\tilde{x}_{\pm}, \tilde{\rho}) = \tilde{\rho}^4 h_{\pm}(\tilde{x}_{\pm}) \tag{3.81}$$

with arbitrary $h_{\pm}$. Furthermore, for the sake of numerical stability, we restrict ourselves to Gaussian shockwaves, i.e. we choose

$$h_{\pm}(\tilde{x}_{\pm}) = \mu_{\pm}^3 \frac{1}{\sqrt{2\pi\omega_{\pm}^2}} e^{-\frac{1}{2}\tilde{x}_{\pm}^2/\omega_{\pm}^2}. \tag{3.82}$$

The energy scale $\mu_{\pm}$ characterizes the transverse energy density of each incoming shock and is defined by the integrated energy density of the incoming shock

$$\mu_{\pm} = \int dz \; \hat{T}^{00}(t \pm z)_{\text{incoming}}. \tag{3.83}$$

For the simulations, we choose to work in the Center-of-Momentum (CM) frame in which the energy densities of the incoming shocks are equal, i.e.

$$\mu \equiv \mu_+ = \mu_-. \tag{3.84}$$

In this frame physical results only depend on two independent dimensionless combinations which we choose to be $\mu\omega_+$ and $\mu\omega_-$.
As shown in figure 3.1 HICs go through different stages. We are interested in the hydrodynamization and formation of a QGP. We will argue in what follows that considering planar asymmetric shocks are a leading order approximation for off-center collisions. In principle, the following argument is the leading term in an expansion in transverse gradients ($\omega \ll \delta \ll L$).

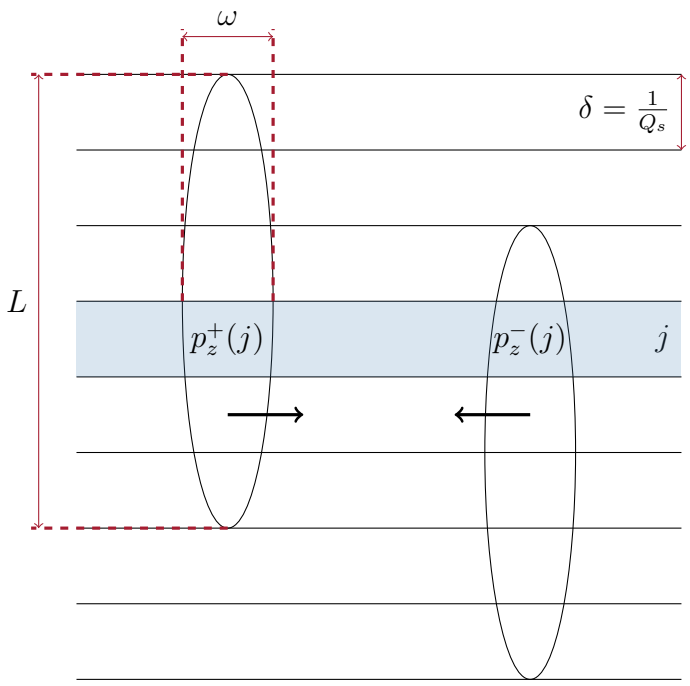

FIGURE 3.8: Visualization why the asymmetric planar shocks are the leading order in an expansion in transverse gradients. Assuming $\omega \ll \delta \ll L$, the planar approximation gives reliable results.

The following argument is illustrated in figure 3.8.

Step 1 Decompose the incoming projectiles in subregions in the transverse plane. We call them "pixels" and we require that they have size $\delta = \frac{1}{Q_s}$ which is small compared to the transverse extent ($\delta \ll L$), but large compared to the longitudinal width of the shock ($\delta \gg \omega$). Q_s is the so-called "saturation" scale which is roughly 1 GeV and hence $\delta = \frac{1}{Q_s} \sim 0.2\,\text{fm}$. At the LHC the longitudinal extent ω is about $\frac{10\,\text{fm}}{\gamma} \sim 0.01\,\text{fm} \ll 0.2\,\text{fm}$ where we used $\gamma \approx 7460$.

Step 2 Let j label independent transverse-plane pixels, with $p_z^\pm(j)$ the portion of the longitudinal momentum of each the incident projectile.

Step 3 For each pixel j, transform to the CM frame in which the total longitudinal momentum within the pixel vanishes, and evaluate the resulting energy scale $\mu(j)$ and incident projectile widths $w_\pm(j)$ for this pixel. Explicitly, $\mu(j)^6 = 4\,p_z^+(j)\,p_z^-(j)/\delta^4$.

Step 4 We can use the results which we will describe in section 3.5 to model the energy-momentum tensor $T^{\mu\nu}(j)$ at the initial proper time τ_{init}.

Step 5 Transform each pixel's energy-momentum tensor $T^{\mu\nu}(j)$ from its CM frame back to the original (lab) frame.

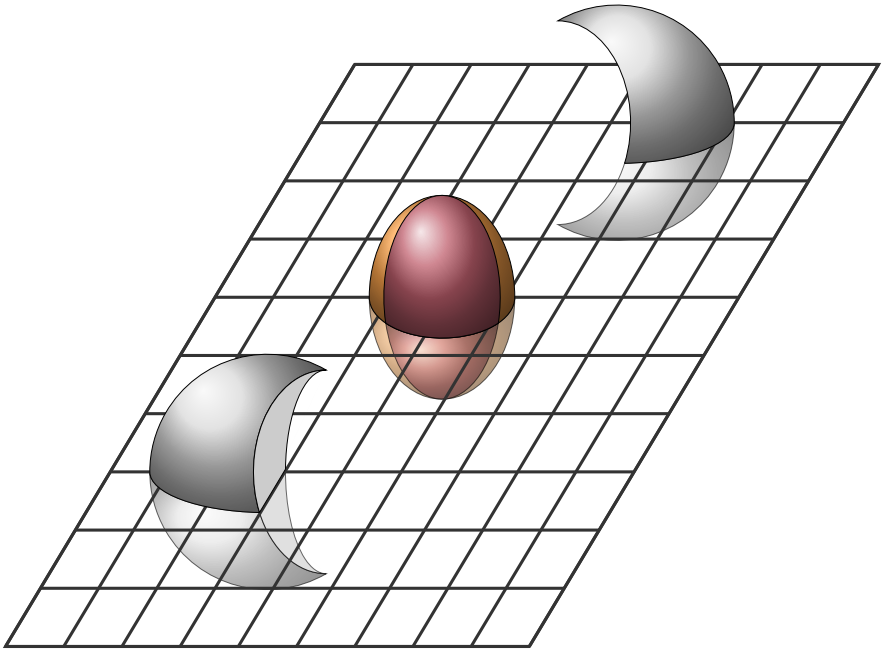

FIGURE 3.9: Sketch of off-center HICs. The almond-shaped overlap region forms a QGP, not the spectator portions (grey). The hydrodynamization time increases rapidly as one approaches the boundary of the overlap region.

Putting all different pixels together we have the full energy-momentum tensor on the initial proper time surface τ_{init} for off-center collisions. These data can then be used as initial data for hydrodynamic simulations. The advantage of this approximation is that one does not need to perform the full (5d) simulations which are numerically very demanding [29].
Pixels near the periphery of the overlap region of the colliding nuclei (cf. figure 3.9), will have decreasing CM frame transverse energy density μ^3. Since the hydrodynamization time scales inversely with μ, this implies that pixels near the periphery of the overlap region (shown in orange) enter the hydrodynamic regime later than pixels in the middle of the overlap region.
In this section, we motivated the usage for planar asymmetric shockwave collisions. In the next section, we will describe in detail how to write computer software to apply the characteristic method described in section 3.2.

3.4 Computational Details for Planar Shockwave Collisions

As we have already mentioned in section 3.2 we can write the coupled non-linear Einstein's equations (3.63) as a set of nested differential equations (3.64). This is only possible in EF coordinates with the metric ansatz (3.58). Hence, we have to perform the coordinate transformation from FG to EF coordinates also described

in section 3.2. We start with the metric (3.78) and we have already seen that for a vanishing transverse dependence this reduces to (3.81). For the parametrization of the coordinate transformation equations, we follow [28] and choose

$$\tilde{t} = t + u + \alpha(t - z, u), \quad \tilde{\mathbf{x}}_\perp = \mathbf{x}_\perp, \tag{3.85a}$$

$$\tilde{z} = z - \gamma(t - z, u), \quad \tilde{\rho} = u + \beta(t - z, u) \tag{3.85b}$$

where $u \equiv \frac{1}{r}$ is the inverted radial coordinate. As already mentioned above, there exist two ways to obtain the equations for the coordinate transformation. As in [28] we will combine both of them and furthermore introduce the fields

$$\alpha = -\gamma + \beta + \delta, \quad \beta = -\frac{u^2\zeta}{1 + u\zeta} \tag{3.86}$$

to be able to decouple one of the equations. Finally, we arrive at

$$\begin{aligned} &\frac{1}{u^2}\frac{\partial}{\partial u}\left(u^2\frac{\partial\zeta}{\partial u}\right) + \frac{2uH}{(1+u\zeta)^5} = 0, \quad \frac{\partial\delta}{\partial u} - \frac{u^2}{(1+u\zeta)^2}\frac{\partial\zeta}{\partial u} = 0, \\ &\frac{\partial\gamma}{\partial u} - \frac{u^2}{(1+u\zeta)^2}\frac{\partial\zeta}{\partial u} + \frac{u^4}{2(1+u\zeta)^2}\left(\frac{\partial\zeta}{\partial u}\right)^2 + \frac{u^4 H}{2(1+u\zeta)^6} = 0 \end{aligned} \tag{3.87}$$

with $H = h_+\left(t - z + u + \delta - u^2\zeta/(1+u\zeta)\right)$. To get more accurate results it is essential to exploit the near boundary asymptotics. Again this asymptotics can be found by solving the equations order by order in u. The expansion for $\beta_0 = 0$ is given by

$$\tilde{\beta}|_{\tilde{\beta}_0=0} = u^3\sum_{i=0}^{\infty} b_i u^i, \quad \tilde{\alpha}|_{\tilde{\beta}_0=0} = u^4\sum_{i=0}^{\infty} a_i u^i, \quad \tilde{\gamma}|_{\tilde{\beta}_0=0} = u\sum_{i=0}^{\infty} g_i u^i \tag{3.88}$$

and for arbitrary β_0 is reads

$$\tilde{\beta} = \sum_{i=1}^{\infty}(-u)^{i-1}\tilde{\beta}_0^i - u^3\sum_{i=0}^{\infty} b_i u^i \sum_{j=-1}^{\infty}\binom{5+j+i}{1+j}\tilde{\beta}_0^{1+j}(-u)^{1+j}, \tag{3.89a}$$

$$\tilde{\alpha} = \sum_{i=1}^{\infty}(-u)^{i}\tilde{\beta}_0^i - u^4\sum_{i=0}^{\infty} a_i u^i \sum_{j=-1}^{\infty}\binom{5+j+i}{1+j}\tilde{\beta}_0^{1+j}(-u)^{1+j}, \tag{3.89b}$$

$$\tilde{\gamma} = u\sum_{i=0}^{\infty} g_i u^i \sum_{j=-1}^{\infty}\binom{5+j+i}{1+j}\tilde{\beta}_0^{1+j}(-u)^{1+j}. \tag{3.89c}$$

The series coefficients can be found in appendix A.3.

We need a solution for the differential equations (3.87) from the boundary $u \equiv 0$ down to the horizon. A priori we do not know where the horizon lies and thus we solve the differential equations to a coordinate value which we hope to lie behind the horizon. This requires some trial and error. The point $u = 0$ is a regular

singular point and thus standard integrators as RK fail to give accurate results there. Therefore, we apply spectral methods described in section 3.1. This method can easily cope with this regular singular point. Going deeper into the bulk and thus coming closer to or even behind the horizon the functions parameterizing the coordinate transformation will grow very fast. Hence, spectral methods which cover the whole computational domain will fail. To deal with this difficulty we solve to a fixed depth using spectral methods and switch to an adaptive integrator afterwards.

Adding an additional background energy density which pushes the horizon towards the boundary stabilizes the numerical procedure.

Once equations (3.87) are solved, we can use the characteristic formulation described in 3.2 to solve Einstein's equations. To do so we will further parameterize the spatial metric $\hat{g}_{ij}$ by the anisotropy function $B(u, t \pm z)$ as

$$\hat{g}_{ij} = \begin{pmatrix} e^B & 0 & 0 \\ 0 & e^B & 0 \\ 0 & 0 & e^{-2B} \end{pmatrix}. \tag{3.90}$$

To read off the anisotropy function we have to look at the dz^2 component of the transformed metric. For this, we have a look at the following transformations

$$d\tilde{t} \to (\partial_z \alpha)\, dz + \dots \tag{3.91a}$$

$$d\tilde{\rho} \to (\partial_z \beta)\, dz + \dots \tag{3.91b}$$

$$d\tilde{z} \to (1 - \partial_z \gamma)\, dz + \dots \tag{3.91c}$$

where the dots refer to components which are not $\propto dz$. Writing down the metric for a shock moving in $+z$ direction and inserting the above transformations together with (3.85) we obtain

$$\left[\frac{-(\partial_z \alpha)^2 + (1 - \partial_z \gamma)^2 + (\partial_z \beta)^2}{(u+\beta)^2} + (u+\beta)^2 H \left(1 - \partial_z \alpha - \partial_z \gamma\right)^2 \right] dz^2. \tag{3.92}$$

From this, we can simply take the logarithm and read off the anisotropy function B

$$B = \frac{1}{3} \log \left[\frac{-(\partial_z \alpha)^2 + (1 - \partial_z \gamma)^2 + (\partial_z \beta)^2}{(u+\beta)^2} + (u+\beta)^2 H \left(1 - \partial_z \alpha - \partial_z \gamma\right)^2 \right]. \tag{3.93}$$

A similar exercise with the corresponding near boundary asymptotics (3.65) gives

$$a_+^{(4)} = -\frac{2}{3} h_+, \qquad f_{z+}^{(4)} = h_+, \qquad \lambda_+ = -\frac{1}{2} \partial_u^2 \beta \Big|_{u=0}. \tag{3.94}$$

The discussion above holds for shocks in $+z$ direction. For colliding shocks we have to do the same for shocks moving in opposite $-z$ direction. This can be simply achieved by using the following relation

$$B(u, t - z) \to B(u, t + z), \tag{3.95a}$$
$$a^{(4)}(t - z) \to a^{(4)}(t + z), \tag{3.95b}$$
$$f^{(4)}(t - z) \to -f^{(4)}(t + z), \tag{3.95c}$$
$$\lambda(t - z) \to \lambda(t + z). \tag{3.95d}$$

To obtain starting configurations we separate the shocks by a distance Δz. As shown in [28] there will always be a region for which a right moving and a left moving shock overlap inside the bulk no matter how far they are separated on the boundary. Inside this region, a simple superposition of spatially separated shocks will not give a correct solution to Einstein's equations. However, in [28] it is pointed out that this region lies inside the horizon for a sufficiently large spatial separation of the two shocks on the boundary. Therefore it is allowed to set

$$B_{\text{total}}(u, t_0, z) = B(u, t_0 - z) + B(u, t_0 + z), \tag{3.96a}$$
$$a^{(4)}_{\text{total}}(t_0, z) = a^{(4)}(t_0 - z) + a^{(4)}(t_0 + z), \tag{3.96b}$$
$$f^{(4)}_{\text{total}}(t_0, z) = f^{(4)}(t_0 - z) - f^{(4)}(t_0 + z), \tag{3.96c}$$
$$\lambda_{\text{total}}(t_0, z) = \lambda(t_0 - z) + \lambda(t_0 + z) \tag{3.96d}$$

for the total functions corresponding to two shocks moving towards each other with the speed of light, separated by $\Delta z = -2t_0$. One problem with this starting configuration remains to be fixed: The overlap of the shift functions $\lambda_\pm$ of the left and right moving shocks in the region close to $z = 0$ is significant. All other functions have negligible overlap. Since we choose the shocks on the first time slice well separated, we can assume that the geometry in between is pure AdS, which justifies to modify λ_{total} close to $z = 0$, without changing $B_{\text{total}}, a^{(4)}_{\text{total}}, f^{(4)}_{\text{total}}$. As in [28] we set

$$\lambda_{\text{total}}(t_0, z) = \theta(-z)\lambda(t_0 - z) + \theta(z)\lambda(t_0 + z) \tag{3.97}$$

with

$$\theta(z) = \frac{1}{2}\left(1 - \text{erf}\left(\frac{-z}{\sqrt{2}w}\right)\right). \tag{3.98}$$

In practice, we add a uniform background energy density to increase the numerical stability. To do so we follow [28, 29] and modify the superposition (3.96b) with

$$a^{(4)}_{\text{total}}(t_0, z) = a^{(4)}(t_0 - z) + a^{(4)}(t_0 + z) - \frac{2}{3}\epsilon_0. \tag{3.99}$$

This added background energy means physically that the colliding shocks will propagate through a thermal medium. But the chosen background energies are small enough that the background is very cold compared to the energy scale μ of the shocks. Hence the dissipation in the medium is small. For the presented results in section 3.5 we will linearly extrapolate to a vanishing background energy density, $\epsilon_0 = 0$.

As already mentioned the integration depth is arbitrary up to now, we just have to ensure that it reaches behind the horizon such that we can solve equation (3.73) which for planar shocks reads

$$d_+\Sigma\Big|_{r=r_h} = -\frac{e^{2B}}{3}\left(\frac{3F^2}{2\Sigma^2}\partial_r\Sigma + \frac{\partial_z F}{\Sigma} + \frac{F}{\Sigma^2}(2\Sigma\partial_z B + \partial_z\Sigma)\right)\Bigg|_{r=r_h}. \tag{3.100}$$

With this equation we want to find the radial shift $\delta\lambda(t, z)$ such that for

$$u = \frac{\overline{u}}{1 + \overline{u}\delta\lambda} \tag{3.101}$$

where $u(\overline{u}_{\max})$ is the radial position of the horizon. Finally, this results in a planar horizon and a rectangular computational domain. To solve the non-linear differential equation (3.100) we linearize it in $\delta\lambda$ to be able to apply a Newton-Raphson root-finding algorithm to determine $\delta\lambda$. As already mentioned adding a background energy density will push the horizon towards the boundary. We found it advantageous to start with a rather big value of about 10%, find the horizon and then use the obtained $\delta\lambda$ as the starting point for a smaller background energy density. During the time evolution, the stationary requirement (3.74) keeps the radial position of the horizon fixed, but due to numerical uncertainties, it is also necessary to correct the shift every $10-100$ time steps depending on the parameters of the simulation.

Once we have the initial conditions $\{B, a^{(4)}, f^{(4)}, \lambda\}$, we can solve the nested set of differential equations (3.64). As can be seen from the near boundary analysis (3.65) some fields diverge at the boundary ($r \to \infty$ or $u \equiv \frac{1}{r} = 0$). To avoid numerical

precision loss, we use the following redefinitions

$$B(u,z,t) = \left(\frac{u}{1+u\lambda(t,z)}\right)^3 b(u,z,t), \tag{3.102a}$$

$$\Sigma(u,z,t) = \frac{1}{u} + \lambda(t,z) + \left(\frac{u}{1+u\lambda(t,z)}\right)^4 \sigma(u,z,t), \tag{3.102b}$$

$$F(u,z,t) = -\partial_z\lambda(t,z) + \left(\frac{u}{1+u\lambda(t,z)}\right)^2 f(u,z,t), \tag{3.102c}$$

$$d_+\Sigma(u,z,t) = \frac{1}{2}\left(\frac{1}{u} + \lambda(t,z)\right)^2 + \left(\frac{u}{1+u\lambda(t,z)}\right)^2 d_+\sigma(u,z,t), \tag{3.102d}$$

$$d_+B(u,z,t) = \left(\frac{u}{1+u\lambda(t,z)}\right)^2 d_+b(u,z,t), \tag{3.102e}$$

$$A(u,z,t) = \frac{1}{2}\left(\frac{1}{u} + \lambda(t,z)\right)^2 + a(u,z,t). \tag{3.102f}$$

After replacing the fields in (3.64) we solve the equations one after another for the functions σ, f, $d_+\sigma$, d_+b and a. The boundary conditions which we have to implement can be deduced from table 3.1 and are given by

$$\sigma\Big|_{u=0} = 0, \qquad \partial_u\sigma\Big|_{u=0} = 0, \tag{3.103a}$$

$$f\Big|_{u=0} = f^{(4)}, \qquad \partial_u f\Big|_{u=0} = \frac{8b^{(4)}}{3}, \tag{3.103b}$$

$$d_+\sigma\Big|_{u=0} = a^{(4)}, \qquad \partial_u d_+\sigma\Big|_{u=0} = \frac{\partial_z f^{(4)}}{3}, \tag{3.103c}$$

$$d_+b\Big|_{u=0} = 0, \qquad \partial_u d_+b\Big|_{u=0} = -2b^{(4)}, \tag{3.103d}$$

$$a\Big|_{u=0} = 0, \qquad \partial_u a\Big|_{u=0} = 0. \tag{3.103e}$$

After we used these initial conditions we can solve equations (3.64) on the first time slice and then use the time evolution equations (3.75), (3.76), and (3.77) and a RK stepper to evolve the initial conditions to the next time slice.
In this section, we gave details on how to write software to solve Einstein's equations in asymptotically AdS spacetime. In the following section, we will show results for symmetric and asymmetric shockwave collisions and we will also analyze them with respect to hydrodynamization.

3.5 Numerical Results

In this section, we review the results we obtained in [1] by applying the techniques described in the last sections. We solved the shockwave setup for several parameters which we list in table 3.2.

run	w_+	w_-	$(\epsilon_0)_1$	$(\epsilon_0)_2$	N_z
1	0.35	0.35	0.055	0.066	720
2	0.25	0.25	0.039	0.045	480
3	0.1	0.25	0.015	0.017	660
4	0.1	0.1	0.015	0.017	600
5	0.075	0.35	0.012	0.015	660
6	0.075	0.25	0.012	0.015	660
7	0.075	0.075	0.012	0.015	600

TABLE 3.2: Configurations calculated for the result section 3.5. We display the width of the incoming shocks $\omega_\pm$, the background energy densities ϵ_0 and the number of grid-points in z direction N_z.

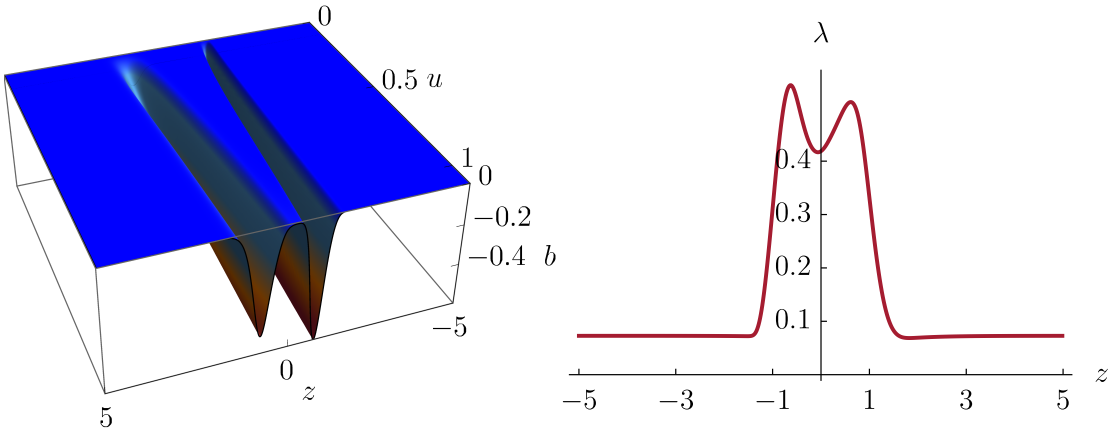

FIGURE 3.10: Initial conditions b (left) and λ (right) for $\omega_+ = 0.075$, $\omega_- = 0.25$ and with background energy density $\epsilon_0 = 0.015$ (run #6). $a^{(4)}$ and $f^{(4)}$ are directly given by the shock function $h(x_\pm)$ via equations (3.94).

We apply periodic boundary conditions in the spatial z direction and use a uniformly spaced Fourier grid with up to 720 grid-points in that direction. The period L_z in z direction is 10, 11 and 12 for narrow, asymmetric and wide shocks respectively. We partition the radial direction in $M = 22$ subdomains of uniform size in the inverted radial coordinate $u \equiv \frac{1}{r}$. In each of these subdomains, a Chebyshev-Gauss-Lobatto grid (3.15) with $N_u = 13$ grid-points is used. For the time evolution we use a fourth-order RK time stepper with stepsize $\delta t = 0.002$ to a final time ranging from $t \in [4/\mu, 20/\mu]$.

Let us illustrate some intermediate results for an example setup. For this purpose we use run #6, i.e. $(\omega_+, \omega_-) = (0.075, 0.25)$ and the added background energy density is given by $\epsilon_0 = 0.015$. In figure 3.10 we plot the initial conditions $\{b, \lambda\}$ for this configuration.

These conditions are obtained by numerically solving the coordinate transformation equations (3.87) and then extracting the corresponding values. These initial conditions are then time evolved. The (rescaled) energy density $\hat{T}^{00}$ for an exam-

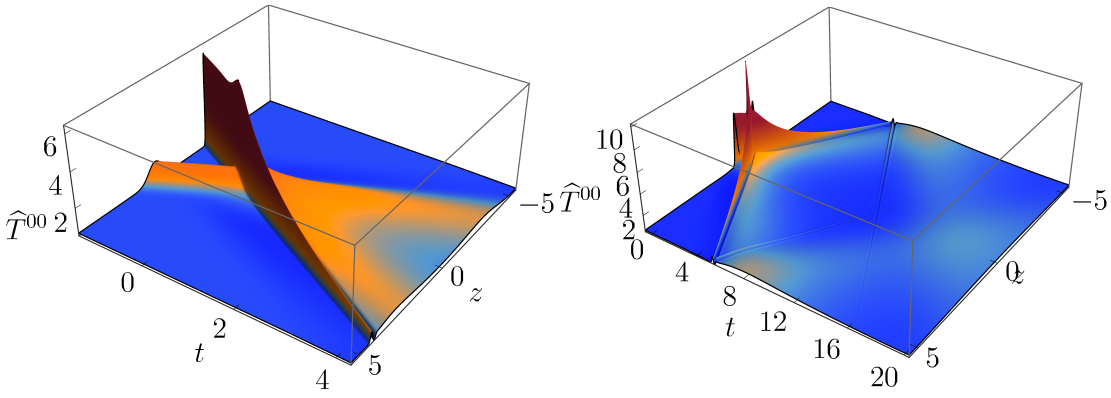

FIGURE 3.11: (Rescaled) energy-momentum tensor $\widehat{T}^{00}$ for asymmetric (left) and symmetric (right) shock collisions. For the asymmetric shock we have $(\omega_+, \omega_-) = (0.075, 0.35)$ while for the symmetric one we have $\omega_\pm = 0.075$.

ple setup is shown in figure 3.11 for asymmetric and symmetric shock collisions. The right plot shows a very long time evolution and thus we see artefacts form the imposed periodicity. That we are able to see these wrap-around artefacts proves the good stability of our code.

In figure 3.12 we plot the local maxima in the energy density. They lie on the forward light cone but outside the hydrodynamic regime which we will discuss below. For the symmetric shocks, we confirm the results published in earlier works [28, 30, 34] and reproduce that in the late time regime this local maximum decreases with $t^{-0.9}$. For asymmetric shocks, this local maximum coincides with the symmetric results after a very short time period and then also results in the same power law fall-off.

Similar results are obtained for all other configurations which we studied.

3.5.1 Hydrodynamic Flow

We want to calculate the hydrodynamization time in this holographic setup. The QGP is almost a perfect fluid and thus it is very well described by hydrodynamics which we reviewed in section 2.5. In this section, we will see at what times the post-collision energy-momentum tensor is well described by hydrodynamics. We will also extend the result of [2] to asymmetric shocks.

To be able to judge the quality of the hydrodynamic approximation we first calculate the proper energy density and the fluid 4-velocity as the eigenvalue and the real, normalized ($u_\mu u^\mu = -1$) future-directed ($u^0 > 0$) eigenvector of the full

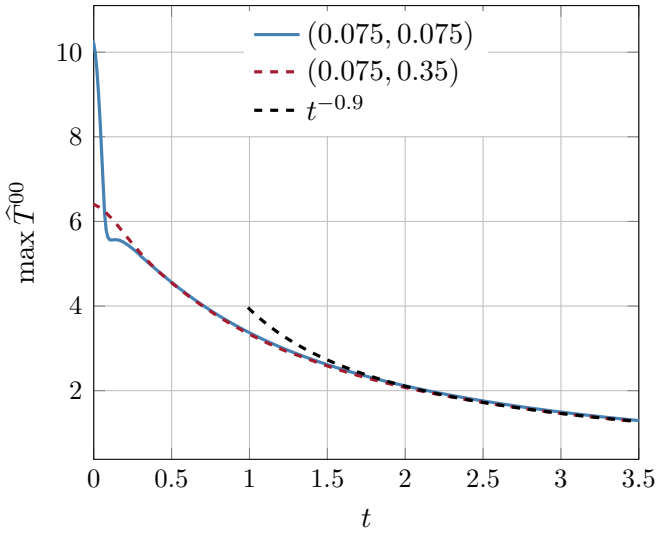

FIGURE 3.12: Maxima of the energy density for symmetric ($\omega_\pm = 0.075$) and asymmetric ($(\omega_+, \omega_-) = (0.075, 0.35)$) collisions. We see that after a short time $t \sim 0.5$ the amplitude for both setups coincides more or less. Furthermore we see that the late time behavior can be expressed by $t^{-0.9}$ as it was found in early results [28].

energy-momentum tensor, which we obtain from our simulation[3]

$$T^{\mu}{}_{\nu} u^{\nu} = -\epsilon\, u^{\mu}. \tag{3.104}$$

After we extracted these parameters we can calculate the hydrodynamic energy-momentum tensor $T^{\mu\nu}_{\text{hydro}}$ using equation (2.105) and then define the residual as in [29]

$$\mathcal{R} = \frac{1}{p}\sqrt{\Delta T_{\mu\nu}\Delta T^{\mu\nu}}, \qquad \Delta T^{\mu\nu} = T^{\mu\nu} - T^{\mu\nu}_{\text{hydro}}. \tag{3.105}$$

This residual measures the difference between the hydrodynamic energy-momentum tensor and the one calculated using holography. As it was done in previous work [2, 28] we define the region where hydrodynamics is applicable by $\mathcal{R} < 15\%$. The result for symmetric and asymmetric shockwave collisions is shown in figure 3.13 for an example configuration. The profile of the boundary is well approximated by a hyperbola (blue, solid line) given by

$$\tau_* = \sqrt{(t - \Delta t)^2 - z^2} \tag{3.106}$$

[3]There exist regions were a real-valued eigenvector fails to exist, but this is outside of the hydrodynamic regime and hence not an issue in this analysis [51].

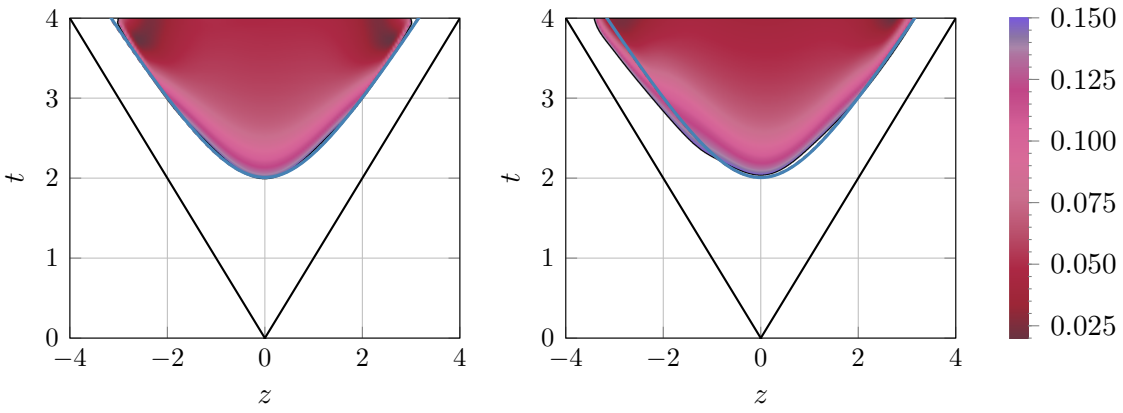

FIGURE 3.13: Spacetime region where the residual $\mathcal{R}$ (3.105) is less than 15%. The left panel shows the corresponding region for $\omega_\pm = 0.075$ while the right one displays $(\omega_+, \omega_-) = (0.1, 0.25)$. The blue line shows the hyperbola $(t - \Delta t)^2 - z^2 = \tau_*^2$ with $\Delta t = 0.5$ and $\tau_* = 1.5$ (cf. (3.106)). For both setups the hydrodynamization time is given by $t_{\text{hydro}} \approx 2$.

with $\Delta t = 0.5$ and $\tau_* = 1.5$. For symmetric shocks, this reproduces the results from [2, 28]. For asymmetric shocks, we can see that the influence of the asymmetry is of minor importance and hence the hydrodynamization time is still almost Lorentz-invariant.

As already mentioned in section 2.5 for a conformal fluid, hydrodynamics is fully encoded in the proper energy density ϵ and the corresponding fluid 4-velocity u^μ. To continue the analysis we first introduce proper time τ and rapidity ξ coordinates by

$$t = \tau \cosh \xi, \qquad z = \tau \sinh \xi. \tag{3.107}$$

Chesler, Kilbertus and van der Schee found in [2] that on a Cauchy surface with $\tau_{\text{init}} = 3.5$ the fluid 4-velocity is very well described by boost invariant flow, i.e.

$$u^\tau = 1, \qquad u^\xi = \vec{u}^\perp = 0. \tag{3.108}$$

We are able to confirm this behavior for symmetric shocks. This generalizes to asymmetric shocks where the violation of this condition is of order $\mathcal{O}(10^{-3})$. This is shown in figure 3.14 for different configurations of colliding shockwaves. Another key result of [2] is that the proper energy density is well described by a Gaussian

$$\epsilon(\omega, \tau) = A(\omega) e^{-\frac{1}{2}\frac{\xi^2}{\sigma(\omega)^2}} \tag{3.109}$$

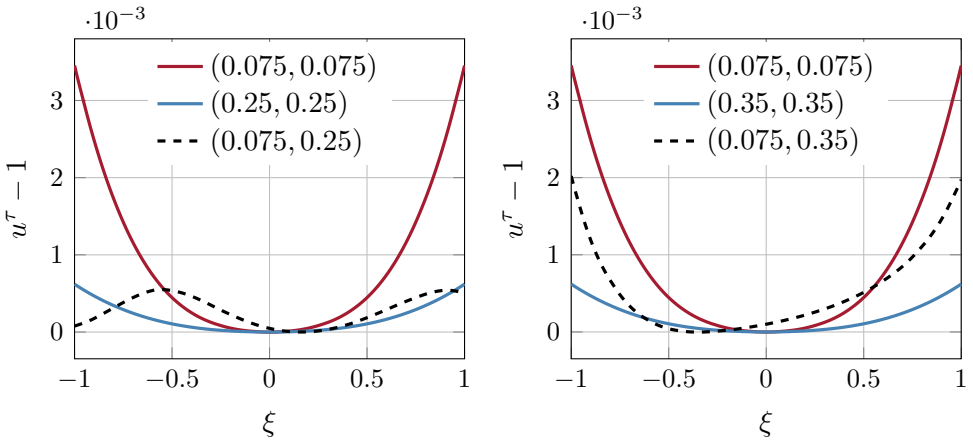

FIGURE 3.14: Violation of the boost invariant flow constraint, $u^\tau - 1$, at proper time $\tau = 2$ for two asymmetric shocks and the corresponding symmetric ones. In the left panel $(\omega_+, \omega_-) = (0.075, 0.25)$ is displayed while the right panel shows $(\omega_+, \omega_-) = (0.075, 0.35)$. As in [2] we find that the violation is just of order $\mathcal{O}(10^{-3})$.

where for $\tau_{\text{init}} = 3.5$ the amplitude and width of the function are given by [2]

$$A(\omega) \approx 0.14 + 0.15\omega - 0.025\omega^2, \tag{3.110a}$$

$$\sigma(\omega) \approx 0.96 - 0.49\omega + 0.13\omega^2. \tag{3.110b}$$

In figure 3.15 we also display the proper energy density for asymmetric shocks and find that they are again given by a Gaussian. This time they are not centered at vanishing rapidity ξ but they are shifted by $\bar{\xi}$. Hence, we write down the proper energy density as

$$\epsilon(\xi, \tau) = A(\omega_+, \omega_-; \tau) e^{-\frac{1}{2}\frac{(\xi - \bar{\xi}(\omega_+, \omega_-; \tau))^2}{\sigma(\omega_+, \omega_-; \tau)}}. \tag{3.111}$$

The shift for several configurations of asymmetric shockwave collisions is shown in figure 3.16. From this graph we can read off, that the shift is given by

$$\bar{\xi}(\omega_+, \omega_-; \tau) = \Xi(\tau) \, \frac{\omega_+ - \omega_-}{\omega_+ + \omega_-} \tag{3.112}$$

to a good approximation. As can be seen from figure 3.16 the coefficient Ξ is approximately 0.07 and ,thus, constant for $\tau > 2$. The rapidity distribution of the proper energy density is sufficiently well approximated by the shifted geometric mean of the corresponding symmetric collisions, i.e.

$$\begin{aligned} \epsilon(\xi, \tau; \omega_+, \omega_-) \approx \Big[& \epsilon(\xi - \bar{\xi}(\omega_+, \omega_-; \tau), \tau; \omega_+, \omega_+) \\ & \times \epsilon(\xi - \bar{\xi}(\omega_+, \omega_-; \tau), \tau; \omega_-, \omega_-) \Big]^{1/2}. \end{aligned} \tag{3.113}$$

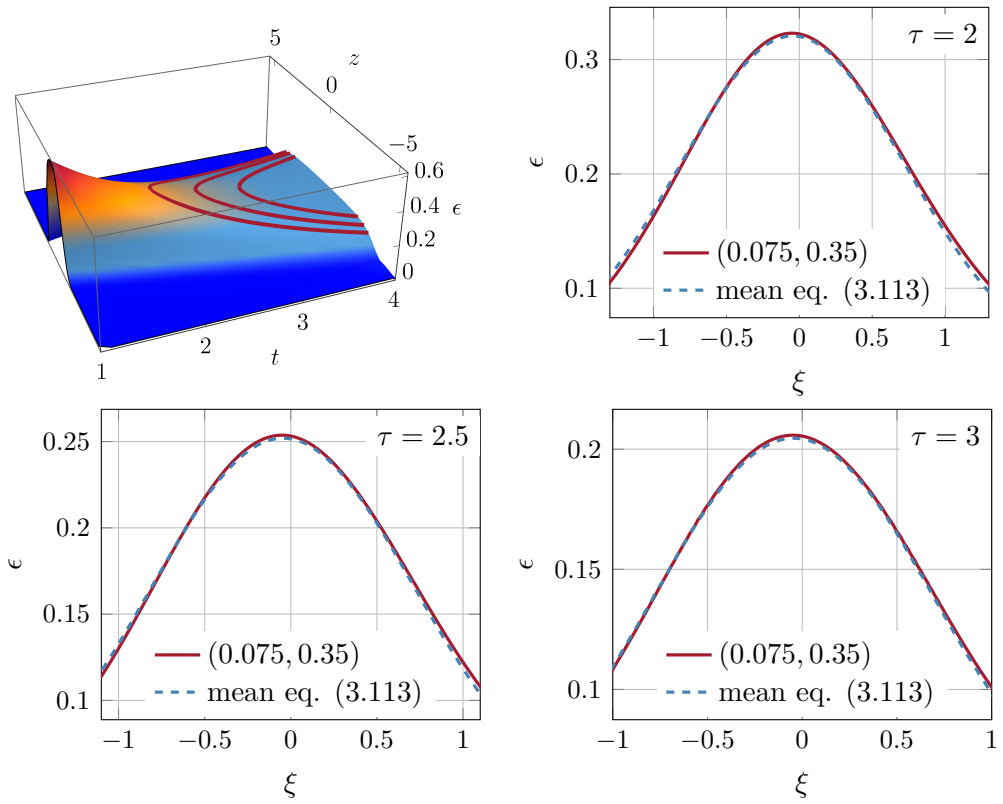

FIGURE 3.15: Proper energy density ϵ for shocks with $(\omega_+, \omega_-) = (0.075, 0.35)$. The top left panel displays this observable for all t and z, while the red lines correspond to lines parametrized by (3.107) for $\tau \in \{2, 2.5, 3\}$. The other panels display the energy density along these curves (red lines), while the blue dashed lines indicate the mean (3.113). We can see that for $|\xi| < 1$ this is a very good approximation, while for $|\xi| > 1$ slight deviations occur.

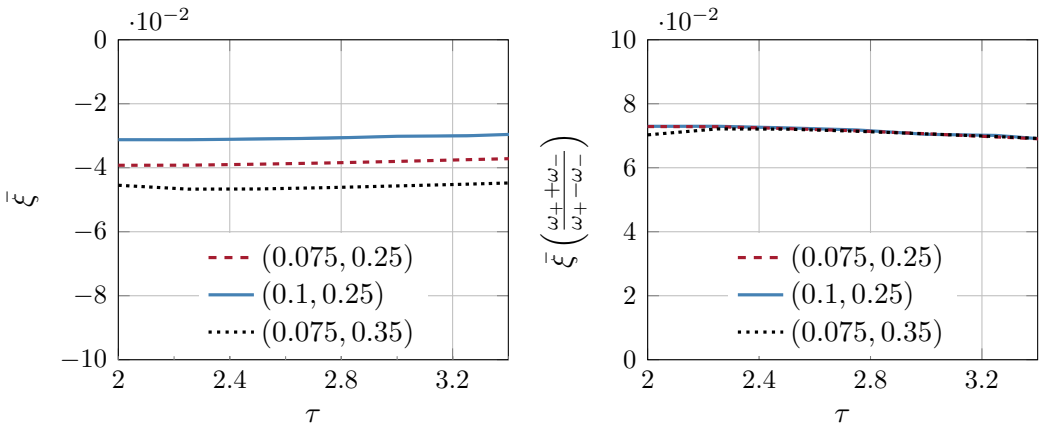

FIGURE 3.16: In these two plots we plot the τ dependence of the rapidity shift $\bar{\xi}$ from equation (3.112) for asymmetric collisions with $(\omega_+, \omega_-) = (0.075, 0.25)$ (dashed red), $(\omega_+, \omega_-) = (0.1, 0.25)$ (solid blue) and $(\omega_+, \omega_-) = (0.075, 0.35)$ (dotted black) in the left panel. In the right panel we plot the coefficient function $\Xi(\tau)$ which is almost constant for $\tau > 2$.

This approximation is displayed in figure 3.15. It works well for $|\xi| < 1$ while for $|\xi| > 1$ tiny deviations become visible. In [1] we suggest an improved model for the means of the proper energy densities.

3.6 Conclusion

This chapter and, hence, also [1] was first of all intended to give a pedagogical introduction to numerically solving Einstein's equations for planar shocks. This has to be seen as supplementing material to [28]. On the other hand, it is, of course, also motivated from a physical point of view. It is an attempt to close the gap between the very early stage of HICs and the hydrodynamic regime (QGP) by providing initial data for further hydrodynamic simulations which require the initial proper energy density for a conformal fluid.

In this chapter, we presented an extension of the "universal" flow for planar shocks [2]. This allows us to compute initial hydrodynamic data for off-center collisions provided that transverse gradients are small compared to longitudinal ones (cf. section 3.3). To access these data one can now simply use equation (3.113) and the result from [2] without performing any costly and numerically challenging simulations.

In [1] we verified the result from [2, 28] that the hydrodynamization time $t_{\text{hydro}} \approx 2$ and we find that this result also holds for asymmetric shockwaves. Considering the asymmetric shockwave collisions as pixels within an off-center collision (cf. figure 3.8), our results imply that hydrodynamization time, measured in the lab frame, increases towards the periphery of the overlap region that forms a QGP.

4

Entanglement Entropy

This chapter on entanglement entropy is based on the work which led to [3] and therefore the structure of this chapter follows this publication.
As mentioned in chapter 1, one of the motivations for this study was to probe the applicability of the holographic principle to QCD to some extent by considering an observable which can be calculated using both theories. The observable of interest is entanglement entropy which we will introduce in section 4.1.
Entanglement entropy has become a heavily studied field of research in recent years since it is widely applied in all kind of fields. For example, it is of great interest in quantum information theory, where many related entanglement measures, as e.g. mutual entropy, exist [52]. As we will show in section 4.2 there is also a relation to the holographic principle via minimal surfaces [53]. Entanglement entropy can also be used as a universal order parameter of quantum phase transitions for, e.g., $2+1$ dimensional topological field theories. This is done by relating entanglement entropy to the quantum dimension [54].
We start this chapter by defining entanglement entropy and Rényi entropies and showing some basic properties thereof in section 4.1. Afterwards, we review the holographic calculation of entanglement entropy in section 4.2 to get an idea of what we can expect from that point of view [55, 56]. We will compare these results with the ones obtained on the lattice later on.
In section 4.3 we will show how to calculate entanglement entropy (or to be more precise, Rényi entropies) on the lattice. This was already done for $SU(2)$ and

$SU(3)$ in earlier works [57, 58]. We follow this line of research to repeat the $SU(2)$ and $SU(3)$ calculations but with much higher statics and to present $SU(4)$ data for the first time [3]. We will also discuss the results with the holographic expectation in mind. Finally, we will conclude and give some possible future directions.

4.1 Entanglement and Rényi Entropy

In this section, we will define entanglement entropy and Rényi entropies as a generalization thereof and show some basic properties. This introduction is based on [59].

To obtain intuition on entanglement, we start with a simple example, namely a two-qubit system, i.e. two spin-1/2-particles where each of them can be in the state $|\uparrow\rangle$ or $|\downarrow\rangle$. It is straightforward to write down the Hilbert space and a basis thereof, since it is just the product space of the two individual particles,

$$\mathcal{H} = \mathcal{H}_{\text{qubit}} \otimes \mathcal{H}_{\text{qubit}} = \text{span}\left\{|\uparrow\uparrow\rangle, |\uparrow\downarrow\rangle, |\downarrow\uparrow\rangle, |\downarrow\downarrow\rangle\right\}. \tag{4.1}$$

It is obvious that these basis states are separable, i.e. if we measure the first qubit in any state, we do not know in which state the second qubit is. We call these states not-entangled. On the other hand, due to the quantum-nature of the system, we can consider states as the Einstein-Podolsky-Rosen (EPR) state [60] given by

$$\frac{1}{\sqrt{2}}\left(|\uparrow\downarrow\rangle + |\downarrow\uparrow\rangle\right) \tag{4.2}$$

which is clearly not separable. We call this state entangled because if we measure the first spin to be in any state, we immediately know the state in which the second particle is.

With this introductory example in mind, we want to formalize the idea of entanglement by considering a lattice of points labeled by α. On each of the lattice sites live degrees of freedom with a Hilbert space $\mathcal{H}_\alpha$. The total Hilbert space is then given by the product space as before, i.e.

$$\mathcal{H} = \otimes_\alpha \mathcal{H}_\alpha. \tag{4.3}$$

Next we bipartite the systems in two regions $\mathcal{A}$ and $\overline{\mathcal{A}}$ as is shown in the left panel of figure 4.1. The boundary $\partial\mathcal{A}$ is called entangling surface. For the lattice system, it is obvious that we can factorize the Hilbert space as

$$\mathcal{H} = \mathcal{H}_{\mathcal{A}} \otimes \mathcal{H}_{\overline{\mathcal{A}}}. \tag{4.4}$$

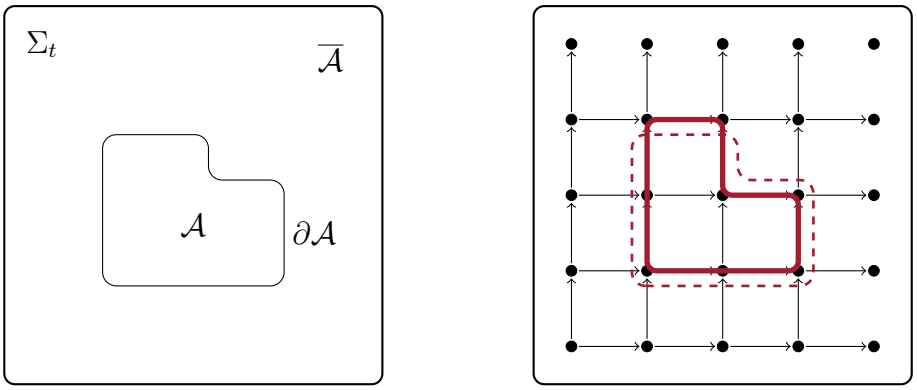

FIGURE 4.1: The left figure shows the bipartition of a fixed time slice Σ_t in regions $\mathcal{A}$ and $\overline{\mathcal{A}}$. The boundary between the two regions $\partial\mathcal{A}$ is called entangling surface. The right figure shows the maximally gauge invariant way of how to factorize the Hilbert space for a gauge theory [61]. The bipartition is chosen such that we cut along the links (solid line) because other possibilities (dashed line) would cut links and thus violate gauge invariance.

Afterwards, we can define the density matrix in the usual way, i.e. $\rho = |\psi\rangle\langle\psi|$. With this bipartition and factorization, we can construct an operator which acts only on one of the factors, e.g. $\mathcal{H}_{\mathcal{A}}$, by tracing out the complement ($\mathcal{H}_{\overline{\mathcal{A}}}$). This operator is called the reduced density matrix and can be written down formally as

$$\hat{\rho}_{\mathcal{A}} = \mathrm{tr}_{\overline{\mathcal{A}}}\left(\hat{\rho}\right) = \mathrm{tr}_{\overline{\mathcal{A}}}\left(|\psi\rangle\langle\psi|\right). \tag{4.5}$$

This definition can be interpreted as follows. We capture the state of degrees of freedom in $\mathcal{A}$ by complete ignorance of $\overline{\mathcal{A}}$. If the state $|\psi\rangle$ can be factorized, then we have a pure state in $\mathcal{H}_{\mathcal{A}}$. On the other hand due to quantum entanglement and the ignorance of $\mathcal{H}_{\overline{\mathcal{A}}}$, we can end up with a non-diagonal density matrix, i.e. a list of possibilities for various states $|\psi\rangle$ in $\mathcal{H}_{\mathcal{A}}$.
To quantify this operator we define entanglement entropy as the von-Neumann entropy of the reduced density matrix

$$S_{\mathrm{EE}} = -\mathrm{tr}_{\mathcal{A}}\left(\hat{\rho}_{\mathcal{A}}\log\left(\hat{\rho}_{\mathcal{A}}\right)\right). \tag{4.6}$$

This definition can be generalized to so-called Rényi entropies which are defined as the moments of the entanglement entropy [62, 63]

$$S^{(q)} = \frac{1}{1-q}\log\left(\mathrm{tr}_{\mathcal{A}}\left(\hat{\rho}_{\mathcal{A}}^{q}\right)\right) \quad \forall\ q \in \mathbb{N},\ q \geq 2. \tag{4.7}$$

These Rényi entropies are very useful to explore the purity of a state. Let us first recall that for a pure state the density matrix is just a projection operator

$\hat{\rho} = |\psi\rangle \langle\psi|$. Thus (with a proper normalization) $\mathrm{tr}\,(\hat{\rho}) = 1$, and due to the projection property $\mathrm{tr}\,(\hat{\rho}^2) = 1$ holds again. On the other hand for a mixed state, we expect that $\mathrm{tr}\,(\hat{\rho}^2) < 1$ and thus Rényi entropies provide a measure for quantum purity [59].

For most systems, as for the system we will consider, this definition can be analytically continued to $q \in \mathbb{R}_+$ and then one can show that

$$\lim_{q \to 1} S^{(q)} = S_{\mathrm{EE}}. \tag{4.8}$$

Up to now we only considered a field theory on a lattice. If we want to take the continuum $a \to 0$ limit the factorization of the Hilbert space (4.4) causes trouble for gauge theories. This is best seen by considering the lattice formulation of gauge theories, where the links are the gauge transporters and thus responsible for gauge invariance. As it can be seen from the right panel of figure 4.1, gauge invariance is lost if we cut any link. There are several possibilities to cope with this issue. One possibility is the so-called maximally gauge invariant way [61, 64], where one cuts along the links and then decides to which region the degree of freedom belongs to (cf. figure 4.1).

In section 4.3 we will consider a slab-shaped geometry with slab length l (cf. figure 4.4). We will use the limit (4.8) to approximate entanglement entropy. Calculating S_{EE} directly is hard in Monte Carlo simulations due to the logarithm, whereas $S^{(q)}$ is relatively cheap for $q \in \mathbb{N}, q \geq 2$.

Indeed, in the actual numerical calculation in section 4.3, we will approximate $S_{\mathrm{EE}} \approx S^{(2)}$.[1] This approximation can also be motivated by looking at the q dependence of the Rényi entropy in simplified models [67, 68] where free massive fields were considered. In these studies, the l-dependent terms in the Rényi entropy $S^{(q)}$ differ from corresponding terms in the entanglement entropy by a factor $\frac{q+1}{2q}$ (c.f,. equation (86) in [68]). For the second Rényi entropy $S^{(2)}$ this gives a factor of $\frac{3}{4}$. Higher Rényi entropies differ even more from entanglement entropy. On the other hand, the relative difference between $S^{(2)}$ and $S^{(3)}$ is around 10% which is the order of the numerical error in our simulations.

These considerations make it apparent that the gain of calculating higher Rényi entropies in order to improve the $q = 1$ extrapolation is overwhelmed by the numerical cost due to the mild dependence of $S^{(q)}$ on q for larger q. Hence, we have to accept a systematic error of at least 25% due to using second Rényi entropy instead of entanglement entropy itself.

Nevertheless, calculations in free field theories suggest that the functional depen-

[1] Studies of the impact of that approximation in [65] showed that for $SU(3)$ these errors are well below the statistical error. In the talk [66] a corresponding plot is shown on slide 38.

dence on l is the same for both entropies [67, 68].
It should be noted that the alternative formula used in [57, 58]

$$S_{\mathrm{EE}} = -\lim_{q\to 1} \frac{\partial}{\partial q} \log \mathrm{tr}\,(\hat{\rho}_{\mathcal{A}}^{q}) \tag{4.9}$$

gives the same result once the derivative is approximated using the finite difference formula $f'(q=1) = f(q=2) - f(q=1)$ on the lattice, i.e. one also measures $S^{(2)}$ precisely.
The Rényi and entanglement entropy contains non-universal UV-divergent terms that have to be removed carefully in order to access the low energy properties of the theory. This removing process has been most carefully worked out for finite and scalable entangled regions, such as the interior of a sphere [69]. For such regions, characterized by a single dimensionful size parameter l, the universal UV-finite contribution $C(l)$ to the entanglement entropy can be extracted as

$$C(l) = l\partial_l(l\partial_l S_{\mathrm{EE}}(l) - 2S_{\mathrm{EE}}(l)). \tag{4.10}$$

For a realistic lattice gauge theory on a square lattice, such spherical geometries are practically impossible, since the smooth surface could only be approximated by polygons with a lot of surface edges. These edges would result in a lot of additional contributions [70]. In the following, we will, therefore, restrict ourselves to a bipartition of the three dimensional time slice Σ_t into a slab of width l and its complement. This geometry of entangling region $\mathcal{A}$ was also considered in most previous simulations [55, 57, 58] and theoretical works [55, 68, 71]. Due to the periodic boundary conditions in spatial directions, the corresponding entangling surface consists of two parallel planes and thus has neither extrinsic curvature nor sharp corners. For such a slab-shaped entangling region with a large enough spatial extent L the entanglement entropy per unit area in $d = 3 + 1$ dimensions diverges as

$$S_{\mathrm{EE}}/L^2 = \frac{A'}{a^2} - \frac{C}{l^2} + (finite), \tag{4.11}$$

where a is the lattice spacing which sets the UV cutoff scale $\Lambda_{UV} \equiv a^{-1}$ and $(finite)$ denotes UV-finite terms which do not diverge as $a \to 0$ or $l \to 0$. For quantum field theories with a mass gap, at large l S_{EE} should approach a constant value. This result was derived in [55, 68, 71] by dimensional analysis and semi-analytic estimates.
The coefficient C in (4.11) is believed to be universal and similar to the A-function (in the terminology of [72–74]), a higher-dimensional generalization of central

charge of 2D CFTs which serves as a counter of the number of effective degrees of freedom in a theory. In particular, it is expected to decrease monotonically along the renormalization group flow, similarly to Zamolodchikov's c-function [75].
To extract C from the entanglement entropy (4.11), one can apply the differential operator $l^3\partial_l$ to the entanglement entropy

$$C(l) = \frac{l^3}{2\,L^2}\frac{\partial S_{\mathrm{EE}}(l)}{\partial l}. \tag{4.12}$$

At $l \sim a$, $C(l)$ counts the number of degrees of freedom at the UV cutoff scale (such as, e.g., asymptotically free gluons in QCD). However, at intermediate values of l, when finite terms in (4.11) become important, the coefficient $C(l)$ defined by (4.12) acquires a nontrivial l-dependence and can be interpreted as a counter of the number of degrees of freedom at scale l. By analogy with higher-dimensional generalizations of Zamolodchikov's c-theorem [72–74] one expects that $C(l)$ would monotonically decrease with l.
For slab-shaped entangled regions, such an interpretation has been confirmed by explicit calculations in free field theories [68, 71] and in holographic models [55]. In this thesis, we follow [55, 68, 71] and consider C as being approximately proportional to the effective number of degrees of freedom, referring to $C(l)$ as an entropic C-function [56–58]. We will see that our numerical results support such an interpretation.
Dimensional arguments suggest that at small slab width l the Rényi entropies (and in particular the second Rényi entropy, which we actually measure) should also behave similarly to (4.11), however, with coefficient C which is in general different from the one for the entanglement entropy. As discussed above, for free field theory the relative error in C is as large as 25% [68].
Let us note that a wealth of results exist for the scaling behavior of Rényi and entanglement entropies in lower, in particular 2D, gapless field theories. The general lesson to be drawn from these studies is to be careful with the naive C-function definition (4.11) and the usage of the second Rényi entropy as an approximation for the entanglement entropy. As mentioned before, the coefficient C may vary between the entanglement entropy and the second Rényi entropy in explicit examples (e.g. [76, 77]) and logarithmically diverging terms may occur (e.g. [78]). Additionally, so-called "unusual corrections" were found [79, 80], including oscillations in l. The necessity to go to large lattices sizes and large l to obtain a good match with CFT results was pointed out in [81]. In general, accurate results can only be expected when all of the above corrections are considered [82]. With this in mind, let us note that gapless lower-dimensional systems are very special and may or may not reflect the physics of four-dimensional YM theory with a finite

mass gap that we are considering in this thesis. Due to a lack of analytic results concerning the entanglement and Rényi entropies in this case, we are forced to simply test the prescription (4.12) with our numerical data. A qualitative analysis of the entanglement entropy for a slab-shaped region (see e.g. equation (4.5) in [71]) suggests that the term $-\frac{C}{l^2}$ in (4.11) might also contain an additional logarithmic factor:

$$S_{\mathrm{EE}}/L^2 = \frac{A'}{a^2} - \frac{C}{l^2} - \frac{C'}{l^2}\ln(l) + (finite). \tag{4.13}$$

In practice, however, it is difficult to extract a relatively small $\ln(l)$ correction to the l^{-2} scaling law. While one can construct a formal expression $C'(l) = l\frac{\partial}{\partial l}\left(\frac{l^3}{2L^2}\frac{\partial S_{\mathrm{EE}}(l)}{\partial l}\right)$ similar to (4.12) and (4.10) yielding the coefficient C' in (4.13), it yields a very noisy signal upon the replacement of a second derivative by finite differences, and is therefore not practical. We thus neglect possible $\ln(l)$ correction and use the expression (4.12) to extract the entropic C-function numerically. As already mentioned, the entropic C-function can be calculated both in holography and on the lattice. We will explain what we are expecting from a holographic point of view in the next section.

4.2 Holographic Entanglement Entropy

In this section, we will recapitulate the derivation of the holographic entropic C-function. The holographic principle was described in chapter 2 where we discussed that a strongly coupled problem in a CFT can be converted into a weakly coupled gravitational one.

Ryu and Takayanagi found a prescription for entanglement entropy using the gauge/gravity dictionary [83] and derived the formula [53]

$$S_{\mathrm{EE}}^{\mathrm{hol}} = \frac{A_{\mathrm{min}}}{4G_N\hbar} \quad \text{for } N_c \to \infty \text{ and } \lambda \text{ large.} \tag{4.14}$$

In this formula, A_{min} represents the minimal surface whose boundary coincides with the boundary of the entangling surface $\partial\mathcal{A}$. This was generalized to Rényi entropies in [84] where it has been argued that one has to replace the minimal surfaces by cosmic branes in AdS.

In the weak form of AdS/CFT, the field theory is conformal and does not show confinement which is an important feature of YM theories. One possibility to see confinement in a theory is to consider the Wilson loop $\mathcal{W}$ which is related to the quark-antiquark potential as $\langle\mathcal{W}\rangle \propto e^{-tV(r)}$ for infinite quark masses. For a

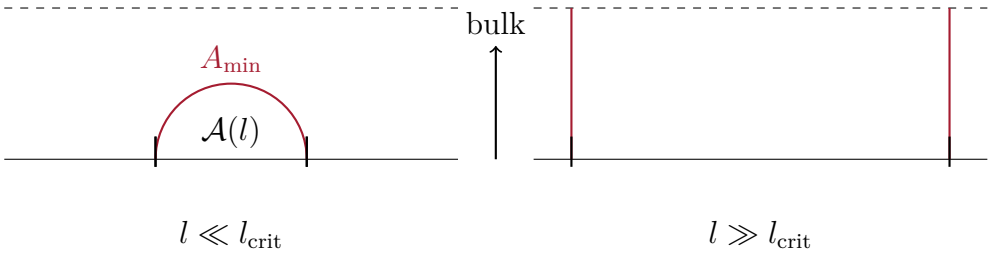

FIGURE 4.2: Entanglement entropy in a confining background. The geometry is deformed such that the Wilson loop satisfies an area law. In this figure, the black solid line represents the boundary which we bipartite in $\mathcal{A}(l)$ and $\overline{\mathcal{A}}$. The bipartition is parametrized by the length l. The confining background is depicted as the black dashed line which serves as a maximal penetration depth for geodesics. For $l \ll l_{\text{crit}}$ the minimal solution is a connected one while for $l \gg l_{\text{crit.}}$ the disconnected surface is minimal. It is straightforward to see that the connected solution depends on l while the disconnected one is l-independent, i.e. $\partial_l S_{\text{EE}} = 0$. Since these two solutions do not intersect smoothly, the derivative of S_{EE} has a jump as shown in figure 4.3.

confining theory as, e.g., QCD, the potential is of Cornell from, i.e.

$$V(r) = \frac{a}{r} + \sigma r. \tag{4.15}$$

The term proportional to r ensures confinement since for increasing distance the potential increases and at some point, enough energy is available that a new quark-antiquark pair is formed. This phenomenon is called (QCD) string breaking. Due to that fact, there are no free color charges below a critical temperature T_c. Therefore we see that for a confining theory the Wilson loop has to satisfy an area law.

On the other hand, the holographic dictionary tells us that the Wilson loop is given by $\langle \mathcal{W} \rangle = \exp(-S)$ where S is the action. In the 't Hooft limit, the action S simplifies to the NG action and thus we are left with the computation of a geodesic starting from the quark and ending at the anti-quark. Having this in mind and just considering pure AdS space, we see that due to the factor $\frac{1}{z^2}$ in the metric (2.77), increasing the distance between the quark and the antiquark at the boundary results in a geodesic penetrating deeper and deeper into the bulk. Thus the Wilson loop does not satisfy the required area law.

Therefore we modify the spacetime and introduce a finite penetration depth, as, e.g., a soft wall [85] or by an additional compactified dimension whose radius shrinks to zero at this depth as in the Witten model [21].[2]

[2]As it is mentioned in [55] for the hard wall model [86] this transition is not present since the disconnected solutions, which are essential for the behavior of entanglement entropy as we will see below, are not well defined.

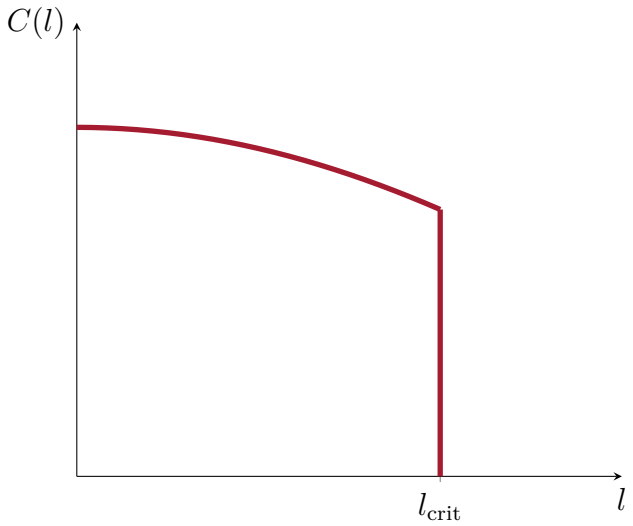

FIGURE 4.3: Expectation for the entropic C-function (4.12) from the holographic principle (figure adapted from [56]). It exhibits a jump at some critical length l_{crit} from a finite value to zero.

The basic idea is depicted in figure 4.2. It can be shown that there are always two solutions to the EoM for the minimal surface A_{min} in (4.14), a disconnected and a connected one [55]. Obviously, one always has to consider both of them and then take the minimum. The connected solution depends on the length l while the disconnected does not. Since the intersection of the connected and the disconnected solution is not smooth, the entropic C-function exhibits a jump at some critical value l_{crit}. At $l < l_{\text{crit}}$ the entropic C-function scales as N_c^2 (to the leading order in the $1/N_c$ expansion) while at $l > l_{\text{crit}}$ it is of order unity as it could be expected due to the confinement at large scales. These results were first published in [55, 56] and we show the corresponding plot in figure 4.3.
In the next section, we will show how we can calculate the entropic C-function on the lattice and we will also show results and discuss them.

4.3 Entanglement Entropy from the Lattice

In this section, we will describe how we can calculate Rényi entropy on the lattice. As already mentioned it is computationally hard to calculate entanglement entropy directly and thus we use the limit in (4.8) to approximate entanglement entropy. This has already been done for $SU(2)$ and $SU(3)$ pure YM theory in previous works [57, 58]. We extend this study by having larger statistics for these two gauge groups and for the first time doing calculations in $SU(4)$ pure YM theory.
By looking at the definition of Rényi entropies (4.7) we see that we have to calculate powers of the reduced density matrix $\text{tr}_{\mathcal{A}}\left(\hat{\rho}_{\mathcal{A}}^q\right)$. In [67] a strategy to tackle

this problem using the path integral formalism was proposed. We will review this method in a graphical way adapted to the lattice. To get familiar to this graphical notation we start by calculating matrix elements of the density matrix $\hat{\rho}$ which we can write as

$$\langle\psi_1|\,\hat{\rho}\,|\psi_2\rangle = \frac{1}{Z}\,\langle\psi_1|\,e^{-\beta\hat{H}}\,|\psi_2\rangle =$$

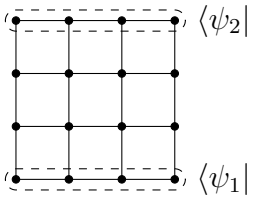

. (4.16)

In this work, we always refer to the density matrix of the groundstate, i.e. $\hat{\rho} = |0\rangle\langle 0|$, which we obtain in the limit $\beta \to \infty$. The picture in the formula has to be understood as follows. We have to integrate over all field configurations from Euclidean time $\tau_E = -\infty$ to $\tau_E = \infty$ with $\left|\psi_{1/2}\right\rangle$ as boundary conditions. Obviously, this integral is infinite dimensional, but in the lattice approach it is discretized to give a finite (but very large) dimensional integral, which is then evaluated using Monte Carlo techniques.
Having introduced this graphical visualization we can calculate matrix elements of the reduced density matrix by tracing over region $\overline{\mathcal{A}}$, i.e.

$$\langle\psi_1|\,\hat{\rho}_{\mathcal{A}}\,|\psi_2\rangle = \sum_{\langle\psi|}$$

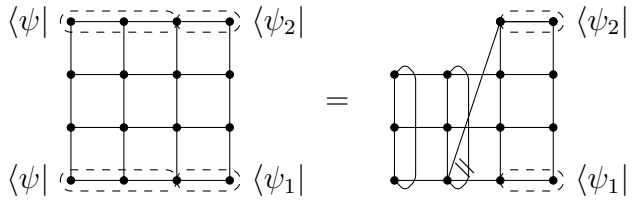

. (4.17)

In the last step, we deformed the lattice such that we automatically get rid of the sum by identifying corresponding states $|\psi\rangle$. It is important to note that the same number of degrees of freedom label a regular lattice and a deformed lattice. In particular, the diagonal link in the deformed lattice carries the same group element as the middle lower link (as indicated by the equal sign). This feature will later allow computing the derivative in the holographic C-function by comparing different cut lengths l obtained from the same underlying lattice configurations. Furthermore this also has the technical advantage, that we can use standard methods to store the lattice data in memory. After these considerations, we can compute powers of the reduced density matrix by gluing copies of reduced density matrix lattices together. This holds true because we can insert a unity operator

$$\langle\psi_1|\,\hat{\rho}_{\mathcal{A}}^2\,|\psi_2\rangle = \sum_{\langle\psi|}\langle\psi_1|\,\hat{\rho}_{\mathcal{A}}\,|\psi\rangle\,\langle\psi|\,\hat{\rho}_{\mathcal{A}}\,|\psi_2\rangle \tag{4.18}$$

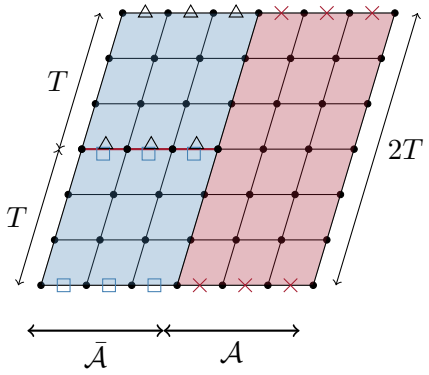

FIGURE 4.4: Visualization of the deformed geometry as it was already shown in [58]. The periodicity in region $\mathcal{A}$ (right, red) is $2T$ while in $\overline{\mathcal{A}}$ (left,blue) we have two copies with periodicity T. The crosses, squares and triangles indicate the identifications which have to be made.

and then replace the sum by an identification as before. Taking the trace over $\mathcal{A}$ afterwards results in the identification of the corresponding open states $\langle\psi_1|$ and $|\psi_2\rangle$, i.e.

$$\mathrm{tr}_{\mathcal{A}}\left(\hat{\rho}_{\mathcal{A}}^2\right) = \tag{4.19}$$

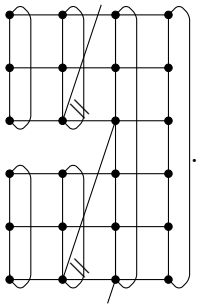

This easily generalizes to arbitrary powers q of the reduced density matrix as

$$\mathrm{tr}_{\mathcal{A}}\left(\hat{\rho}_{\mathcal{A}}^q\right) = \frac{Z[\mathcal{A}, q, T]}{Z^q[T]} \tag{4.20}$$

where $Z[T]$ is the partition function of a normal lattice and the partition function $Z[\mathcal{A}, q, T]$ refers to a lattice which has a temporal period of $q \times T$ in $\mathcal{A}$ and there are q subsystems with period T in $\bar{\mathcal{A}}$. We show an alternative graphical way, which was also used in [58], to depict this geometry in figure 4.4.
Using (4.7) and (4.20) we can write the Rényi entropies as

$$S^{(q)} = \frac{1}{q-1} F[\mathcal{A}, q, T] - \frac{q}{q-1} F[T] \tag{4.21}$$

where we used the relation $F = -\log Z$ between the free energy F and the partition function Z. As already mentioned we will approximate the entanglement entropy by the second Rényi entropy. Our aim is to calculate the entropic C-function and therefore we have to calculate the derivative with respect to l. We

approximate this by using the central finite difference approximation for $q = 2$

$$\frac{\partial}{\partial l} S_{EE}(l - a/2) \approx \frac{F[l - a, 2, T] - F[l, 2, T]}{a}. \tag{4.22}$$

The term $\sim F[T]$ in (4.21) vanishes since it does not depend on l. At this point, we see that for the first Rényi entropy there is no cut and hence the derivative of the first Rényi entropy will always vanish. Therefore, the best we can do with this method is to calculate the second Rényi entropy.

So far we have achieved to rewrite the problem of calculating the entropic C-function to measuring differences of free energies on the deformed lattice geometry defined above. Calculating such differences was first developed in [87, 88] and we will briefly review the method in what follows.

Assuming we want to calculate the difference of two arbitrary free energies F_1 and F_2, we can first use the relation between the free energy and the partition function $F_i = -\log(Z_i)$ again and then use the Fundamental Theorem of Calculus, i.e.

$$F_2 - F_1 = -\log Z_2 + \log Z_1 = -\int_0^1 d\alpha \frac{\partial}{\partial \alpha} \log Z(\alpha) \tag{4.23}$$

where the equality in the last step obviously only holds if $Z(1) = Z_2$ and $Z(0) = Z_1$. The simplest partition function satisfying these requirements is given by a linear interpolation

$$Z(\alpha) = \int D[U] \exp\left(-(1-\alpha)S_1[U] - \alpha S_2[U]\right) \tag{4.24}$$

where $\int D[U]$ refers to the path integral over all gauge links U. Then we can analytically calculate the derivative with respect to α to arrive at

$$F_2 - F_1 = \int_0^1 d\alpha \left\langle S_2[U] - S_1[U] \right\rangle_\alpha \tag{4.25}$$

where $\langle \cdot \rangle_\alpha$ denotes the average with weight of the interpolating partition function $Z(\alpha)$ defined above.

With this procedure, we can finally calculate the entropic C-function by the following steps:

Step 1 Generate gauge configurations with interpolating action

$$S_{\text{int}} = (1-\alpha)S_l[U] + \alpha S_{l+1}[U] \tag{4.26}$$

on the deformed lattice (see figure 4.4). The subscripts l and $l+1$ refer to the length of the cut.

Step 2 Measure $S_{l+1} - S_l$ on these configurations for several values of α.

Step 3 Integrate over α by using cubic spline interpolation and then analytically integrate the interpolation. Other numerical methods turn out to give the same results within statistics.

Step 4 Calculate the entropic C-function using the formula

$$C(l - a/2) = \frac{(l - a/2)^3}{aL^2} \int_0^1 d\alpha \, \langle S_{l+1} - S_l \rangle_\alpha \, . \tag{4.27}$$

4.4 Numerical Results

In the previous section, we have reviewed how to calculate entanglement entropy or to be more precise Rényi entropies, on the lattice. In this section, we will first discuss the details of our lattice calculation and afterwards, we are going to present results for the entropic C-function in $SU(2)$, $SU(3)$ and $SU(4)$ pure YM theory. To implement the method described in the last section we use the standard Wilson action given by

$$S[U] = \frac{\beta}{N_c} \sum_{U_{\mu\nu}} \text{Re tr} \, (1 - U_{\mu\nu}) \, . \tag{4.28}$$

We are using a pseudo-heatbath algorithm to update the gauge configurations. Doing this we have to calculate the closing plaquettes for the link which we want to update. It is crucial in this step that we carefully choose the nearest neighbors of the lattice sites, since there are several points at the end of the cut which are non-trivial to reach.

To generate random $SU(N_c)$ matrices we use the Cabbibo-Marinari algorithm [89], where one updates all $SU(2)$ subgroups of the $SU(N_c)$ matrix one after another. To avoid autocorrelation we wait 100 sweeps between successive measurements and we also checked the autocorrelation time. For all sets of parameters, we use a lattice of size $N_s^3 \times (q \times N_t) = 16^3 \times (2 \times 16)$. Since the resolution of the entropic C-function in l would be very poor if we only considered one single β value we have to set the scale on the lattice to be able to compare several different lattice spacings. We do this by using the string tension $\sqrt{\sigma}$ determined in [90] and then measure everything in units of $\sqrt{\sigma}$.

The number of configurations for $SU(2)$, $SU(3)$ and $SU(4)$ pure YM theory are given in table 4.1. The numbers in these tables are the configurations we gathered for each α value.

As mentioned in the last section (cf. equation (4.27)) we have to integrate the interpolating action over α. Therefore we have to study the convergence of the

Configurations for SU(2)

β	$a\sqrt{\sigma}$ \ l	2	3	4	5	6	7
2.420	0.245		414,720	414,720	1,708,280	1,437,288	1,432,656
2.440	0.228			276,480	1,928,208	1,808,640	1,763,604
2.450	0.220	172,800	1,013,760	1,642,921	2,582,780	2,583,793	2,561,809
2.460	0.213			276,480	1,840,128	1,826,752	1,750,272
2.500	0.184	172,800	172,800	449,280	829,440	1,720,584	1,723,629

Configurations for SU(3)

β	$a\sqrt{\sigma}$ \ l	2	3	4	5	6	7
5.700	0.391	44,976	44,976	130,656	253,056	218,328	230,568
5.720	0.374			34,728			
5.740	0.357			34,728			
5.750	0.350	34,728	34,728	34,728	120,408	208,080	134,640
5.770	0.335			34,728			
5.780	0.328			34,728			
5.800	0.314	34,728	34,728	34,728	120,408	255,048	134,640

Configurations for SU(4)

β	$a\sqrt{\sigma}$ \ l	2	3	4	5	6	7
11.000	0.215	24,480	70,560	93,600	93,600	69,120	184,320
11.004	0.214						57,600
11.008	0.214						30,744
11.058	0.203		26,650				
11.075	0.200					160,221	115,200
11.100	0.195				253,440	253,440	253,440
11.112	0.193					30,744	
11.156	0.186						57,600
11.192	0.180				33,961		
11.200	0.179		103,680	103,680	149,760	357,120	357,120
11.300	0.164		11,520	11,520	126,720	126,720	264,960
11.398	0.152			31,704			

TABLE 4.1: $SU(2)$, $SU(3)$ and $SU(4)$ configurations for the used β values and cut lengths l. The numbers are the configurations simulated for each value of α. To get the total number of configurations one has to multiply the $SU(2)$ and $SU(3)$ configurations by 11 and the $SU(4)$ ones by 21.

N_c	c	$\chi^2/_{d.o.f.}$
2	0.054(1)	0.24
3	0.173(5)	1.14
4	0.417(6)	0.44

TABLE 4.2: Fit to a constant and corresponding $\chi^2/_{d.o.f.}$ for the first few data points in figure 4.5.

integral value with respect to the number of discretization points carefully. As in [58] we find that we need 11 interpolating points for $SU(3)$ but we need 21 for $SU(4)$. For $SU(2)$ we also use 11 interpolating points instead of the 6 which were used in [57]. The increased number of α values can be explained by the larger lattice volume and the, therefore, larger integrand compared to [57]. Besides the increased computational cost due to larger color matrices, this gives an additional factor of ~ 2 in computation time. Which makes it computationally almost impossible to go to really larger N_c with present-day computational resources.
The entropic C-function which we obtain from the lattice simulations are shown in figure 4.5. In these plots, the different markers and colors correspond to different lattice couplings β.
We see that for sufficiently small values of l the entropic C-function is constant within statistical errors for $N_c = 2, 3, 4$. This behavior can be expected since entropy is saturated by weakly interacting massless gluons in the short-distance asymptotic freedom regime and the entropic C-function is defined such that it is constant for non-interacting conformal fields. To get access to these constants we fit a constant to the first data points where $l\sqrt{\sigma}$ is less than $l_{max} = 1.1$, 1.3 and 0.7 for $SU(2)$, $SU(3)$ and $SU(4)$ respectively. To verify these results we also varied the fit range and found only a mild dependence. We also summarize the fit results in table 4.2.
Above l_{max} the data for $SU(2)$ and $SU(N_c \neq 2)$ are qualitatively different and will, therefore, be discussed separately.
Let us start with $SU(2)$ data. We find that above l_{max} there is no clear trend, but remarkably the data for $a\sqrt{\sigma} = 0.220$ (red data points in figure 4.5) show the expected transition at $l\sqrt{\sigma} \gtrsim 1$. We have two different explanations in mind.
First of all these effects might well be lattice artifacts. In the lattice approach, one discretizes continuous spacetime by some finite lattice with a lattice spacing a and therefore one automatically picks up discretization errors (from the non-zero lattice spacing a) and finite volume effects (from the finite physical volume $(qTa)(La)^3$). To get reliable results one has to be sure that both errors are under control. It is known that the finite volume effects are only suppressed by a power law in $SU(2)$ gauge theory, while they are suppressed exponentially for $SU(N_c > 2)$. There-

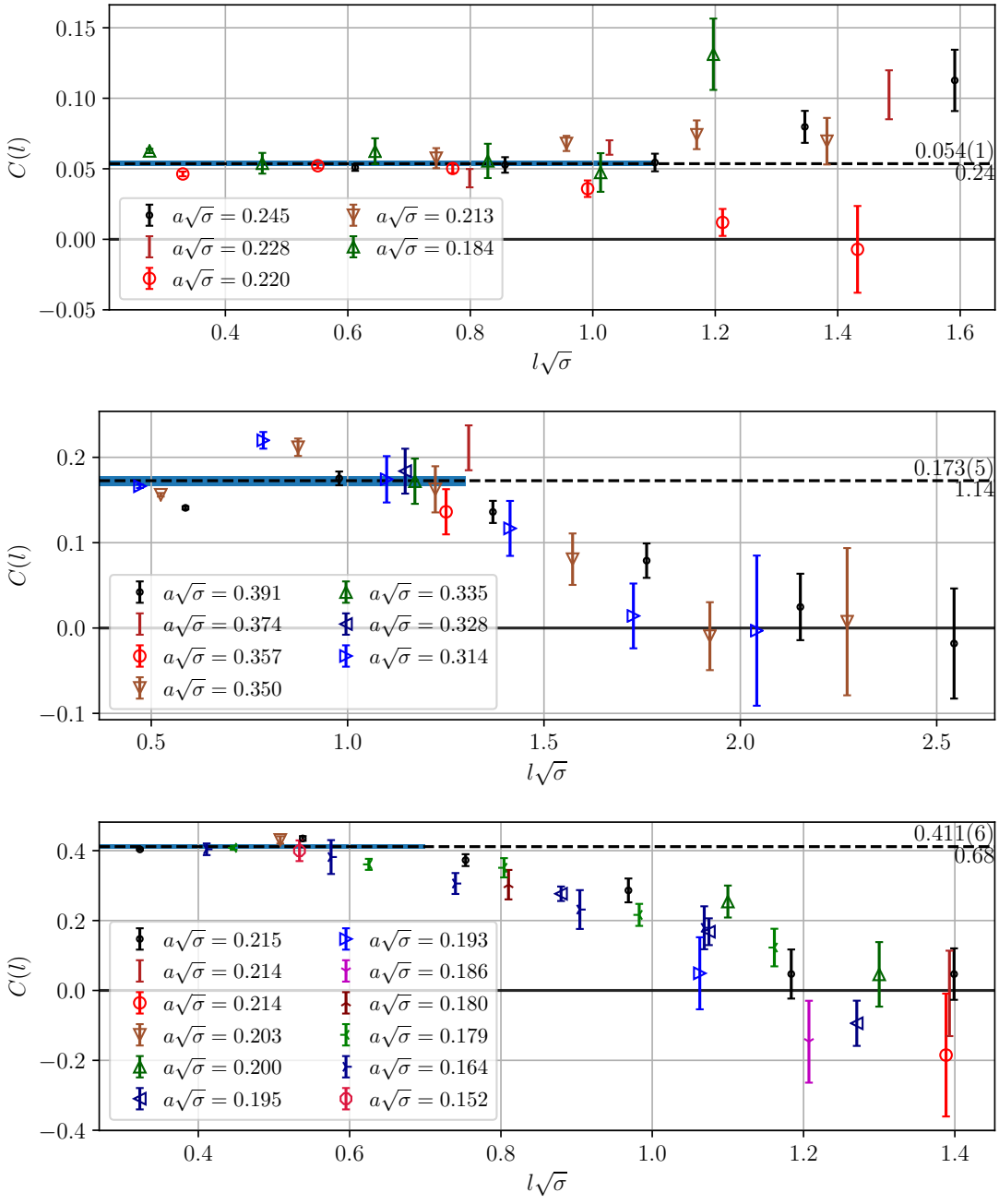

FIGURE 4.5: Entropic C-functions for $SU(2)$, $SU(3)$ and $SU(4)$ (from top to bottom) lattice gauge theories. The black dashed line with the blue error band is a fit to a constant for the first data points where $l\sqrt{\sigma}$ is less than 1.1, 1.3 and 0.7 for $SU(2)$, $SU(3)$ and $SU(4)$ respectively. The numerical value with error is given on the very right of each plot. The value below gives the $\chi^2/_{d.o.f.}$ for this fit.

fore larger finite volume effects are expected for $SU(2)$ YM theories. This is also supported by the fact, that with our lattice size, $(2 \times 16 \times 16^3)$, we are already at half of the critical temperature for $a\sqrt{\sigma} \approx 0.18$ [91, 92]. On the other hand, if we go to larger $a\sqrt{\sigma}$ to get a larger physical volume, we suffer from discretization effects. Therefore for the chosen lattice size, we only have a small window around $a\sqrt{\sigma} \approx 0.22$ where we have both effects under control. We emphasize that this discussion is only qualitative so far and the lattice artifacts have to be studied with more care on larger lattices. Due to the limited computational resources, this was not feasible within this work.

Beside these lattice artifacts, this difference might also originate in the different order of finite-temperature deconfinement phase transition in $SU(2)$ (second-order) and $SU(N_c > 2)$ (first-order) gauge theories. It is reasonable to conjecture that the behavior near the critical cut length l_{max} might be related to thermal entropy close to the finite-temperature phase transition since both transitions look qualitatively similar for theories with a Hagedorn-type spectrum of states [55]. Therefore we can expect an enhancement of entanglement entropy and its fluctuations in the vicinity of the second-order thermal phase transition in $SU(2)$ gauge theory due to the divergence of the correlation length [93]. This is absent for first-order phase transitions in $SU(N_c > 2)$ gauge theories.

For the $SU(N_c \neq 2)$ case, we find an expected monotonic decrease (within statistical errors) of the entropic C-function for $l > l_{max}$. It reaches a value which is compatible with zero. We have seen in section 4.2 that we expect a discontinuous transition from the holographic computation [55], while we observe a smooth transition. Nevertheless, this behavior can be expected for a finite lattice and finite N_c.

Additionally, holography makes several assumptions which do not hold true in the YM theory considered here, and thus it is also not very puzzling that we get not exactly the same results. The parameter which we did vary here was the number of colors N_c, which is assumed to be ∞ in the holographic prediction. Therefore we want to compare the different gauge groups. In the short l regime, the theory is fairly well described by free gluons which have $N_c^2 - 1$ degrees of freedom and thus we rescale the entropic C-function by this number. The resulting graph is shown in figure 4.6. In this plot, we only distinguish between different gauge groups and do not display the lattice spacings. Obviously, the $SU(2)$ data is still qualitatively different and thus we will leave them out from the discussion from now on. We can see that the $SU(3)$ and $SU(4)$ data are shifted but besides that, they have a similar shape. Since we finally want to see if the number of colors has a visible influence of the validity of the gauge/gravity prediction, i.e. that the slope for

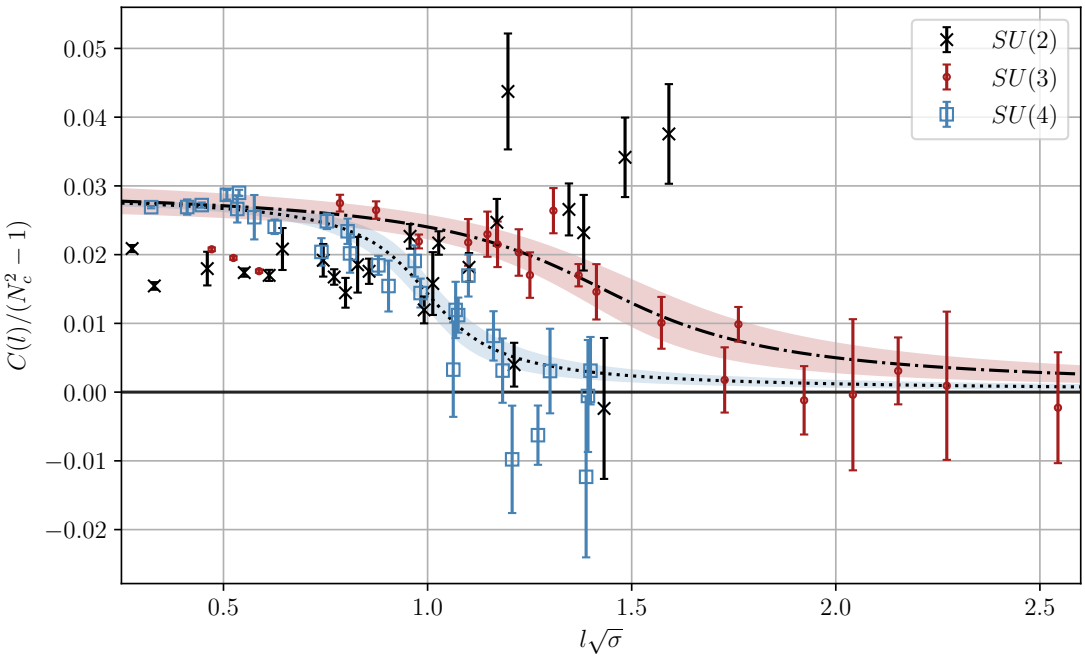

FIGURE 4.6: The entropic C-function for $SU(2)$, $SU(3)$ and $SU(4)$ rescaled by the gluon degrees of freedom $N_c^2 - 1$. The fits to these data are according to a regularized step function (4.29). The first three red points ($SU(3)$) were excluded from the fit due to large discretization errors, but these points show a trend towards the fit in the continuum limit.

large N_c becomes steeper we fit the data to a regularized step function given by

$$A\left[\frac{1}{2} + \frac{1}{\pi}\arctan\left(\frac{x-C}{B}\right)\right]. \tag{4.29}$$

The resulting fit with error bands is visualized in figure 4.6 by the black lines and the fit parameters are given by

N_c	A	B	C
3	0.030 ± 0.003	-0.328 ± 0.112	1.422 ± 0.068
4	0.029 ± 0.001	-0.132 ± 0.044	0.997 ± 0.029

From these results, we can calculate the maximal slope $m_{\max} = \frac{A}{B\pi}$ which gives

$$m_{\max}^{SU(3)} = -0.030 \pm 0.013, \tag{4.30}$$
$$m_{\max}^{SU(4)} = -0.070 \pm 0.025. \tag{4.31}$$

Due to limited statistics, the errors are quite large and thus it is hard to give a definite conclusion, but we observe a trend towards a steeper slope for $N_c = 4$. This is consistent with the scenario of a discontinuous transition in the large N_c limit.

4.5 Discussion

In this chapter, we have calculated the entropic C-function corresponding to second Rényi entropy $S^{(2)}$ as an approximation for entanglement entropy as a function of the width l of the slab-like entangled region in pure $SU(N_c)$ YM theory for $N_c = 2, 3, 4$ using lattice methods.

We have shown that the UV-finite entropic C-function is proportional to the number of gluon states $(N_c^2 - 1)$ for short distances. At larger values of l, this quantity is consistent with zero, which is in agreement with the absence of colorful states in the low-energy confinement regime. We also found an indication that this transition is steeper for $N_c = 4$ than for $N_c = 3$ which would support the holographic prediction of a jump in the $N_c \to \infty$ limit [55]. Let us note that for finite N_c a phase transition on a finite lattice cannot be discontinuous. Thus, there are two possible scenarios of how to interpret this. One possibility is, that the entropic C-function undergoes a discontinuous transition for any N_c, but this can only be seen by working on sufficiently larger lattices and taking the proper infinite volume limit. Another possibility is, that the discontinuity occurs only in the $N_c \to \infty$ limit, since the predictions of [55] based on the holographic principle and a Hagedorn-type spectrum are strictly speaking only valid in this limit.

Obviously, the facts that the holographic principle assumes SUSY, large 't Hooft coupling λ, and so one also may be responsible for these differences. Also, the fact that [55] calculates the entropic C-function of entanglement entropy and we calculated the one related to the second Rényi entropy might be an explanation for this difference.

Possible future projects can involve both sides. First of all in the lattice approach, one would like to increase statistics further to decrease the error bars. Going to larger N_c may reveal a steeper slope and thus a more abrupt transition. But as already mentioned this results in large computational cost, not only due to the obvious N_c dependence but also due to the finer lattice of α-values for the integrand. For $N_c = 3, 4$ this already resulted in an additional factor of 2^{N_c} in computational cost. Hence, it is questionable if this is feasible in the near future.

On the other hand, the holographic calculations can also be brought closer to the lattice simulations by considering corrections due to finite 't Hooft coupling. Also, the result of [84] using Rényi instead of entanglement entropy in the holographic setup is interesting and might be closer to the results which we observed numerically.

5

Summary and Conclusion

In this thesis, we used AdS/CFT which we reviewed in chapter 2 to be able to map strongly coupled problems in a CFT to weakly coupled gravity, i.e. Einstein gravity.

In chapter 3 we used this duality to collide lumps of energy in a CFT which can be translated to solving classical Einstein's equations in asymptotically AdS space-time. This collision in the CFT can be seen as an approximation for the early stage of a HIC and the formation of the QGP which is an almost perfect fluid. We chose the latter property as a benchmark of how fast the two incoming projectiles are well described by hydrodynamics after the collision. We used infinitely extended shocks in the transverse directions which reduced the dimension of the problem and hence, resulted in less numerical instabilities and lower computational costs. We argued in section 3.3 that this can be seen as the first-order in a gradient expansion for off-center collisions (cf. figure 3.8). In [2] Chesler, Kilbertus and van der Schee found an expression for the post-collision proper energy density. This is needed as initial data for hydrodynamic simulations which are much less cumbersome than going through the whole holographic numerics. We were able to generalize this result to asymmetric shocks by using appropriate averages of symmetric collisions (cf. equation (3.113)). This helps a lot in the understanding of the early phase of HIC since there are not really any other tools to study this sector, because in this regime QCD is strongly coupled and thus PT fails. On the other hand, this is also a dynamical, out-of-equilibrium process which cannot be

analyzed with the most common tool, i.e. LQCD. Hence, the AdS/CFT approach is very promising, even though it assumes a supersymmetric, infinitely strongly coupled CFT with an infinite number of colors.
Additionally, confinement is not present in this formulation of AdS/CFT which can be seen from the quark anti-quark potential since it does not satisfy an area law as we sketched in section 4.2. But there are other models, like the already mentioned Witten model [21] which include confinement. Hence, it would be interesting to perform calculations in this model, which uses the AdS_6/CFT_5 duality and then wraps up one coordinate to break parts of the CFT SUSY. But to continue the numerical studies in that direction a lot of pioneering work has to be redone for the D4-brane setup in type IIA superstring theory. E.g., one would have to redo the calculation from [94] for the relation between the near boundary metric of AdS spacetime and the energy-momentum tensor in the boundary CFT for type IIA string theory. Overcoming these difficulties would be very interesting because then one could also observe the confinement-deconfinement phase transition in these model HICs.
As already mentioned there are other differences between the CFT side and QCD. In chapter 4 we studied entanglement entropy which can be calculated both using holography and for pure YM theory. Thus we can probe the dependence of this observable on the number of colors N_c at least to some extent. We used a slab-shaped geometry for which the holographic calculation predicts a jump of the entropic C-function (4.12) at some finite size of the slab (cf. figure 4.2). This computation uses the Ryu-Takayangi formula (4.14) derived in [53]. We calculated the entropic C-function corresponding to the second Rényi entropy on the lattice for $SU(N_c)$, $N_c \in \{2, 3, 4\}$. We found a smooth transition instead of a jump which can be expected for a finite lattice. To make a very precise statement one would have to consider the proper infinite volume limit. Assuming that also in the infinite volume limit we still do not find a jump but a smooth transition, we also found that the slope of this transition is larger for $N_c = 4$ than for $N_c = 3$ which supports the holographic prediction in the $N_c \to \infty$ limit. As can be seen from table 4.1 this was a high-statistics study and hence computationally quite costly. Therefore, going to larger lattices (to study the infinite volume limit) or to go to larger N_c (to test if the slope increases further) are out of scope in the near future. A very promising idea from the holographic side was proposed in [84] which gives formulas for calculating Rényi entropies which bring the holographic setup closer to the scenario considered in this work.
To sum up, the AdS/CFT duality is a tool to study the early phase of HICs even though differences between supersymmetric CFT and QCD are significant. Nevertheless, there are ways to lower the differences between these theories, e.g.

the Witten model [21] or the Sakai-Sugimoto model [95, 96]. This will enlarge the spectrum of observables which are universal enough to give similar results for holographic models and strongly coupled, dynamical QCD processes.
The applicability of AdS/CFT to QCD can be estimated by having a look at observables in both theories, as we did for entanglement entropy. Further investigations in this direction could strengthen this approach.

A

Explicit equations for Planar Shocks

A.1 Einstein's Equations for Planar Shocks

In this section, we write down explicit forms for Einstein's equations (3.64a)-(3.64g) for planar shocks. We parametrize the spatial metric $\hat{g}$ as

$$\hat{g} = \begin{pmatrix} e^{B} & 0 & 0 \\ 0 & e^{B} & 0 \\ 0 & 0 & e^{-2B} \end{pmatrix}, \tag{A.1}$$

with an anisotropy function $B(u,t,z)$ and $u = 1/r$. For the case of planar shocks where we do not have a transverse (x,y) dependence, the functions F_x and F_y can also be set to zero. From now on we name the F_z component F for brevity. With

these simplifications Einstein's equations in EF coordinates read

$$\Big(\partial_r^2 + Q_\Sigma[B]\Big)\,\Sigma = 0\,, \tag{A.2a}$$

$$\Big(\partial_r^2 + P_F[B,\Sigma]\partial_r + Q_F[B,\Sigma]\Big)\,F = S_F[B,\Sigma]\,, \tag{A.2b}$$

$$\Big(\partial_r + Q_{d_+\Sigma}[\Sigma]\Big)\,d_+\Sigma = S_{d_+\Sigma}[B,\Sigma,F]\,, \tag{A.2c}$$

$$\Big(\partial_r + Q_{d_+B}[B,\Sigma]\Big)\,d_+B = S_{d_+B}[B,\Sigma,F,d_+\Sigma]\,, \tag{A.2d}$$

$$\partial_r^2 A = S_A[B,\Sigma,F,d_+\Sigma,d_+B]\,, \tag{A.2e}$$

$$\Big(\partial_r + Q_{d_+F}[B,\Sigma]\Big)\,d_+F = S_{d_+F}[B,\Sigma,F,d_+\Sigma,d_+B,A]\,, \tag{A.2f}$$

$$d_+\,(d_+\Sigma) = S_{d_+^2\Sigma}[B,\Sigma,F,d_+\Sigma,d_+B,A]\,. \tag{A.2g}$$

Now we write down the source terms whereby we omit the dependencies in the square brackets.

$$Q_\Sigma = \tfrac{1}{2}B'^2\,, \tag{A.3a}$$

$$P_F = 2B' + \Sigma'\,\Sigma^{-1}\,, \tag{A.3b}$$

$$Q_F = 2B'' + (6B'\,\Sigma' + 4\Sigma'')\,\Sigma^{-1} + 3B'^2 - 4\Sigma'^2\,\Sigma^{-2}\,, \tag{A.3c}$$

$$S_F = 2B'_{,z} + (4\Sigma'_{,z} + 6B'\,\Sigma_{,z})\,\Sigma^{-1} + 3B_{,z}\,B' - 4\Sigma'\,\Sigma_{,z}\,\Sigma^{-2}\,, \tag{A.3d}$$

$$Q_{d_+\Sigma} = 2\Sigma'\,\Sigma^{-1}\,, \tag{A.3e}$$

$$\begin{aligned} S_{d_+\Sigma} = {} & -2\Sigma + \frac{e^{2B}}{12\Sigma^3}\Big\{8\Sigma\Big[F\Big(2\Sigma'_{,z} + F'\,\Sigma'\Big) + F^2\,\Sigma'' + F_{,z}\,\Sigma' + \Sigma_{,zz}\Big] \\ & + 2\Sigma\,(F\,\Sigma' + \Sigma_{,z})\Big(8(F\,B' + B_{,z}) + F'\Big) - 4\Big(F\Sigma' + \Sigma_{,z}\Big)^2 \\ & + \Sigma^2\Big[2F\Big(4B'_{,z} + B'\,(7B_{,z} + 4F') + F''\Big) + 2F'_{,z} + 4B'F_{,z} \\ & \quad + F^2\Big(4B'' + 7B'^2\Big) + 4B_{,z}F' + 7B_{,z}^2 + 4B_{,zz} + F'^2\Big]\Big\}\,, \end{aligned} \tag{A.3f}$$

$$Q_{d_+B} = \tfrac{3}{2}\Sigma'\,\Sigma^{-1}\,, \tag{A.3g}$$

$$\begin{aligned} S_{d_+B} = {} & \tfrac{3}{2}B'\,d_+\Sigma\,\Sigma^{-1} - \frac{e^{2B}}{6\Sigma^4}\Big\{\Sigma^2\Big(2F'_{,z} + B'F_{,z} + B_{,z}F' + B_{,z}^2 + B_{,zz} + F'^2\Big) \\ & + F\Big[\Sigma(4\Sigma'_{,z} + B'\,\Sigma_{,z} + B_{,z}\,\Sigma' - 2F'\,\Sigma') + 2\Sigma^2\Big(B'_{,z} + B'(B_{,z} + F') + F''\Big) \\ & - 8\Sigma'\Sigma_{,z}\Big] + F^2\Big[\Sigma\Big(B'\Sigma' + 2\Sigma''\Big) + \Sigma^2\Big(B'' + B'^2\Big) - 4\Sigma'^2\Big] \\ & + \Sigma\Big(B_z\Sigma_{,z} - 4F'\Sigma_{,z} + 2F_{,z}\Sigma' + 2\Sigma_{,zz}\Big) - 4\Sigma_{,z}^2\Big\}\,, \end{aligned} \tag{A.3h}$$

$$\begin{aligned} S_A = {} & +\tfrac{3}{2}d_+B\,B' - 6d_+\Sigma\,\Sigma'\,\Sigma^{-2} + 2 + \frac{e^{2B}}{4\Sigma^4}\Big\{ - 8\Sigma\Big[F(\Sigma'_{,z} + F'\,\Sigma' + F\Sigma'') \\ & + F\Sigma'_{,z} + F_{,z}\,\Sigma' + \Sigma_{,zz} + 2(F\,B' + B_{,z})(F\,\Sigma' + \Sigma_{,z})\Big] + 4\Big(F\Sigma' + \Sigma_{,z}\Big)^2 \end{aligned}$$

$$+\Sigma^2\Big[-7(F\,B'+B_{,z})^2+F'^2-4\Big(F\Big(2B'_{,z}+B'\,F'\Big)+F^2\,B''+B'\,F_{,z}+B_{,zz}\Big)\Big]\Big\}\,, \tag{A.3i}$$

$$Q_{d_+F}=2B'-2\Sigma'\,\Sigma^{-1}\,, \tag{A.3j}$$

$$\begin{aligned}S_{d_+F}=&-2(A'_{,z}+F\,A''+A'\,F')-2(B'-\Sigma'\,\Sigma^{-1})(FA'+A_{,z})+A'F'\\&-3d_+B\Big[F\,B'+B_{,z}+2(F\Sigma'+\Sigma_{,z})\,\Sigma^{-1}\Big]-2\Big(F\,(d_+B)'+(d_+B)_{,z}\Big)\\&+d_+\Sigma\,\Big(3\Sigma F'+4(F\Sigma'+\Sigma_{,z})\Big)\,\Sigma^{-2}-4\Big(F\,(d_+\Sigma)'+(d_+\Sigma)_{,z}\Big)\,\Sigma^{-1}\,,\end{aligned} \tag{A.3k}$$

$$\begin{aligned}S_{d_+^2\Sigma}=&-\frac{e^{2B}}{3\Sigma^2}\Big\{\Sigma\Big[FA'_{,z}+F\Big(A'_{,z}+FA''+A'F'\Big)+2\Big(FA'+A_{,z}\Big)\Big(FB'+B_{,z}\Big)\\&+A'\,F_{,z}+A_{,zz}-2d_+F\,(F\,B'+B_{,z})-(d_+F)_{,z}-F(d_+F)'\Big]\\&+\Big(F\Sigma'+\Sigma_{,z}\Big)\Big(FA'+A_{,z}-d_+F\Big)\Big\}-A'\,d_+\Sigma+\tfrac{1}{2}\Sigma\,d_+B^2\,.\end{aligned} \tag{A.3l}$$

Here primes denote radial derivatives, $f'\equiv\partial f/\partial r$, while $f_{,z}\equiv\partial f/\partial z$, etc. The conditions for the horizon at a fixed radial position (3.73) can be written down as

$$d_+\Sigma\Big|_{r=r_h}=-\frac{e^{2B}}{3}\Big(-\frac{F^2}{2\Sigma_{,z}^3}+\frac{F_{,z}}{\Sigma}+\frac{F}{\Sigma^2}(2\Sigma B_{,z}+\Sigma_{,z})\Big)\Big|_{r=r_h}\,. \tag{A.4}$$

The stationary horizon equation derived from (3.74) can be written as

$$\begin{aligned}0=&\,A_{,zz}+A_{,z}\left[-F'-2F\left(B'-\frac{\Sigma'}{\Sigma}\right)+2B_{,z}+\frac{\Sigma_{,z}}{\Sigma}\right]\\&+\tfrac{1}{4}A\left\{F'^2-2F'_{,z}-2F'\left(2B_{,z}+\frac{\Sigma_{,z}}{\Sigma}\right)-4F_{,z}\left(B'-3\frac{\Sigma'}{\Sigma}\right)+F^2\left[\left(B'-\frac{4\Sigma'}{\Sigma}\right)^2-\frac{6\Sigma''}{\Sigma}\right]\right.\\&\quad+4FF'\left(B'-\frac{\Sigma'}{\Sigma}\right)-4F\left(B'_{,z}+2B'B_{,z}-6B_{,z}\frac{\Sigma'}{\Sigma}+B'\,\frac{\Sigma_{,z}}{\Sigma}-\frac{\Sigma'_{,z}}{\Sigma}-2\frac{\Sigma_{,z}\Sigma'}{\Sigma^2}\right)\\&\quad\left.+4B_{,zz}+7(B_{,z})^2+16B_{,z}\frac{\Sigma_{,z}}{\Sigma}+\frac{8\Sigma_{,zz}}{\Sigma}-\frac{4(\Sigma_{,z})^2}{\Sigma^2}+24\,e^{-2B}\left(\Sigma'\,d_+\Sigma-\Sigma^2\right)\right\}\\&+F_{,z}\left(2d_+B-\frac{d_+\Sigma}{\Sigma}\right)-\tfrac{3}{2}F^2\left(d_+B\,B'-\frac{(d_+\Sigma)'}{\Sigma}+4-\frac{2d_+\Sigma}{\Sigma}\left(B'+\frac{\Sigma'}{\Sigma}\right)\right)\\&-F\left(\frac{3(d_+\Sigma)_{,z}}{\Sigma}+d_+B\left(B_{,z}-\frac{4\Sigma_{,z}}{\Sigma}\right)-\frac{d_+\Sigma}{\Sigma}\left(3F'-2B_{,z}+\frac{2\Sigma_{,z}}{\Sigma}\right)\right)\\&+\frac{e^{2B}}{4\Sigma^2}\left\{-6\,(d_+B)^2\,\Sigma^4+F^4\left(B'+\frac{2\Sigma'}{\Sigma}\right)^2+2F^3\left(B'+\frac{2\Sigma'}{\Sigma}\right)\left(2F'+B_{,z}+\frac{2\Sigma_{,z}}{\Sigma}\right)\right.\\&\quad\left.+F^2\left(F'^2+4B_{,z}\,F'+(B_{,z})^2+(2F'+B_{,z})\frac{4\Sigma_{,z}}{\Sigma}+\frac{4(\Sigma_{,z})^2}{\Sigma^2}\right)\right\}.\end{aligned} \tag{A.5}$$

A.2 Equations for the Transformation from FG to EF

In this section, we derive the equations for the coordinate transformation from FG to EF coordinates.
We start with the metric for a shock moving in $+\tilde{z}$ direction in FG coordinates which is given by

$$ds^2_{FG} = \tilde{\rho}^{-2}\left(-d\tilde{t}^{\,2} + d\tilde{\mathbf{x}}^2_\perp + d\tilde{z}^2 + d\tilde{\rho}^2\right) + \tilde{\rho}^2 h(\tilde{x}_-) d\tilde{x}^2_+. \tag{A.6}$$

for an arbitrary shock function $h(\tilde{x}_+)$ and $\tilde{x}_- \equiv \tilde{t} - \tilde{z}$. The desired form in EF coordinates with inverted radial coordinate ($r \equiv 1/u$) is given by

$$ds^2_{EF} = -2dt\left[\frac{1}{u^2}du + Adt + Fdz\right] + \Sigma^2 \hat{g}_{ij} dx^i dx^j. \tag{A.7}$$

From this, we can read off that the fixed metric coefficients are

$$g^{EF}_{uu} = 0, \quad g^{EF}_{uz} = 0, \quad g^{EF}_{ut} = -\frac{1}{u^2}. \tag{A.8}$$

We parametrize the FG coordinates according to

$$\begin{aligned} \tilde{t} &= t + u + \alpha(t-z,u), \quad \tilde{\mathbf{x}}_\perp = \mathbf{x}_\perp, \\ \tilde{z} &= z - \gamma(t-z,u), \quad \tilde{\rho} = u + \beta(t-z,u). \end{aligned} \tag{A.9}$$

Calculating the transformation of the FG metric to EF coordinates, i.e.

$$g^{EF}_{AB} = \frac{\partial \tilde{x}^C}{\partial x^A}\frac{\partial \tilde{x}^D}{\partial x^B} g^{FG}_{CD} \tag{A.10}$$

and using the fixed coefficients (A.8) we arrive at the following equations

$$\begin{aligned} g^{EF}_{uu} : 0 = &-\alpha'(\alpha'+2) + \beta'(\beta'+2) + \gamma'^2 \\ &+ H(\beta+u)^4(\alpha'+\gamma'+1)^2, \qquad \text{(A.11a)} \\ g^{EF}_{uz} : 0 = &\, H(\beta+u)^4(\alpha'+\gamma'+1)(\alpha_{,z}+\gamma_{,z}-1) - (\alpha'+1)\alpha_{,z} \\ &+ (\beta'+1)\beta_{,z} - \gamma'(-\gamma_{,z}+1), \qquad \text{(A.11b)} \\ g^{EF}_{ut} + g^{EF}_{uz} : 0 = &\, \gamma'(2\gamma_{,z}+1) + \beta^2/u^2 + 2\beta/u - \alpha' - \gamma', \qquad \text{(A.11c)} \end{aligned}$$

where the prime $'$ denotes radial derivatives, the subscript z denotes derivatives in z direction and $H \equiv h(t+u-z+\alpha+\gamma)$. The dependence of α, β and γ on $(t-z,u)$ is suppressed for brevity.

Following [28] it is helpful to redefine α and β such that

$$\alpha = -\gamma + \beta + \delta, \quad \beta = -\frac{u^2\zeta}{1+u\zeta}. \tag{A.12}$$

Inserting this in equations (A.11) and taking appropriate linear combinations we can decouple one of the three differential equations, while the other two remain coupled. The equations read

$$\frac{\partial\delta}{\partial u} - \frac{u^2}{(1+u\zeta)^2}\frac{\partial\zeta}{\partial u} = 0\,, \quad \frac{1}{u^2}\left(u^2\frac{\partial\zeta}{\partial u}\right) + \frac{2uH}{(1+u\zeta)^{5)}} = 0\,, \tag{A.13}$$

and

$$\frac{\partial\gamma}{\partial u} - \frac{u^2}{(1+u\zeta)^2}\frac{\partial\zeta}{\partial u} + \frac{u^4}{2(1+u\zeta)^2}\left(\frac{\partial\zeta}{\partial u}\right)^2 + \frac{u^4 H}{2(1+u\zeta)^6} = 0\,. \tag{A.14}$$

Alternatively, it is easy to see that curves along the radial direction in EF coordinates (A.7) satisfy the geodesic equation. Since coordinate transformations are isometries the same curves written down in FG coordinates have to satisfy the geodesic equation, i.e.

$$\frac{d^2\tilde{Y}^A}{dr^2} + \tilde{\Gamma}^A_{BC}\frac{d\tilde{Y}^B}{dr}\frac{d\tilde{Y}^C}{dr} = 0 \tag{A.15}$$

where $\tilde{\Gamma}$ are the Christoffel symbols evaluated in FG coordinates. Parameterizing the coordinate transformation again by (A.9) we arrive at three non-trivial equations, i.e.

$$\begin{aligned}\alpha'' = &-\frac{2\,(\alpha'+1)}{u} + \frac{2(\alpha'+1)(\beta'+1)}{\beta+u} \\ &+ \tfrac{1}{2}\Big[H'(\beta+u)^4(\alpha'+\gamma'+1)^2 + 8H(\beta'+1)(\beta+u)^3(\alpha'+\gamma'+1)\Big],\end{aligned} \tag{A.16a}$$

$$\begin{aligned}\gamma'' = -\gamma'\,\frac{2(\beta-u\beta')}{(u(\beta+u))} - \tfrac{1}{2}\Big[&H'(\beta+u)^4\,(\alpha'+\gamma'+1)^2 \\ &+ 8H(\beta'+1)(\beta+u)^3(\alpha'+\gamma'+1)\Big],\end{aligned} \tag{A.16b}$$

$$\begin{aligned}\beta'' = -\frac{2}{u}\,\beta' - \frac{2}{u} + \frac{1}{\beta}\Big[&H(\beta+u)^4(\alpha'+\gamma'+1)^2 + (\alpha'(\alpha'+2) \\ &+ \beta'^2 - \gamma'^2 - u\beta'')\Big].\end{aligned} \tag{A.16c}$$

It is possible to solve any of these sets of equations leading to the same initial data.

A.3 Near Boundary Expansions

The coefficients $\{a_i\}_i$ of the near boundary expansion (3.89b) of $\tilde{\alpha}$ are given by

$$a_0 = \frac{2\sqrt{\frac{2}{\pi}}e^{-\frac{z^2}{2w^2}}}{15w}, \tag{A.17a}$$

$$a_1 = \frac{11ze^{-\frac{z^2}{2w^2}}}{60\sqrt{2\pi}w^3}, \tag{A.17b}$$

$$a_2 = \frac{37ze^{-\frac{z^2}{2w^2}}(z^2-3w^2)}{2016\sqrt{2\pi}w^7}, \tag{A.17c}$$

$$a_3 = \frac{e^{-\frac{z^2}{w^2}}(768w^7+23\sqrt{2\pi}e^{\frac{z^2}{2w^2}}(3w^4-6w^2z^2+z^4))}{12096\pi w^9}, \tag{A.17d}$$

$$a_4 = \frac{ze^{-\frac{z^2}{w^2}}(1896w^7+7\sqrt{2\pi}e^{\frac{z^2}{2w^2}}(15w^4-10w^2z^2+z^4))}{21600\pi w^{11}}, \tag{A.17e}$$

$$a_5 = \frac{e^{-\frac{z^2}{w^2}}(-48456w^9+89736w^7z^2-67\sqrt{2\pi}e^{\frac{z^2}{2w^2}}(15w^6-45w^4z^2+15w^2z^4-z^6))}{1425600\pi w^{13}}. \tag{A.17f}$$

The coefficients $\{b_i\}_i$ of the near boundary expansion (3.89a) of $\tilde{\beta}$ are given by

$$b_0 = -\frac{e^{-\frac{z^2}{2w^2}}}{6\sqrt{2\pi}w}, \tag{A.18a}$$

$$b_1 = -\frac{ze^{-\frac{z^2}{2w^2}}}{10\sqrt{2\pi}w^3}, \tag{A.18b}$$

$$b_2 = \frac{e^{-\frac{z^2}{2w^2}}(w^2-z^2)}{30\sqrt{2\pi}w^5}, \tag{A.18c}$$

$$b_3 = \frac{ze^{-\frac{z^2}{2w^2}}(3w^2-z^2)}{126\sqrt{2\pi}w^7}, \tag{A.18d}$$

$$b_4 = \frac{e^{-\frac{z^2}{w^2}}(-116w^7-3\sqrt{2\pi}e^{\frac{z^2}{2w^2}}(3w^4-6w^2z^2+z^4))}{4032\pi w^9}, \tag{A.18e}$$

$$b_5 = -\frac{ze^{-\frac{z^2}{w^2}}(312w^7+\sqrt{2\pi}e^{\frac{z^2}{2w^2}}(15w^4-10w^2z^2+z^4))}{8640\pi w^{11}}. \tag{A.18f}$$

The coefficients $\{g_i\}_i$ of the near boundary expansion (3.89c) of $\tilde{\gamma}$ are given by

$$g_0 = -\frac{e^{-\frac{z^2}{2w^2}}}{5\sqrt{2\pi}w}, \tag{A.19a}$$

$$g_1 = -\frac{3ze^{-\frac{z^2}{2w^2}}}{20\sqrt{2\pi}w^3}, \tag{A.19b}$$

$$g_2 = \frac{5e^{-\frac{z^2}{2w^2}}(w^2 - z^2)}{84\sqrt{2\pi}w^5}, \tag{A.19c}$$

$$g_3 = -\frac{11ze^{-\frac{z^2}{2w^2}}(z^2 - 3w^2)}{672\sqrt{2\pi}w^7}, \tag{A.19d}$$

$$g_4 = \frac{e^{-\frac{z^2}{w^2}}(-32w^7 - \sqrt{2\pi}e^{\frac{z^2}{2w^2}}(3w^4 - 6w^2z^2 + z^4))}{576\pi w^9}, \tag{A.19e}$$

$$g_5 = -\frac{ze^{-\frac{z^2}{w^2}}(3408w^7 + 13\sqrt{2\pi}e^{\frac{z^2}{2w^2}}(15w^4 - 10w^2z^2 + z^4))}{43200\pi w^{11}}. \tag{A.19f}$$

List of Figures

List of Tables

Acronyms

AdS Anti-de-Sitter

CFT Conformal Field Theory

CM Center-of-Momentum

DBI Dirac-Born-Infeld

EF Eddington-Finkelstein

EoM Equations of Motion

EPR Einstein-Podolsky-Rosen

FEM Finite Element Method

FG Fefferman-Graham

GR General Relativity

GSO Gliozzi, Scherk and Olive

HIC Heavy Ion Collision

LHC Large Hadron Collider

LQCD Lattice QCD

NG Nambu-Goto

NS Neveu-Schwarz

ODE Ordinary Differential Equation

PT Perturbation Theory

QED Quantum Electro Dynamics

QCD Quantum Chromo Dynamics

QGP Quark Gluon Plasma

R Ramond

RHIC Relativistic Heavy Ion Collider

RK Runge-Kutta

SM Standard Model

SUGRA Supergravity

SUSY Supersymmetry

SYM Super Yang-Mills

YM Yang-Mills

Bibliography

[1] S. Waeber, A. Rabenstein, A. Schäfer, and L. G. Yaffe, "Asymmetric shockwave collisions in AdS_5", [1906.05086].

[2] P. M. Chesler, N. Kilbertus, and W. van der Schee, "Universal hydrodynamic flow in holographic planar shock collisions", [1507.02548].

[3] A. Rabenstein, N. Bodendorfer, P. Buividovich, and A. Schäfer, "Lattice study of Rényi entanglement entropy in $SU(N_c)$ lattice Yang-Mills theory with $N_c = 2, 3, 4$", [1812.04279].

[4] S. Bethke, "The 2009 World Average of α_s", [0908.1135].

[5] K. G. Wilson, "Confinement of quarks", *Physical Review D* **10** (1974) 2445–2459.

[6] J. M. Maldacena, "The Large N Limit of Superconformal Field Theories and Supergravity", [hep-th/9711200].

[7] S. S. Gubser, I. R. Klebanov, and A. A. Tseytlin, "Coupling Constant Dependence in the Thermodynamics of N=4 Supersymmetric Yang-Mills Theory", [hep-th/9805156].

[8] A. Buchel, J. T. Liu, and A. O. Starinets, "Coupling constant dependence of the shear viscosity in N=4 supersymmetric Yang-Mills theory", [hep-th/0406264].

[9] A. Buchel, "Resolving disagreement for eta/s in a CFT plasma at finite coupling", [0805.2683].

[10] B. Hassanain and M. Schvellinger, "Diagnostics of plasma photoemission at strong coupling", [1110.0526].

[11] D.-L. Yang and B. Müller, "Shear Viscosities of Photons in Strongly Coupled Plasmas", [1507.04232].

[12] S. Grozdanov and A. O. Starinets, "On the universal identity in second order hydrodynamics", [1412.5685].

[13] D. Steineder, S. A. Stricker, and A. Vuorinen, "Thermalization at intermediate coupling", [1209.0291].

[14] S. A. Stricker, "Holographic thermalization in N=4 Super Yang-Mills theory at finite coupling", [1307.2736].

[15] D. Steineder, S. A. Stricker, and A. Vuorinen, "Probing the pattern of holographic thermalization with photons", [1304.3404].

[16] S. Waeber, A. Schäfer, A. Vuorinen, and L. G. Yaffe, "Finite coupling corrections to holographic predictions for hot QCD", [1509.02983].

[17] M. Ammon and J. Erdmenger, *Gauge/Gravity Duality*, vol. 57. Cambridge University Press, Cambridge, 2015.

[18] D. Tong, "Lectures on String Theory", [0908.0333].

[19] M. Ammon, "Gauge/gravity duality applied to condensed matter systems", *Fortschritte der Physik* **58** (2010) 1123–1250.

[20] G. Hooft, "A planar diagram theory for strong interactions", *Nuclear Physics B* **72** (1974) 461–473.

[21] E. Witten, "Anti-de Sitter Space, Thermal Phase Transition, And Confinement In Gauge Theories", *Advances in Theoretical and Mathematical Physics* **2** (1998) 253–291, [hep-th/9803131].

[22] E. Witten, "Anti De Sitter Space And Holography", [hep-th/9802150].

[23] S. S. Gubser, I. R. Klebanov, and A. M. Polyakov, "Gauge Theory Correlators from Non-Critical String Theory", [hep-th/9802109].

[24] P. Kovtun, "Lectures on hydrodynamic fluctuations in relativistic theories", [1205.5040].

[25] C. Eckart, "The Thermodynamics of Irreversible Processes. III. Relativistic Theory of the Simple Fluid", *Physical Review* **58** (1940) 919–924.

[26] P. Romatschke, "Relativistic Hydrodynamic Attractors with Broken Symmetries: Non-Conformal and Non-Homogeneous", [1710.03234].

[27] L. D. Landau and J. M. Lifschitz, *Fluid Mechanics*. Elsevier, 1987.

[28] P. M. Chesler and L. G. Yaffe, "Numerical solution of gravitational dynamics in asymptotically anti-de Sitter spacetimes", [1309.1439].

[29] P. M. Chesler and L. G. Yaffe, "Holography and off-center collisions of localized shock waves", [1501.04644].

[30] W. van der Schee, *Gravitational collisions and the quark-gluon plasma.* PhD thesis, Utrecht University, 2014.

[31] P. Kovtun, D. T. Son, and A. O. Starinets, "Viscosity in Strongly Interacting Quantum Field Theories from Black Hole Physics", [hep-th/0405231].

[32] G. Policastro, D. T. Son, and A. O. Starinets, "Shear viscosity of strongly coupled N=4 supersymmetric Yang-Mills plasma", [hep-th/0104066].

[33] P. M. Chesler and L. G. Yaffe, "Boost invariant flow, black hole formation, and far-from-equilibrium dynamics in N = 4 supersymmetric Yang-Mills theory", [0906.4426].

[34] P. M. Chesler and L. G. Yaffe, "Holography and colliding gravitational shock waves in asymptotically AdS_5 spacetime", [1011.3562].

[35] H. Bondi, "Gravitational Waves in General Relativity", *Nature* **186** (1960) 535–535.

[36] R. Sachs, "Gravitational waves in general relativity VIII. Waves in asymptotically flat space-time", *Proceedings of the Royal Society of London. Series A. Mathematical and Physical Sciences* **270** (1962) 103–126.

[37] P. M. Chesler and L. G. Yaffe, "Horizon formation and far-from-equilibrium isotropization in supersymmetric Yang-Mills plasma", [0812.2053].

[38] H. Wang, "Study of Particle Ratio Fluctuations and Charge Balance Functions at RHIC", [1304.2073].

[39] G. Philips and P. Taylor, *Theory and Applications of Numerical Analysis.* Elsevier, 1996.

[40] K. Weierstrass, "Über die analytische Darstellbarkeit sogenannter willkürlicher Functionen reeller Argumente", in *Mathematische Werke* (J. Knoblauch, ed.), pp. 1–38. Cambridge University Press, Cambridge, 1885.

[41] V. Cardoso, L. Gualtieri, C. Herdeiro, and U. Sperhake, "Exploring New Physics Frontiers Through Numerical Relativity", *Living Reviews in Relativity* **18** (2015) 1.

[42] J. P. Boyd, *Chebyshev and Fourier Spectral Methods (Revised)*. Dover Publications, 2001.

[43] F. N. van de Vosse and P. D. Minev, *Spectral Element Methods: Theory and Applications/ F.N. Van de Vosse and P.D. Minev*. EUT report. Eindhoven University of Technology, Faculty of Mechanical Engineering, 1996.

[44] R. Arnowitt, S. Deser, and C. W. Misner, "The Dynamics of General Relativity", [gr-qc/0405109].

[45] T. Mädler and J. Winicour, "Bondi-Sachs Formalism", [1609.01731].

[46] S. de Haro, K. Skenderis, and S. N. Solodukhin, "Holographic Reconstruction of Spacetime and Renormalization in the AdS/CFT Correspondence", [hep-th/0002230].

[47] K. Skenderis, "Lecture Notes on Holographic Renormalization", [hep-th/0209067].

[48] Eric Poisson, *An advanced course in general relativity*. University of Guelph, 2002.

[49] H. Bantilan and P. Romatschke, "Simulation of Black Hole Collisions in Asymptotically AdS Spacetimes", [1410.4799].

[50] S. S. Gubser, S. S. Pufu, and A. Yarom, "Entropy production in collisions of gravitational shock waves and of heavy ions", [0805.1551].

[51] P. Arnold, P. Romatschke, and W. van der Schee, "Absence of a local rest frame in far from equilibrium quantum matter", [1408.2518].

[52] N. J. Cerf and C. Adami, "Quantum Information Theory of Entanglement and Measurement", [quant-ph/9605039].

[53] S. Ryu and T. Takayanagi, "Holographic Derivation of Entanglement Entropy from AdS/CFT", [hep-th/0603001].

[54] A. Kitaev and J. Preskill, "Topological entanglement entropy", [hep-th/0510092].

[55] I. R. Klebanov, D. Kutasov, and A. Murugan, "Entanglement as a Probe of Confinement", [0709.2140].

[56] T. Nishioka, S. Ryu, and T. Takayanagi, "Holographic Entanglement Entropy: An Overview", [0905.0932].

[57] P. V. Buividovich and M. I. Polikarpov, "Numerical study of entanglement entropy in SU(2) lattice gauge theory", [0802.4247].

[58] E. Itou, K. Nagata, Y. Nakagawa, A. Nakamura, and V. I. Zakharov, "Entanglement in Four-Dimensional SU(3) Gauge Theory", [1512.01334].

[59] M. Rangamani and T. Takayanagi, "Holographic Entanglement Entropy", [1609.01287].

[60] A. Einstein, B. Podolsky, and N. Rosen, "Can Quantum-Mechanical Description of Physical Reality Be Considered Complete?", *Physical Review* **47** (1935) 777–780.

[61] S. Aoki, T. Iritani, M. Nozaki, T. Numasawa, N. Shiba, and H. Tasaki, "On the definition of entanglement entropy in lattice gauge theories", [1502.04267].

[62] A. Rényi, "On Measures of Entropy and Information", in *Proceedings of the Fourth Berkeley Symposium on Mathematical Statistics and Probability, Volume 1: Contributions to the Theory of Statistics*, vol. 1, pp. 547–561. University of California Press, 1961.

[63] A. Rényi, "On the Foundations of Information Theory", *Revue de l'Institut International de Statistique / Review of the International Statistical Institute* **33** (1965), no. 1 1–14.

[64] P. V. Buividovich and M. I. Polikarpov, "Entanglement entropy in gauge theories and the holographic principle for electric strings", *Physics Letters B* **670** (2008) 141–145, [0806.3376].

[65] Y. Nakagawa, A. Nakamura, S. Motoki, and V. I. Zakharov, "Entanglement entropy of SU(3) Yang-Mills theory", [0911.2596].

[66] E. Itou, "Quantum entanglement entropy for SU(3) gauge theories", http://www2.yukawa.kyoto-u.ac.jp/∼hhiqcd.ws/sympo/Itou.pdf , 2015.

[67] P. Calabrese and J. Cardy, "Entanglement Entropy and Quantum Field Theory", [hep-th/0405152].

[68] H. Casini and M. Huerta, "Entanglement and alpha entropies for a massive scalar field in two dimensions", [cond-mat/0511014].

[69] H. Liu and M. Mezei, "A refinement of entanglement entropy and the number of degrees of freedom", [1202.2070].

[70] P. Bueno and R. C. Myers, "Corner contributions to holographic entanglement entropy", [1505.07842].

[71] S. Ryu and T. Takayanagi, "Aspects of Holographic Entanglement Entropy", [hep-th/0605073].

[72] J. L. Cardy, "Is there a c-theorem in four dimensions?", *Physics Letters B* **215** (1988) 749–752.

[73] R. C. Myers and A. Sinha, "Holographic c-theorems in arbitrary dimensions", [1011.5819].

[74] Z. Komargodski and A. Schwimmer, "On Renormalization Group Flows in Four Dimensions", [1107.3987].

[75] A. B. Zamolodchikov, "Irreversibility of the flux of the renormalization group in a 2-D field theory", *JETP Letters* **43** (1986) 730–732.

[76] F. Gliozzi and L. Tagliacozzo, "Entanglement entropy and the complex plane of replicas", [0910.3003].

[77] L. Tagliacozzo, G. Evenbly, and G. Vidal, "Simulation of two-dimensional quantum systems using a tree tensor network that exploits the entropic area law", [0903.5017].

[78] J. Helmes, J.-M. Stéphan, and S. Trebst, "A Rényi entropy perspective on topological order in classical toric code models", [1507.04682].

[79] J. Cardy and P. Calabrese, "Unusual Corrections to Scaling in Entanglement Entropy", [1002.4353].

[80] M. Fagotti and P. Calabrese, "Entanglement entropy of two disjoint blocks in XY chains", [1003.1110].

[81] V. Alba, L. Tagliacozzo, and P. Calabrese, "Entanglement entropy of two disjoint blocks in critical Ising models", [0910.0706].

[82] S. Sahoo, E. M. Stoudenmire, J.-M. Stéphan, T. Devakul, R. R. P. Singh, and R. G. Melko, "Unusual Corrections to Scaling and Convergence of Universal Renyi Properties at Quantum Critical Points", [1509.00468].

[83] A. Lewkowycz and J. Maldacena, "Generalized gravitational entropy", [1304.4926].

[84] X. Dong, "The Gravity Dual of Renyi Entropy", [1601.06788].

[85] A. Karch, E. Katz, D. T. Son, and M. A. Stephanov, "Linear Confinement and AdS/QCD", [hep-ph/0602229].

[86] C. P. Herzog, "A Holographic Prediction of the Deconfinement Temperature", [hep-th/0608151].

[87] Z. Fodor, "QCD Thermodynamics", [0711.0336].

[88] G. Endrodi, Z. Fodor, S. D. Katz, and K. K. Szabo, "The equation of state at high temperatures from lattice QCD", [0710.4197].

[89] N. Cabibbo and E. Marinari, "A new method for updating SU(N) matrices in computer simulations of gauge theories", *Physics Letters B* **119** (1982) 387–390.

[90] B. Lucini, M. Teper, and U. Wenger, "Properties of the deconfining phase transition in SU(N) gauge theories", [hep-lat/0502003].

[91] J. Fingberg, U. M. Heller, and F. Karsch, "Scaling and Asymptotic Scaling in the SU(2) Gauge Theory", [hep-lat/9208012].

[92] P. Giudice and S. Piemonte, "Improved thermodynamics of SU(2) gauge theory", [1708.01216].

[93] M. M. Anber and B. J. Kolligs, "Entanglement entropy, dualities, and deconfinement in gauge theories", [1804.01956].

[94] K. Skenderis, "Asymptotically Anti-de Sitter spacetimes and their stress energy tensor", [hep-th/0010138].

[95] T. Sakai and S. Sugimoto, "Low energy hadron physics in holographic QCD", [hep-th/0412141].

[96] T. Sakai and S. Sugimoto, "More on a holographic dual of QCD", [hep-th/0507073].

Acknowledgments

First of all, I want to thank Andreas Schäfer for giving me the possibility to do my PhD at the University of Regensburg, the supervision, the funding for my position, and also for all travel expenses going to several conferences.
Another thanks goes to my collaborator Sebastian Waeber without whom it would not have been possible to finish the publication [1]. We had a hard time going through the numerics until we finally arrived at a working and stable code. During that time a lot of nice and interesting physics discussions took place.
Norbert Bodendorfer was always there to give great advice regarding scientific problems and other things in general. I also enjoyed all the great and patient explanations for all kind of physics questions even if the problem sounded naive in the first place. I also really enjoyed the collaboration leading to [3]. Besides the physics perspective, he also always let me take part in all social events of his working group even though I was not a member thereof.
Pavel Buividovich was also a collaborator to [3]. With providing his $SU(2)$ code he set a basis for this project. I also want to thank him for the nice and clear explanations mainly regarding lattice QCD topics. The discussions about efficient implementations were also very enlightening and fruitful.
Larry Yaffe was very helpful by discussing all kind of numerics regarding the solution of differential equations. He started giving me advice already during my Bachelor's thesis and this never came to an end. He always was a great help for the publication [1].
The numerical simulations for [3] were performed on ATHENE the HPC cluster of the Regensburg University Compute Center. I am very thankful for these resources and for the kind support by Randy Rückner.
A great thanks goes to my parents, Klaus and Anke, who always supported me during my whole studies, both financially as well as personally. I am really thankful that they enabled me my whole education. They were always there even in the hardest times.
Also, my siblings, Jonas and Johanna, were of great help with all the nice gatherings and non-physical discussion. Also the interest brought to each others field

of studies was very pleasant for me. My brother Jonas helped me a lot with all kinds of questions regarding computer science.
I also want to thank my grandparents, Georg, Elisabeth, Fritz and Luise, for always supporting me and being so proud of me.
My friends are a very important factor in my life. I want to thank them herewith. I do not want to give any specific names since it then becomes hard to decide where to stop. I want to thank all my friends in Regensburg for making my studies such a great and delightful time. I am also very happy about my friends in my place of origin who always gave me a warm welcome whenever I came back to my hometown. I really appreciated all the very nice non-physics discussions.